ELECTRICAL IMPEDANCE TOMOGRAPHY USING LORENTZ FIELDS

A THESIS SUBMITTED TO

THE GRADUATE SCHOOL OF NATURAL AND APPLIED SCIENCES

OF

MIDDLE EAST TECHNICAL UNIVERSITY

BY

REYHAN ZENGİN

IN PARTIAL FULFILLMENT OF THE REQUIREMENTS

FOR

THE DEGREE OF DOCTOR OF PHILOSOPHY

IN

ELECTRICAL AND ELECTRONICS ENGINEERING

SEPTEMBER 2012

Approval of the thesis:

ELECTRICAL IMPEDANCE TOMOGRAPHY USING LORENTZ FIELDS

submitted by **REYHAN ZENGİN** in partial fulfillment of the requirements for the degree of **Doctor of Philosophy in Electrical and Electronics Engineering Department, Middle East Technical University** by,

Prof. Dr. Canan Özgen
Dean, Graduate School of **Natural and Applied Sciences** _____

Prof. Dr. İsmet Erkmen
Head of Department, **Electrical and Electronics Eng.** _____

Prof. Dr. Nevzat Güneri Gençer
Supervisor, **Electrical and Electronics Eng. Dept., METU** _____

Examining Committee Members:

Prof. Dr. Mustafa Kuzuoğlu
Electrical and Electronics Engineering Dept., METU _____

Prof. Dr. Nevzat Güneri Gençer
Electrical and Electronics Engineering Dept., METU _____

Prof. Dr. Ergin Atalar
Electrical and Electronics Engineering Dept., Bilkent University _____

Prof. Dr. Gerhard Wilhelm Weber
Institute of Applied Mathematics Dept., METU _____

Assist. Prof. Dr.Yeşim Serinağaoğlu Doğrusöz
Electrical and Electronics Engineering Dept., METU _____

Date: 13.09.2012

I hereby declare that all information in this document has been obtained and presented in accordance with academic rules and ethical conduct. I also declare that, as required by these rules and conduct, I have fully cited and referenced all material and results that are not original to this work.

Name, Last Name: REYHAN ZENGİN

Signature:

ABSTRACT

ELECTRICAL IMPEDANCE TOMOGRAPHY USING LORENTZ FIELDS

Zengin, Reyhan

Ph.D., Department of Electrical and Electronics Engineering

Supervisor: Prof. Dr. Nevzat Güneri Gençer

September 2012, 148 pages

In this thesis, a novel approach is proposed to image the electrical conductivity properties of biological tissues. This technique is based on electrical current induction using ultrasound together with and applied static magnetic field. Acoustic vibrations are generated via piezoelectric transducers located on the surface of a biological body. To simulate the new technique multiphysics solution is required which couples pressure and electromagnetic equations. The feasibility of the proposed approach is investigated using analytical and numerical techniques. A linear phased array piezoelectric transducer and a single element transducer are used to form pressure distribution in human body/tissue. In the existence of a static magnetic field, the resultant (velocity) current density is sensed by a receiver coil encircling the tissue and used for reconstructing the conductivity distribution. To

sense the resultant current density a novel coil configuration is proposed. Truncated Singular Value Decomposition (tSVD) Method is used as a reconstruction algorithm. Results show the potential of this approach as a new, practical and high resolution imaging modality for electrical conductivity imaging.

Keywords: Electrical Conductivity Imaging, Contactless Imaging, Reconstruction Algorithm, Ultrasound, Linear Phased Array Transducer

ÖZ

LORENTZ ALANLARI İLE ELEKTRİKSEL EMPEDANS TOMOGRAFİSİ

Zengin, Reyhan

Doktora, Elektrik ve Elektronik Mühendisliği Bölümü

Tez Yöneticisi: Prof. Dr. Nevzat Güneri Gençer

Eylül 2012, 148 Sayfa

Bu çalışmada, biyolojik dokuların elektriksel iletkenlik özelliklerinin görüntülenmesi için yeni bir yaklaşım önerildi. Bu yaklaşım, ultrason ve statik manyetik alanla elektrik akım indükleme tabanlıdır. Akustik titreşimler, biyolojik doku üzerine yerleştirilen piezoelektrik dönüştürücüler tarafından oluşturulur. Yeni teknigin benzetimi için basınç ve elektromagnetik denklemlerin birlikte çözülmesi gerekir. Önerilen yaklaşımın fizibilitesi analitik ve sayısal tekniklerle incelendi. Doku/organda basınç dağılımı oluşturmak için doğrusal dizili ve tek elemanlı ultrasonik dönüştürücüler kullanıldı. Statik manyetik alanın varlığında oluşan hız

akım yoğunluğu, dokunun etrafını çevreleyen algılayıcı bobin ile algılanır ve iletkenlik dağılımını geriçatmak için kullanılır. Oluşan akım yoğunluğunu algılamak için yeni bir bobin sistemi önerildi. Geriçatma algoritmalarından Kesilmiş tekil değer ayrıştırması metodu kullanıldı. Sonuçlar, önerilen yaklaşımın yeni, pratik ve elektrik iletkenlik görüntülemesi için yüksek çözünürlükte bir görüntüleme olduğunu göstermektedir.

Anahtar Kelimeler: Elektrik iletkenlik görüntülemesi, Dokunmasız görüntüleme, Geriçatma Algoritması, Ultrason, Doğrusal faz dizili dönüştürücü

To my mother and my father,

To my husband,

ACKNOWLEDGMENTS

TABLE OF CONTENTS

LIST OF FIGURES

FIGURES

xxi

LIST OF TABLES

TABLES

CHAPTER 1

INTRODUCTION

1.1 Electrical properties of body tissues

The electrical properties of body tissues identify the pathways of current flow through the body and have attracted the interest of many investigators [1]. The behavior of these properties is examined on a *microscopic* and *macroscopic* scale. Depending on the tissue size that is examined, the electrical conductivity can be considered as, for example, *inhomogeneous* in microscopic scale whereas *homogeneous* in macroscopic scale. The conductivity in macroscopic scale is called the *effective conductivity* [2, 3].

To determine the electrical properties of biological tissues the interaction of polar molecules and ions is studied. If a material is composed of neutral molecular dipoles, it is called as a *dielectric* material. The positively charged ions (cations) and negatively charged ions (anions) produce *conductive* paths of current flow between extracellular and intracellular spaces. In this manner, a biological tissue is considered as a *conductive dielectric*.

The electrical behavior of a biological tissue is defined using the two parameters: dielectric constant (permittivity) ε (F/m) and electric conductivity σ (S/m). The

dielectric constant and conductivity values of different body tissues are listed in Appendix B. The electrical properties of biological tissues are non-linear functions of frequency. Furthermore, if the frequency of electromagnetic field changes, the interaction between the field and the tissue also changes [4]. There are several mechanisms that affect this frequency dependence. The following are the different mechanisms for a typical soft tissue [1]:

- For low frequencies (lower than several hundred kHz) the conductivity of tissue is dominated in the extracellular space by the conduction in the electrolytes. The volume fraction of extracellular space and the conductivity of the extracellular medium affect the bulk conductivity of the tissue.

- At low frequencies, due to the polarization of counter ions near charged surfaces in the tissue and the polarization of large membrane-bound structures in the tissue, the tissue exhibits a dispersion called *alpha dispersion* (in low kHz range). The relative permittivity of tissue reaches very high values at frequencies below the alpha dispersion. The alpha dispersion can be observed in the permittivity but it is not noticeable in the conductivity of the tissue.

- For radio frequencies (0.1-10 MHz) the *beta dispersion* is exhibited since the cell membranes charge through the intracellular and extracellular media. Above the beta dispersion, current passes through both media. The beta dispersion can be observed in both dielectric constants and conductivity values.

- At microwave frequencies (above 1GHz), because of the rotational relaxation of the water content of tissues, the gamma dispersion is exhibited.

1.2 Electrical Impedance Tomography (EIT)

Imaging electrical conductivity of biological tissues is one of the major research areas in the field of medical imaging. To image the conductivity of body tissues researchers have proposed different approaches. The earliest and generally accepted title for this relatively new imaging modality is Electrical Impedance Tomography (EIT) which uses surface electrodes to inject current and measures voltages from the body surface. Magnetic Resonance Electrical Impedance Imaging Tomography (MREIT), Magnetic Induction Tomography (MIT), Magneto Acoustic Tomography (MAT), Magneto-Acousto-Electrical Tomography (MAET) and Magneto Acoustic Tomography with Magnetic Induction (MAT-MI) are approaches proposed for the same purpose, but use other means for applying currents and measurements.

The purpose of this thesis is to introduce a novel technique based on ultrasonically induced velocity field for a body exposed to a static magnetic field. The proposed technique has the advantage of steering electrical current ultrasonically inside the body while measuring the resultant interaction (time-varying magnetic field) using an encircling coil, magnetically. The rest of this section presents the previous work on impedance imaging.

In EIT, there are two major approaches: Applied Current Electrical Impedance Tomography (ACEIT) [5-7] and Induced Current Electrical Impedance Tomography (ICEIT) [8, 9]. In ACEIT electrodes are placed on the surface of a body. Electrical current is injected between a pair of electrodes and the resultant voltage is recorded between two surface electrodes [5]. Current drive and voltage measurement electrodes are changed to obtain an independent set of data for image reconstruction.

In ICEIT currents are induced using time-varying magnetic fields using different coil configurations around the body. The surface electrodes are used to measure the voltage data. The features of the induced currents as an alternative to injected (applied) currents are listed as follows [10] :

- The currents in the medium are not limited by the current density at the electrodes, thus larger current densities can be induced yielding higher SNR in the measurements.
- An electrode on the periphery of the region is optimized to sense voltages, and not used for current drive.
- The number of measurements can be increased by increasing the number of different coil configurations.

In the earlier studies, impedance imaging was performed at a particular frequency. Recently, multi-frequency EIT studies were introduced to exploit the frequency dependent changes in the electrical properties for diagnostic purposes (MFEIT) [3, 11-15]. In Magnetic Resonance Current Density Imaging (MRCDI), the internal magnetic flux density is measured to visualize the current density distribution due to currents injected from the body surface [16-18]. To get internal magnetic flux density images MRCDI requires an MRI scanner. Once the magnetic flux density is measured, an image of the corresponding internal current density distribution is reconstructed using the Ampere's Law.

MREIT is another technique that utilizes the magnetic flux density produced by an injected current [19-22]. The purpose of MREIT is to reconstruct the conductivity distribution from magnetic field measurements using MRI. This approach can be assumed as a combination of EIT and MRCDI.

In MIT [23-26], currents are induced in the conductive body by time-varying magnetic fields using transmitter coils. The secondary magnetic fields due to existence of the conductive body are measured using receiver coils. The number of independent measurements is increased by changing the location of the transmitter coil.

In addition to these early attempts performed electromagnetically, recently, novel techniques are proposed that integrates electromagnetism with acoustics. MAT [27-29] is based on the idea that application of magnetic field to a liquid or tissue-like media in which electric currents are carried generates a force on the current pathway.

This force is known as the Lorentz force. When the applied magnetic field is alternating, the generated force on the internal currents is also alternating. This time-varying force in the medium generates acoustic wave fronts which propagate away from the current site. These vibrations are detected at the object surface using ultrasonic transducers.

In MAT-MI [30-33] technique, two magnetic fields are applied to the body: a static field and a time-varying magnetic field. Due to time-varying magnetic fields, eddy currents are generated. Eddy currents and applied static field results in vibrations (due to Lorentz force) and ultrasound waves are emitted. Ultrasonic transducers on the body surface are used as receivers. High resolution images of the conductivity distribution are reconstructed using this approach. The only difference between MAT-MI and MAT is that MAT uses electrical stimulation under static magnetic field. Since these approaches use ultrasound as the detected signal the resultant conductivity images have high resolution.

1.3 Ultrasound Imaging

After the discovery of piezoelectric effect (1880) ultrasound found applications in different fields, namely, development of sonar systems (1912-1915), detection of flaws (1928), detection of submarines (1940), non-destructive metal testing (1941), etc. In 1938, researchers started to study the interaction between ultrasound and living systems. In 1948, an extensive study has started on ultrasound medical imaging in the USA and Japan.

Figure 1-1 shows the three different ranges of acoustic waves, namely, infrasound, sound and ultrasound. The frequency range above the audio band (20 Hz-20 kHz) is named as ultrasound. Ultrasound has found numerous applications in different areas such as diagnostic sonography, animal research ultrasonography, medical imaging, etc. In medical applications of ultrasound, generally, frequencies above 1 MHz are

used. Lower frequencies between 1-3 MHz are used for imaging the deep-lying structures, such as liver. Higher frequencies as 5-10 MHz are used for imaging regions that are close to the body surface [34]. Acoustic waves support their propagation in a physical medium. When the acoustic waves propagate with a velocity c_0 *(m/s)*, the particles of the medium oscillate about their equilibrium position with a velocity u *(m/s)*.

The reflectivity of tissue to sound waves and velocity of moving objects are measured with ultrasound imaging. Since it is radiation-free, it is a noninvasive method. Furthermore, ultrasound is external applied and non-traumatic. The ultrasound images can be captured in real time, thus, not only the structure of the body but also the movement of internal organs can be shown. Ultrasound is used as a diagnostic tool and as a therapeutic modality in medicine [35].
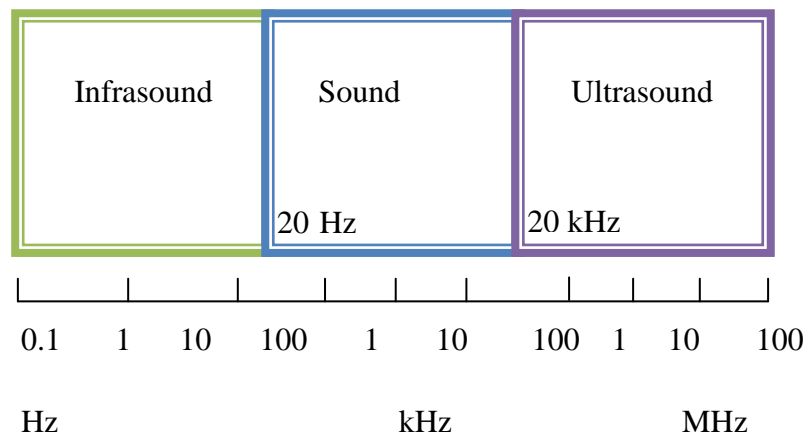
Figure 1-1 Spectrum of acoustic waves [35].

Clinical applications of ultrasound are listed below [36]:

- Angiology (angiography, arterial wall properties, detection of gas bubble formation within tissue due to decompression),
- Cardiology (heart wave studies, diagnosis of congenital heart disease, measurements of left ventricular volume and function, two-dimensional imaging of the heart, ultrasonic contrast studies, pericardial effusion, pleural effusion and pulmonary embolism),
- Endocrinology (adrenal glands, thyroid glands),
- Gastroenterology (teeth and mouth, liver, spleen, stomach and intestine, gallbladder and bile duct, pancreas, ascites),
- Neurology (midline localization, A-scope studies of the brain, intracranial pulsations, two-dimensional visualization of the brain).
- Obstetrics and Gynecology (early diagnosis of pregnancy, diagnosis of multiple pregnancy, visualization of placenta, assessment of fetal development, fetal anatomy, fetal heart rate, fetal breathing, fetal urine-production rate, diagnosis of fetal death, hydatidiform mole, detection of intrauterine contraceptive devices, abdominal tumors associated with pregnancy, gynecological tumors)
- Oncology (ultrasonic scanning in radiotherapy and chemotherapy, investigations of the breast)
- Ophthalmology (A-scan studies, B-scan studies)
- Orthopedics and Rheumatology (soft tissue thickness and edema, assessment of fracture healing, assessment of osteoporosis)
- Otothinolaryngology
- Urology (kidney, bladder, prostate, testis)

1.4 The proposed approach: Electrical Impedance Tomography using Lorentz Fields

In this thesis, a novel impedance imaging technique is proposed that integrates electromagnetic fields and ultrasound to introduce current inside the body. The geometry of the proposed method is shown in Figure 1.2. This method is based on Lorentz fields generated by applying ultrasound together with an applied static magnetic field. Acoustic vibrations are generated via piezoelectric transducers located on the surface the body. The resultant field due to velocity current density distribution in the body is sensed by an encircling coil.

The advantages of the proposed method, as compared to the other tomography methods, are as follows:

1) No surface electrodes are used to inject current in the conducting body; larger current densities can be introduced since the currents in the body are not limited by the current density just beneath the electrodes.

2) No coils are used to induce current in the conducting body; when coils are used it is difficult to manipulate the current density distribution.

3) To induce currents in a conducting body only an ultrasonic transducer and static magnetic field are required.

4) To measure the resultant current density an encircling coil is used yielding contactless measurements (same advantage as in MIT, MAT, MAT-MI)

5) There are different types of ultrasonic transducer used in medical applications, thus the type of ultrasonic transducer can be chosen according to the size of subject to be imaged.

6) Electronically steering and focusing properties of transducer (linear phased array) give wide range of area to be scanned in a short time. Current induction duration is less as compared the others (since scanning with an US transducer is faster.).

$$\vec{J}_{vel} = \sigma(\vec{v} \times \vec{B})$$
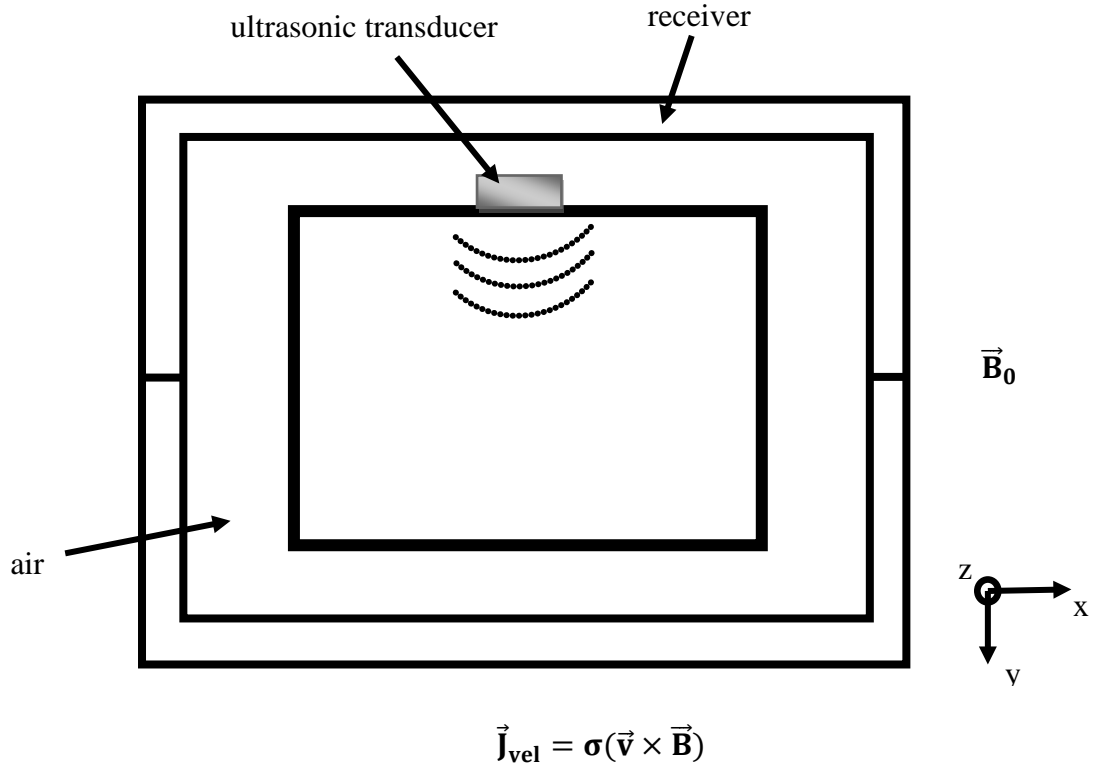
Figure 1-2 Problem Geometry for the Electrical Impedance Imaging using Lorentz Fields. A uniform static magnetic flux density $\vec{B}_0$ is applied along the z-axis. An ultrasonic pulse propagating along y-axis generates velocity currents ($\vec{J}_{vel}$) due to Lorentz fields. The resultant time-varying magnetic fields are measured using a receiver coil encircling the conductive body.

1.5 Objectives of the thesis

EIT using Lorentz fields must be studied in mathematical terms. The problem definition must be clarified, basic assumptions and numerical solution strategies must be investigated in detail. This is necessary in order to understand the performance and basic limitations of the proposed method relative to the other approaches in this field. Therefore, specific goals are as follows:

9

- To formulate the forward problem. That is, for a body of known conductivity distribution, calculation of measurements due to Lorentz fields (generated by an applied ultrasound and a static magnetic field).

- To explore numerical solution methods for the forward problem and investigate the characteristics of the imaging system with simulations. The numerical method must handle the corresponding multiphysics problem that couples acoustic and electromagnetic equations.

- To analyze the sensitivity of measurements to the conductivity perturbations.

- To formulate the inverse problem, i.e., calculation of the conductivity distribution from the measurements, and investigate its characteristics.

- To reconstruct images of simulated data using different inverse problem algorithms and investigate their performances.

1.6. Thesis Outline

Formulation of the forward problem is given in Chapter 2. Numerical solutions of the Lorentz fields are described in Chapter 3. To solve the problem numerically, finite element method based software called Comsol Multiphysics is used. The modules of Comsol are also described in this chapter. After the forward problem description, solution of forward and inverse problem is described in Chapter 4. Sensitivity matrix analysis is performed for a specific body/transducer/receiver coil configuration.

The results of the forward and inverse problems are also given in Chapter 4. Pressure and velocity current density distributions in conductive bodies are shown. Truncated Singular Value Decomposition (tSVD) method is used to reconstruct the image. The reconstructed images are given for specific conductivity perturbations. Conclusion and discussion are given in Chapter 5. Focusing and steering properties of ultrasound are described in Appendix A. A brief review of the transducers, especially linear phased array transducers are described. The electrical and acoustic properties

of human tissues are given in Appendix B. General information about the single to noise ratio (SNR) of a data acquisition system is given is Appendix C.

CHAPTER 2

FORWARD PROBLEM

2.1 Introduction

The forward problem of the proposed imaging modality is a *multiphysics* problem, i.e., the electromagnetic and acoustics fields must be solved simultaneously (Figure 2.1). In this section, first the basic field equations governing the behavior of time-varying electromagnetic and acoustic fields are given. Secondly, the general formulation of the partial differential equations for the scalar and magnetic vector potentials are presented in the electromagnetic part of this work. In the acoustic part, the formulation of the partial differential equation for the acoustic pressure is presented. Thereafter, relation of the measurements to the existing (coupling) electromagnetic and acoustic waves is described.
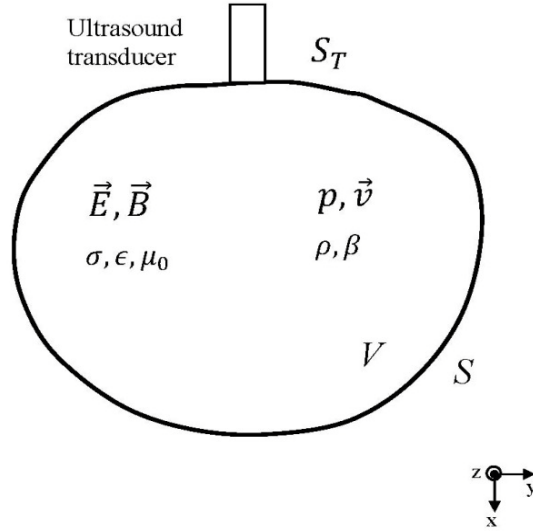
Figure 2-1 Forward problem geometry. The conductive body with material properties $(\sigma, \epsilon, \mu_0)$ and bounded by surface S is under uniform static field $\vec{B}_0$. To introduce currents inside the body an acoustic field is applied using an ultrasound transducer. The transducer surface is denoted by S_T. The acoustic material properties are the mass density ρ and compressibility β. Propagating ultrasound results in a time-varying pressure distribution p and particle velocity $\vec{v}$. The interaction of particle velocity $\vec{v}$ with the magnetic flux density generates electric field in volume V.

2.2 Basic Electromagnetic Field Equations

The following set of Maxwell's equations governs the behavior of time-varying electromagnetic fields in a linear, non-magnetic, isotropic conductive body [37]:

$$\nabla \times \vec{E} = -\frac{\partial \vec{B}}{\partial t} \tag{2.1}$$

$$\nabla \times \vec{B} = \mu_0 \vec{J} + \mu_0 \frac{\partial \vec{D}}{\partial t} \tag{2.2}$$

13

$$\nabla \cdot \vec{D} = \rho \tag{2.3}$$

$$\nabla \cdot \vec{B} = 0 \tag{2.4}$$

For the solution of these fields we need the continuity condition

$$\nabla \cdot \vec{J} = -\frac{\partial \rho}{\partial t} \tag{2.5}$$

and the constitutive relations:

$$\vec{D} = \epsilon \vec{E} \tag{2.6}$$

$$\vec{J} = \sigma \vec{E} + \sigma \left(\vec{v} \times \vec{B} \right) \tag{2.7}$$

where $\vec{v}$ is the velocity of the conductor and $\vec{v} \times \vec{B}$ is the *Lorentz field*. The second term on the right hand side of this equation is known as the *velocity* current density.

Since the divergence of $\vec{B}$ is zero (Equation (2.4)), it is possible to introduce a magnetic vector potential $\vec{A}$ as

$$\vec{B} = \nabla \times \vec{A} \tag{2.8}$$

Consequently, $\vec{E}$ can be expressed in terms of the magnetic vector potential $\vec{A}$ and gradient of a scalar potential φ as

$$\vec{E} = -\nabla \varphi - \frac{\partial \vec{A}}{\partial t} \tag{2.9}$$

2.3 $\vec{A} - \varphi$ Formulation

In three-dimensional (3D) problems, the electric and magnetic fields are usually calculated using an $\vec{A} - \varphi$ formulation which results in two coupled equations in terms of $\vec{A}$ and φ. To obtain the first equation, Equation (2.2) is rewritten in terms of the magnetic vector potential $\vec{A}$ as follows:

$$\nabla \times \mu_0^{-1} (\nabla \times \vec{A}) = \vec{J} + \frac{\partial \vec{D}}{\partial t} \tag{2.10}$$

The terms $\vec{J}$ and $\vec{D}$ on right hand side can be expressed using equations (2.6) and (2.7) yielding:

$$\nabla \times \mu_0^{-1} (\nabla \times \vec{A}) = \sigma(\vec{E} + \vec{v} \times \vec{B}) + \frac{\partial}{\partial t} \epsilon \vec{E} \tag{2.11}$$

Reorganizing the right hand side we obtain,

$$\nabla \times \mu_0^{-1} (\nabla \times \vec{A}) = (\sigma + \epsilon \frac{\partial}{\partial t}) \vec{E} + \sigma(\vec{v} \times \vec{B}) \tag{2.12}$$

By replacing $\vec{B}$ and $\vec{E}$ using the expressions in (2.8) and (2.9) we obtain,

$$\nabla \times \mu_0^{-1} (\nabla \times \vec{A}) + \left(\sigma + \epsilon \frac{\partial}{\partial t}\right) (\nabla \varphi + \frac{\partial \vec{A}}{\partial t}) - \sigma(\vec{v} \times \nabla \times \vec{A}) = 0 \tag{2.13}$$

A second equation relating $\vec{A}$ and φ can be obtained using the continuity equation (Equation (2.5)),

$$\nabla \cdot \vec{J} = \nabla \cdot \sigma\left(\vec{E} + \vec{v} \times \vec{B}\right) = -\frac{\partial}{\partial t} \nabla \cdot \left(\epsilon \vec{E}\right) \tag{2.14}$$

$$\nabla \cdot \sigma\left(\vec{E} + \vec{v} \times \vec{B}\right) + \frac{\partial}{\partial t} \nabla \cdot \left(\epsilon \vec{E}\right) = 0 \tag{2.15}$$

$$\nabla \cdot \left[\left(\sigma + \frac{\partial}{\partial t}\epsilon\right)\vec{E} + \sigma(\vec{v} \times \vec{B}) = 0 \tag{2.16}$$

Once again, using the expressions in equations (2.8) and (2.9), we obtain

$$\nabla \cdot \left[\left(\sigma + \frac{\partial}{\partial t}\epsilon\right)\left(\nabla\varphi + \frac{\partial \vec{A}}{\partial t}\right) - \sigma\left(\vec{v} \times \nabla \times \vec{A}\right)\right] = 0 \tag{2.17}$$

Equations (2.13) and (2.17) represent the general form of the system of equations that is used to calculate $\vec{A}$ and φ for arbitrary excitations. For sinusoidal excitations ($e^{j\omega t}$ is assumed), these two equations can be written using phasor notation (boldface) as follows:

$$\nabla \times \mu_0^{-1}\left(\nabla \times \boldsymbol{\vec{A}}\right) + (\sigma + j\omega\epsilon)\left(\boldsymbol{\nabla\varphi} + j\omega\boldsymbol{\vec{A}}\right) - \sigma\left(\boldsymbol{\vec{v}} \times \nabla \times \boldsymbol{\vec{A}}\right) = 0 \tag{2.19}$$

$$\nabla \cdot \left[(\sigma + j\omega\epsilon)\left(\boldsymbol{\nabla\varphi} + j\omega\boldsymbol{\vec{A}}\right) - \sigma\left(\vec{v} \times \nabla \times \boldsymbol{\vec{A}}\right)\right] = 0 \tag{2.20}$$

In the proposed system, the conductive body is source-free, i.e., the low-frequency biological sources and corresponding potentials are of no concern. The potentials $\vec{A}$

16

and φ can be solved once the boundary conditions are set due to external sources. In the proposed approach, neither a time-varying magnetic field is applied using external coils nor a current or potential is applied using, for example, surface electrodes. The origin of the electric and magnetic potentials is the Lorentz fields and currents generated by the combination of a uniform static magnetic field $\vec{B}_0$ (say, in z direction) and a propagating acoustic field. The latter is generated by an ultrasound transducer attached on the surface of the body as shown in Figure 2.1. Equations (2.19) and (2.20) together with appropriate boundary conditions can be used to calculate the electric field components for general conditions, i.e., general material properties and excitation frequencies. The formulation, however, can be considerably simplified under three major assumptions: 1) displacement currents are negligible, 2) propagation effects can be ignored, and 3) inductive effects are negligible. Following section investigates the verification of these assumptions.

2.4 Model Simplification: φ Formulation

Imaging electrical properties of breast tissue can be considered as an important application area for the new imaging modality. To model breast, breast fat and blood are two tissues of primary concern. The conductivity and permittivity values of various biological tissues at different frequencies can be found in [38-40] . Using the tabulated values, the conduction to displacement current ratio $\sigma/\omega\epsilon$ is calculated for these two tissues at an operation frequency of 1 MHz. This ratio is found 19.8 and 4.9 for breast fat and blood, respectively. Note that, for most of the tissues other than blood, this ratio is found higher than 5.

To ignore the propagation effects the wavelength must be much larger than the maximum field point in the biological body. At 1 MHz, the wavelengths are 3 m and 19.2 m in blood and breast fat, respectively. Consequently, for an imaging distance of 0.1 m, propagation affects can be ignored.

17

To verify the third assumption, the magnitude of the two electric field components (given in Equation (2.9)) can be compared assuming a specific source in a homogeneous medium. The approach has been applied for different purposes in the [41] literature, and is adopted here to provide a quantitative basis for simplification. This ratio is found as follows:

$$\left|\frac{\omega\vec{A}}{\nabla\varphi}\right| = \left|\omega^2\mu_0\epsilon\left(1 + \frac{\sigma}{j\omega\epsilon}\right)R^2\right| \tag{2.21}$$

As expected, the ratio depends on the material properties (σ, ϵ, μ), excitation frequency (ω) and the maximum distance (R) between the source and field points in the imaging area. In this study, this ratio is calculated for blood and breast fat tissues. At an operation frequency of 1 MHz, using the material properties of blood ($\sigma = 0.82$ S/m, $\epsilon = 3000\epsilon_0$ F/m) and free space ($\mu_0 = 4\pi \times 10^{-7}$ H/m, $\epsilon_0 = 8.854 \times 10^{-12}$ F/m) one obtains a value of 0.43 when $R = 0.1$ m and 0.1 when R= 0.05m. The ratio reduces to 0.002 when the tissue is assumed breast fat ($\sigma = 0.026$ S/m, $\epsilon = 23.6\epsilon_0$ F/m) and R = 0.1 m. In a possible breast model, the larger part of the body should be assumed as breast fat, whereas a tumor in the breast can be a couple of millimeters. One may conclude that for such a model inductive effects can be ignored. However, for different parts of the body (with different sizes and electrical properties) and higher operation frequencies, this assumption should be further investigated.

Note that, under the above three assumptions, one obtains the quasi-static electric field expression:

$$\vec{E} = -\nabla\varphi \tag{2.22}$$

The partial differential equation governing the behavior of the scalar potential distribution due to ultrasonically induced Lorentz fields is then written as:

$$\nabla \cdot \left[\sigma\nabla\varphi - \sigma(\vec{v} \times \vec{B})\right] = 0 \tag{2.23}$$

or

$$\nabla \cdot (\sigma \nabla \varphi) = \nabla \cdot \vec{J}_L \qquad in \ V \qquad\qquad (2.24)$$

where $\vec{J}_L = \sigma(\vec{v}(t) \times \vec{B})$ denotes the velocity current density.

The associated boundary condition for the scalar potential is derived to make the normal component of the total current zero on the body surface:

$$\sigma \frac{\partial \varphi}{\partial n} = \vec{J}_L \cdot \vec{n}$$

or

$$\frac{\partial \varphi}{\partial n} = (\vec{v}(t) \times \vec{B}) \cdot \vec{n} \qquad\qquad (2.25)$$

The potential of the ground point used for the potential difference measurements should be set to zero to obtain a unique solution to the Neumann problem. Note that for velocity fields with general time dependence, the Neumann boundary condition is a function of time and is determined by the behavior of the velocity vector $\vec{v}(t)$ on the surfaces.

Assume a particle velocity is generated to propagate in an infinitely thin line. If ultrasonic excitation is time-harmonic, then a steady-state boundary condition is achieved at both ends of this line that crosses the boundary. Since particle velocity is in a specific direction, then the boundary conditions should be positive at one end and negative at the other end. On the hand, if a brief pulse is applied to the transducer, then the boundary condition at the transducer end will be nonzero during the acoustic pulse generation and will be zero during the propagation of this pulse throughout the body. The boundary condition at the other end of this propagation line will be zero during the generation of the acoustic pulse at the transducer end. It will stay zero during the propagation in the body and will be nonzero as the particle velocity crosses the boundary.

Hall Effect Imaging (or Ultrasonically Induced Lorentz Field Imaging) is based on voltage measurements acquired from the body surface due to ultrasonically induced Lorentz fields (Figure 2-2). Note that the theory behind this imaging modality has not been presented in the literature. The derivations and simplifications presented in this section clarify the theory behind forward problem of Hall Effect Imaging and provide necessary tools to interpret the experimental results.

2.5 Model Simplification: B_z Formulation

To reveal the characteristics of the proposed imaging system, a two-dimensional (2D) numerical model is considered, assuming a body of finite thickness lying on the xy plane. Consequently, the electric field $\vec{E}$ and particle velocity $\vec{v}$ is represented by the transverse components only (i.e., x- and y- components), whereas the magnetic flux density has only z-component. In addition, the displacement currents $(\partial \vec{D}/\partial t)$ are assumed negligible. Under such conditions, computationally more efficient formulation can obtained starting from Equation (2.1):

$$\nabla \times \vec{E} + \frac{\partial \vec{B}}{\partial t} = 0 \qquad (2.26)$$

The electric field $\vec{E}$ has two components as given by Equation (2.7):

$$\vec{E} = \frac{\vec{J}}{\sigma} - \vec{v} \times \vec{B} \qquad (2.27)$$

This expression can be rewritten using equation (2.2),

$$\vec{E} = \frac{\nabla \times \vec{B}}{\mu_0 \sigma} - \vec{v} \times \vec{B} \qquad (2.28)$$

Consequently, equation (2.26) takes the following form:

$$\frac{1}{\mu_0} \nabla \times \left(\frac{1}{\sigma} \nabla \times \vec{B} - \vec{v} \times \vec{B} \right) + \frac{\partial \vec{B}}{\partial t} = 0 \qquad (2.29)$$

For a 2D simulation study, as will be shown in the next chapter, one may assume $\vec{B} = B_z \vec{a}_z$ and proceed the numerical calculations by computing the single flux density component.

The boundary condition for (2.29) is the usual condition that sets the continuity of the electric field on the body surface:

$$\vec{n} \times \left(\vec{E}_1 - \vec{E}_2 \right) = 0 \qquad (2.30)$$

where $\vec{n}$ is the outward normal on the body surface. $\vec{E}_1$ and $\vec{E}_2$ denote the electric fields on both sides of the surface.

2.6 Basic Acoustic Field Equations

To provide simplicity, a lossless, source-free medium is assumed and, initially, a one-dimensional (1-D) derivation is presented. In the static case, the body pressure is constant and denoted by p_0. The mass density of the body is assumed position

dependent and represented by $\rho_0(x)$. In the presence of a propagating pressure wave, the total pressure p_T is position and time-varying and is given as

$$p_T(x,t) = p_0 + p(x,t) \tag{2.31}$$

In such a case, the total mass density can be expressed as

$$\rho_T(x,t) = \rho_0 + \rho(x,t) \tag{2.32}$$

A propagating ultrasound also results in displacements in the small elements of the body and an associated 'particle velocity', $v(x,t)$. The particle displacement and its derivatives are small when $|p/p_0| \ll 1$ and $|\rho/\rho_0| \ll 1$. This results in a linearization procedure, and the 'equation of motion' is expressed as [42] :

$$-\partial p/\partial x = \rho_0 \ \partial v/\partial t \tag{2.33}$$

This shows that a particle accelerates in the opposite direction of the pressure gradient. The 'continuity equation' for mass conservation is written as

$$-\frac{\partial \rho_T}{\partial t} = \frac{\partial(\rho_T \ v)}{\partial x} \tag{2.34}$$

which reduces to the following after linearization (under the above given conditions):

$$-\frac{\partial \rho}{\partial t} = \rho_0 \frac{\partial v}{\partial x} \qquad (2.35)$$

To obtain a differential equation relating p and ρ, the particle velocity term in Equations (2.33) and (2.35) must be eliminated. This can be achieved by employing a 'constitutive equation' between them. If the change in mass density ρ is some function of changes in pressure p only, then a 'linearized constitutive equation' can be written as

$$\rho = [\partial \rho / \partial p]_{p=0} \; p = \rho_0 \beta_0 \; p \qquad (2.36)$$

where β_0 is the compressibility (reciprocal of the bulk modulus or elastic constant) defined as

$$\beta_0 = -\frac{1}{V}\frac{\partial V}{\partial p}$$

Following is the derivation of the wave equation for pressure by combining Equations (2.33), (2.35) and (2.36). Taking the spatial derivative of Equation (2.33) we obtain,

$$-\frac{\partial^2 p}{\partial x^2} = \frac{\partial}{\partial x}\left[\rho_0\left(\frac{\partial v}{\partial t}\right)\right] = \rho_0 \frac{\partial}{\partial x}\left(\frac{\partial v}{\partial t}\right) + \frac{\partial v}{\partial t}\frac{\partial \rho_0}{\partial x} \qquad (2.37)$$

The first term on the right hand side can be rewritten using Equation (2.35),

$$-\frac{\partial^2 p}{\partial x^2} = -\frac{\partial^2 \rho}{\partial t^2} + \frac{\partial v}{\partial t}\frac{\partial \rho_0}{\partial x} \qquad (2.38)$$

The second term on the right hand side can be modified using (2.33), yielding

$$-\frac{\partial^2 p}{\partial x^2} = -\frac{\partial^2 \rho}{\partial t^2} + \left(-\frac{1}{\rho_0}\frac{\partial p}{\partial x}\right)\frac{\partial \rho_0}{\partial x} \tag{2.39}$$

Using the linearized constitutive Equation (2.36), and reorganizing the equation, we obtain

$$(\rho_0 \beta_0)\frac{\partial^2 p}{\partial t^2} = \frac{\partial^2 p}{\partial x^2} - \frac{\partial p}{\partial x}\left(\frac{1}{\rho_0}\frac{\partial \rho_0}{\partial x}\right) \tag{2.40}$$

or

$$\frac{1}{c_s^2}\frac{\partial^2 p}{\partial t^2} = \frac{\partial^2 p}{\partial x^2} - \frac{\partial p}{\partial x}\left(\frac{1}{\rho_0}\frac{\partial \rho_0}{\partial x}\right) \tag{2.41}$$

where $c_s^2 = (\rho_0 \beta_0)^{-1}$ represents the speed of pressure waves. Multiplying both sides by $1/\rho_0$, and rearranging the right hand side, one obtains

$$\frac{1}{\rho_0 c_s^2}\frac{\partial^2 p}{\partial t^2} = \frac{\partial}{\partial x}\left(\frac{1}{\rho_0}\frac{\partial p}{\partial x}\right) \tag{2.42}$$

The three-dimensional form of Equation (2.42) is as follows:

$$\frac{1}{\rho_0 c_s^2}\frac{\partial^2 p}{\partial t^2} = \nabla \cdot \left(\frac{1}{\rho_0}\nabla p\right) \tag{2.43}$$

which is known as *the wave equation* for acoustic fields.

24

The equation of motion (Equation (2.33)) used in the preceding derivation is true as long as there are no other force terms. We may drop the terms related to gravitational force, whereas presence of current density $\vec{J}$ and magnetic flux density $\vec{B}$ in the body results in Lorentz force (per unit volume) $\vec{q} = \vec{J} \times \vec{B}$ in addition to the mechanical forces in the body. Consequently, in the presence of a magnetic flux density and charged particles in the body, equation of motion can be modified as follows:

$$q_x - \partial p/\partial x = \rho_0 \ \partial v/\partial t \tag{2.44}$$

where q_x denotes the x-component of this interaction. Note that, movement of charged particles results in a current density $\vec{J} = \sigma \vec{E} + \sigma(\vec{v} \times \vec{B})$, in turn, current density influences the motion. In such a case, the wave equation should be modified taking into account the effects of Lorentz forces, yielding

$$\frac{1}{\rho_0 c_s^2} \frac{\partial^2 p}{\partial t^2} = \nabla \cdot \left[\frac{1}{\rho_0} (\nabla p - \vec{q}) \right] \tag{2.45}$$

Since the medium is source-free, the pressure distribution is determined due to boundary conditions as dictated by an ultrasonic transducer in contact with the medium. In this study, the boundary conditions are assumed as follows:

$$\frac{1}{\rho_0} (\nabla p - \vec{q}) \cdot \vec{n} = a_n \quad on \ S_T \tag{2.46}$$

where S_T denotes the body surface which is in contact with the transducer, The term a_n in Equation (2.46) represents the *local acceleration* produced by the transducer (derivation of this term is discussed in the next section). The remaining part of the surface is denoted by S. The second boundary condition is obtained using the continuity relation for acceleration:

$$\frac{\partial \vec{v}_1}{\partial t} \cdot \vec{n} = \frac{\partial \vec{v}_2}{\partial t} \cdot \vec{n}$$

where $\vec{v}_1$ and $\vec{v}_2$ denote the particle velocities in region 1 and region 2 of an interface, respectively. This expression can also be written as

$$\frac{1}{\rho_{01}} \left(\nabla p - \vec{q} \right)_1 \cdot \vec{n} = \frac{1}{\rho_{02}} \left(\nabla p - \vec{q} \right)_2 \cdot \vec{n} \qquad on \ S \qquad (2.47)$$

2.7 Piezoelectric Medium:

Piezoelectric materials, which normally have neutral molecules, respond to an applied electric field by changing their mechanical dimensions.

Converse is also true; when a piezoelectric material is strained an electric field occurs due to small electric dipoles generated inside the material. This is due to their asymmetric atomic lattice. The field equations of piezoelectric materials couples the equations of elasticity and electricity by piezoelectric *constitutive relations* as explained below.

The force per unit area applied to a body is called *stress* and, in one-dimensional (1D) case, it is denoted by T. The fractional extension of the body is called *strain* and is denoted by S. For small stresses applied to a 1D system, the relation between stress and strain is given by the Hooke's law:

$$T = cS$$

where $c = 1/\beta_0$ is the *elastic constant* of the material (as given using a different notation in Equation (2.31)). In a piezoelectric material, however, the piezoelectric constitutive relation is as given below:

$$T = c^E S - eE \qquad (2.48)$$

The additional stress term on the right hand side is due to the presence of the electric field E. The parameter e is called the *piezoelectric stress constant*, and c^E is the *elastic constant in the presence of constant or zero E field.*

In the presence of an electric field E, the electrical displacement D depends on the strain as well as the electric field:

$$D = eS + \epsilon^S E \tag{2.49}$$

where ϵ^s is the *permittivity* with zero or constant strain.

If the material is not piezoelectric, the 'equation of motion', say in z-direction, is given by:

$$\frac{\partial T}{\partial z} = \rho_0 \frac{\partial v}{\partial t} \tag{2.50}$$

or

$$c^E \frac{\partial^2 u}{\partial z^2} = \rho_0 \frac{\partial^2 u}{\partial t^2} \tag{2.51}$$

which is another form of Equation (2.43) in terms of displacement u when the medium has uniform material properties.

The electrical behavior of the medium is governed by the following equation for the z component of the electrical displacement vector D_z,

$$\frac{\partial D_z}{\partial z} = 0 \tag{2.52}$$

implying that D_z is constant and there are no free charges in the medium. The electric field can be written in terms of the derivative of a scalar potential as follows:

$$E = -\frac{\partial \varphi}{\partial x}$$

Consequently, Equation (2.48) can be rewritten as:

27

$$-\epsilon^s \frac{\partial^2 \varphi}{\partial x^2} = 0 \tag{2.53}$$

If the material is not piezoelectric, Equations (2.47) and (2.49) are isolated. In a piezoelectric material, however, the elasticity and electricity equations are coupled due to piezoelectric constitutive relations (2.44) and (2.45). In such a case, one obtains the following equations of piezoelectricity in 1D:

$$c^E \frac{\partial^2 u}{\partial z^2} + e \frac{\partial^2 \varphi}{\partial z^2} = \rho_0 \frac{\partial^2 u}{\partial t^2} \tag{2.54}$$

$$e \frac{\partial^2 u}{\partial z^2} - \epsilon^s \frac{\partial^2 \varphi}{\partial x^2} = 0 \tag{2.55}$$

In a 3D problem, three equations are derived in the elasticity part for the three displacement components. Together with the electric field equation, four equations are obtained for four unknowns. Depending on the material properties, different forms of these equations can be found [43].

In this study, the displacements and potential distribution are solved using COMSOL multiphysics [44]. The normal component of the acceleration a_n on the crystal surface S_T is given as the boundary condition (Equation (2.46)) for the acoustic problem in the body.
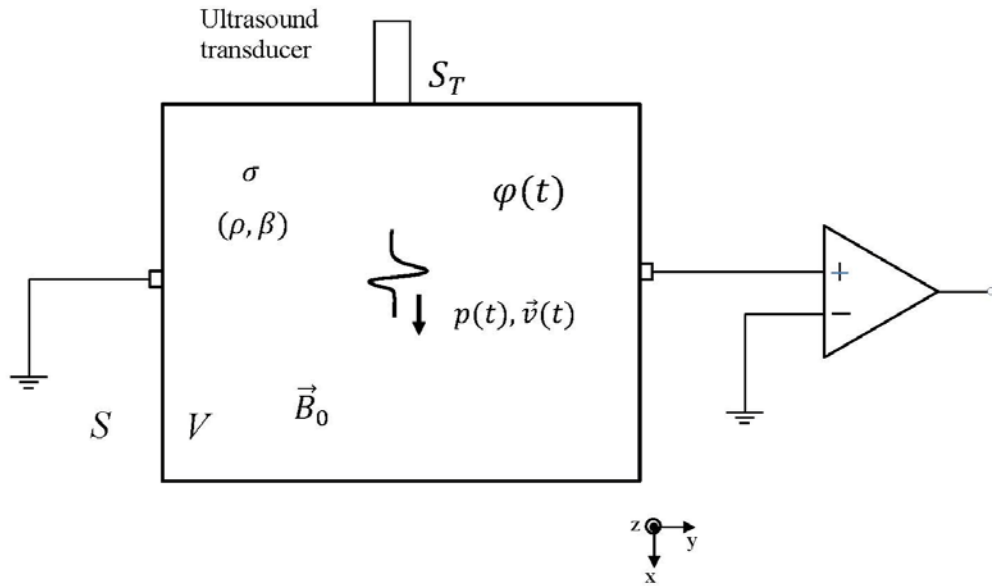
Figure 2-2 Problem geometry of Hall Effect Imaging. The body is assumed resistive with material properties (σ, μ_0) and bounded by surface S is under uniform static field $\vec{B}_0$. To introduce currents inside the body an acoustic field is applied using an ultrasound transducer. The resultant potential difference is measured using electrodes attached on the body surface.

2.8 Relation of measurements to the conductivity distribution

2.8.1 Voltage Measurements (Hall Effect Imaging)

Using the φ formulation presented in Section 2.4, the behavior of the scalar potential can be investigated for two cases: homogeneous and inhomogeneous conductivity distributions.

2.8.1.1 Homogeneous conductivity distribution:

For a homogeneous conductivity distribution ($\sigma = \sigma_0 = constant$), Equations (2.24) and (2.25) can be written as,

29

$$\nabla^2 \varphi_0 = \nabla \cdot \vec{J}_L \qquad\qquad in\ V \qquad\qquad\qquad (2.56)$$

$$\frac{\partial \varphi_0}{\partial n} = \left(\vec{v} \times \vec{B}\right) \cdot \vec{n} \qquad on\ S\ and\ S_T \qquad\qquad (2.57)$$

The potential of a point on the surface, corresponding to the reference point of voltage measurements, should also be set to zero.

The divergence of the velocity current $\vec{J}_L = \sigma_0 \vec{E}_L = \sigma_0 \left(\vec{v} \times \vec{B}\right)$ can be approximated as:

$$\sigma_0 \nabla \cdot \vec{E}_L \approx \sigma_0 \nabla \cdot \left(\vec{v} \times \vec{B}_0\right) \qquad\qquad\qquad (2.58)$$

since the static field is much greater than the ultrasonically induced magnetic flux density. Using the vector identity $\nabla \cdot \left(\vec{A} \times \vec{B}\right) = \sigma_0 (\vec{B} \cdot \nabla \times \vec{A} - \vec{A} \cdot \nabla \times \vec{B})$, one obtains

$$\sigma_0 \nabla \cdot \left(\vec{v} \times \vec{B}_0\right) = \sigma_0 (\vec{B}_0 \cdot \nabla \times \vec{v} - \vec{v} \cdot \nabla \times \vec{B}_0) \qquad\qquad (2.59)$$

In an acoustically uniform medium (i.e., mass density is uniform), assuming particle motion is primarily determined by ultrasonic sources, it can be shown that curl of the particle velocity is equal to zero $(\nabla \times \vec{v} = 0)$. Since the source current of the static field generator is outside the body, curl of the static field $\left(\nabla \times \vec{B}_0 \right)$ is also equal to zero in V. Consequently, when the conductivity is homogeneous, the divergence of the velocity current density is zero $(\nabla \cdot \vec{J}_L = 0)$. Since there are no internal sources, the potential φ_0 is determined due to nonzero boundary conditions as given by Equation (2.57). One should note that $\varphi_0(x, y, z)$ and related voltage measurement are time dependent due to time-varying velocity fields, however, they are independent of the conductivity σ_0 of the medium.

As discussed in section 2.4, for a propagating brief acoustic pulse, the boundary conditions at both ends of the propagation line will be non-zero at different time instants. During the propagation, however, the boundary conditions will be zero yielding $\varphi_0 = 0$ in the body.

2.8.1.2 Inhomogeneous conductivity distribution:

When the conductivity is not homogeneous, then Equation (2.24) should be satisfied:

$$\nabla \cdot (\sigma \nabla \varphi) = \nabla \cdot \vec{J}_L = \nabla \sigma \cdot \vec{E}_L + \sigma \nabla \cdot \vec{E}_L \qquad (2.60)$$

where the right hand side is written in terms of the velocity field $\vec{E}_L$. Recognizing that the divergence of the velocity field is zero we obtain,

$$\nabla \cdot (\sigma \nabla \varphi) = \nabla \sigma \cdot \vec{E}_L = \nabla \sigma \cdot \ \vec{v} \times \vec{B} \qquad (2.61)$$

The source term of this equation, expressed by the scalar product of the conductivity gradient and the velocity field, represents the charge accumulation at the conductivity interfaces. Obviously, if the gradient is in the same direction of the velocity field then the magnitude of potential reaches to its maximum value. Since the velocity field $\vec{E}_L$ is inversely proportional to the mass density ρ_0 (equation (2.33)), the voltage measurements are related to the conductivity gradient weighted by mass density, as reported in different studies [37] .

The boundary condition for equation (2.61) can be written as:

$$\frac{\partial \varphi}{\partial n} = \ \left(\vec{v} \times \vec{B} \right) \cdot \vec{n} \qquad on \ S \ and \ S_T \qquad (2.62)$$

In a three-dimensional body, the potential at any instant is determined by the distribution of conductivity gradient and velocity field in the body. For a propagating velocity field, the potential is also time varying and changes as a function of sound propagation velocity.

Note that the boundary conditions for homogeneous (Equation 2.57) and inhomogeneous cases (Equation 2.62) are almost same (assuming velocity field assuming velocity field is same for both cases). They determine the contribution

from the body surface and can be eliminated if the first order variation in the scalar potential function is calculated due to a perturbation in conductivity distribution.

2.8.1.3 The first order variation in the potential distribution ($\Delta\varphi$) due to a conductivity perturbation ($\Delta\sigma$):

Let φ_0 and φ be the scalar potential functions corresponding to conductivity distributions σ_0 and σ (we assume σ_0 is the initial conductivity distribution which is not necessarily homogeneous). Then they obey the following differential equations:

$$\nabla \cdot (\sigma_0 \nabla \varphi_0) = \nabla \sigma_0 \cdot \vec{v} \times \vec{B} \tag{2.63}$$

$$\nabla \cdot (\sigma \nabla \varphi) = \nabla \sigma \cdot \vec{v} \times \vec{B} \tag{2.64}$$

Equation (2.64) can be rewritten by replacing φ with $\varphi_0 + \Delta\varphi$ and σ with $\sigma_0 + \Delta\sigma$:

$$\nabla \cdot (\sigma_0 \nabla \varphi_0) + \nabla \cdot \left(\sigma_0 \nabla(\Delta\varphi)\right) + \nabla \cdot (\Delta\sigma \nabla \varphi_0) + \nabla \cdot \left(\Delta\sigma \nabla(\Delta\varphi)\right)$$

$$= \nabla \sigma_0 \cdot \vec{v} \times \vec{B} + \nabla(\Delta\sigma) \cdot \vec{v} \times \vec{B}$$

The first terms on both sides are equal as given by Equation (2.63) and they drop from the equation. The last term on the left hand side can be dropped since it is a second order variation. Consequently, we obtain

$$\nabla \cdot \left(\sigma_0 \nabla(\Delta\varphi)\right) = -\nabla \cdot (\Delta\sigma \nabla \varphi_0) + \nabla(\Delta\sigma) \cdot \vec{v} \times \vec{B} \tag{2.65}$$

with the following boundary condition:

$$\frac{\partial(\Delta\varphi)}{\partial n} = 0 \quad on\ S\ and\ S_T$$

When σ_0 is initially assumed homogeneous, then a simplified form is obtained

$$\sigma_0 \nabla^2(\Delta\varphi) = \nabla(\Delta\sigma) \cdot \left(-\nabla \varphi_0 + \vec{v} \times \vec{B}\right) \tag{2.66}$$

It is observed that the variation in the scalar potential is determined by the scalar product of the gradient in conductivity distribution (normalized to conductivity σ_0) and the total electric field obtained for the initial conductivity.
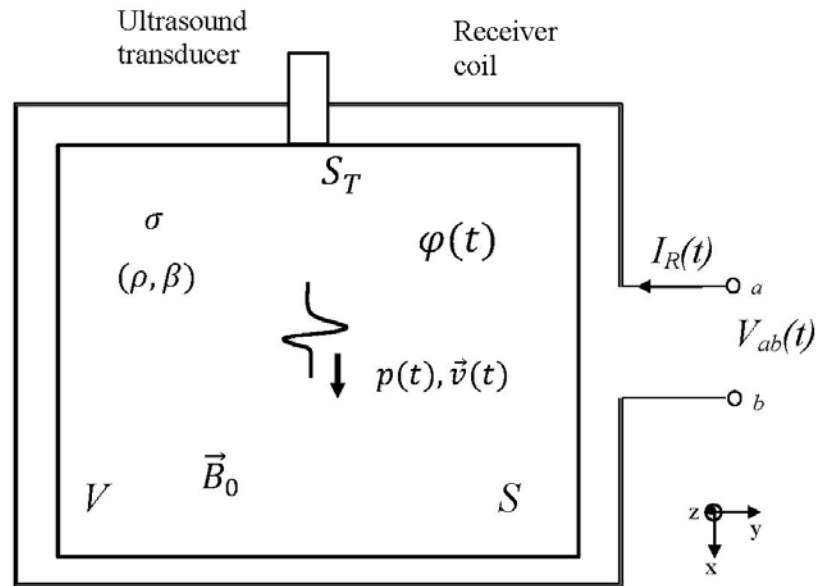
Figure 2-3 Problem geometry of the proposed approach. The changes in the magnetic field are measured using a coil encircling the body or placed nearby the body.

2.8.2 Magnetic Field Measurements (Proposed Approach)

Problem geometry for the proposed approach is shown in Figure 2.3. The magnetic field due to ultrasonically induced Lorentz fields is to be measured using an external coil. Based on the simplified formulation presented in Section 2.4, the behavior of the magnetic field is investigated. Similar to the analysis performed for Hall Effect Imaging, the governing equations for the magnetic flux density are derived for homogeneous and inhomogeneous conductivity distributions.

2.8.2.1 Magnetic Field Measurements for homogeneous and inhomogeneous conductivity distributions

The behavior of the initially applied magnetic field $\vec{B}_0$ is investigated using Equation (2.2). Since $\vec{B}_0$ is static and its source is outside the conductive body and measurement site,

$$\nabla \times \vec{B}_0 = 0 \tag{2.67}$$

Taking the curl of both sides,

$$\nabla \times \nabla \times \vec{B}_0 = 0 \tag{2.68}$$

In the case of ultrasonically induced Lorentz fields in a conductive body, velocity ($\vec{J}_L = \sigma \vec{E}_L = \sigma(\vec{v} \times \vec{B})$) and conduction ($-\sigma \nabla \varphi$) currents change the total magnetic flux density to $\vec{B}(t) = \vec{B}_0 + \vec{b}(t)$. Using Equation (2.2) for $\vec{B}(t)$ and neglecting the displacement currents, we obtain

$$\nabla \times \vec{B} = -\mu_0 \sigma \nabla \varphi + \mu_0 \sigma(\vec{v} \times \vec{B}) \tag{2.69}$$

Applying the curl operator to both sides,

$$\nabla \times \nabla \times \vec{B} = \mu_0 \nabla \times \left[-\sigma \nabla \varphi + \sigma(\vec{v} \times \vec{B}) \right] \tag{2.70}$$

Replacing $\vec{B}(t)$ with $\vec{B}_0 + \vec{b}(t)$ and using Equation (2.67), it is possible to write a differential equation for $\vec{b}(t)$ as follows:

$$\nabla \times \nabla \times \vec{b} = \mu_0 \nabla \times \left[-\sigma \nabla \varphi + \sigma(\vec{v} \times (\vec{B}_0 + \vec{b})) \right] \tag{2.71}$$

The velocity current on the right hand side can be approximated as

$$\sigma \left(\vec{v} \times \vec{B} \right) \approx \sigma(\vec{v} \times \vec{B}_0)$$

as $|b(t)|$ is much smaller compared to $|B_0|$. Thus, the first order Born approximation for $\vec{b}(t)$ can be obtained using the following equation:

$$\nabla \times \nabla \times \vec{b} = \mu_0 \nabla \times \left[-\sigma \nabla \varphi + \sigma \left(\vec{v} \times \vec{B}_0\right)\right] \tag{2.72}$$

When the body has an initial conductivity distribution σ_0, the equation for the corresponding field $\vec{b}_0$ is

$$\nabla \times \nabla \times \vec{b}_0 = \mu_0 \nabla \times \left[-\sigma_0 \nabla \varphi_0 + \sigma_0 \left(\vec{v} \times \vec{B}_0\right)\right] \tag{2.73}$$

An expression for the first order variation in the magnetic flux density $\Delta \vec{b}(t)$ can be obtained when $\vec{b}$, φ and σ terms in Equation (2.72) are replaced by $\vec{b}_0 + \Delta \vec{b}$, $\varphi_0 + \Delta \varphi$ and $\sigma_0 + \Delta \sigma$, respectively. In such a case,

$$\nabla \times \nabla \times \left(\vec{b}_0 + \Delta \vec{b}\right) = \mu_0 \nabla \times \begin{bmatrix} -(\sigma_0 + \Delta \sigma)(\nabla \varphi_0 + \Delta \varphi) \\ +(\sigma_0 + \Delta \sigma)\left(\vec{v} \times \vec{B}_0\right) \end{bmatrix} \tag{2.74}$$

or

$$\nabla \times \nabla \times \vec{b}_0 + \nabla \times \nabla \times \Delta \vec{b} = -\nabla \times (\sigma_0 \nabla \varphi_0) - \nabla \times \left(\sigma_0 \nabla (\Delta \varphi)\right) - \nabla \times$$
$$(\Delta \sigma \nabla \varphi_0) - \nabla \times \left(\Delta \sigma \nabla (\Delta \varphi)\right) + \nabla \times \sigma_0 \left(\vec{v} \times \vec{B}_0\right) + \nabla \times \Delta \sigma \left(\vec{v} \times \vec{B}_0\right) \tag{2.75}$$

Reorganizing the terms on the right hand side, we obtain

$$\nabla \times \nabla \times \vec{b}_0 + \nabla \times \nabla \times \Delta \vec{b}$$
$$= \sigma_0 \nabla \times \left(-\nabla \varphi_0 + \vec{v} \times \vec{B}_0\right) - \nabla \times \left(\sigma_0 \nabla (\Delta \varphi)\right) - \nabla \times (\Delta \sigma \nabla \varphi_0)$$
$$- \nabla \times \left(\Delta \sigma \nabla (\Delta \varphi)\right) + \nabla \times \Delta \sigma \left(\vec{v} \times \vec{B}_0\right) \tag{2.76}$$

The first terms on both sides are equal as given by Equation (2.73). Neglecting the second order variations (the fourth term on the right hand side) one obtains a general

35

relation between the first order variation in the flux density and perturbation in conductivity:

$$\nabla \times \nabla \times \Delta \vec{b} = -\nabla \times \left(\sigma_0 \nabla(\Delta\varphi)\right) - \nabla \times (\Delta\sigma\nabla\varphi_0) + \nabla \times \Delta\sigma\left(\vec{v} \times \vec{B}_0\right) \quad (2.77)$$

or using the vector identity $\nabla \times \left(P\vec{A}\right) = \nabla P \times \vec{A} + P\nabla \times \vec{A}$,

$$\nabla \times \nabla \times \Delta\vec{b} = -\nabla\sigma_0 \times \left(\nabla(\Delta\varphi)\right) - \sigma_0\nabla \times \left(\nabla(\Delta\varphi)\right) - \nabla \times (\Delta\sigma\nabla\varphi_0)$$

$$+\nabla \times \Delta\sigma\left(\vec{v} \times \vec{B}_0\right) \quad (2.78)$$

Since curl of gradient of a function is zero the second term on the right hand side drops. When the initial conductivity is homogeneous ($\sigma_0 = $ constant), the first term on the right is zero. Consequently, one obtains the following expression that relates the first order variation in magnetic flux density to the conductivity perturbation:

$$\nabla \times \nabla \times \Delta\vec{b}(t) = \nabla \times \left[\Delta\sigma\left(-\nabla\varphi_0 + \vec{v}(t) \times \vec{B}_0\right)\right] \quad (2.79)$$

2.8.3 Lead-Field analysis:

The measured data in the proposed approach are the voltages picked up from the receiver coil (Figure 2-3). The relation between the receiver coil voltage and magnetic flux density is given by the Faraday's law of induction:

$$v_{ab}(t) = -\int_{Coil} \frac{\partial\vec{B}}{\partial t} \cdot d\vec{S} \quad (2.80)$$

where $d\vec{S}$ is the differential surface element in the surface enclosed by the receiver coil. Since $\vec{B}(t)$ is related to the conductivity distribution in the body, the received voltage is a function of the conductivity distribution. The above equation, however, does not show this relation explicitly. To obtain such a relation, in this thesis study, an approach that is frequently used in formulating the forward problem of

magnetoencephalography (MEG) is used. This approach is based on the *reciprocity theorem* [45]. In short, this theorem states that the location of the detector and source can be changed without affecting the detected signal amplitude. Using this theorem, the detected signal is expressed in terms of volume integral of the source (dipole) distribution. The sensitivity of the measurement to a specific dipole is determined by the scalar product of a *lead-field vector* (the electric field generated by a reciprocal unit current in the detector coil) with the selected dipole. Thus, once the lead field vector is solved for specific detector geometry, the detector voltage for an arbitrary dipole source can be easily calculated by integrating over the source domain.

Similar approach can be applied if the lead field vector for the proposed imaging modality can be identified. In the following sections, the lead field vector will be found for electromagnetic fields with 1) harmonic time dependence, and 2) general time dependence.

2.8.3.1 Harmonic time dependence:

A straightforward extension of this imaging modality is to excite the ultrasonic transducer with its resonance frequency continuously. The pick-up voltage at the receiver coil is then the steady state response (a single measurement) obtained for a specific transducer/receiver coil configuration. To increase the number of measurements, the transducer and receiver coil configurations should be changed. Though the measurement strategy is somehow difficult for continuous excitation, the analysis for the lead field vector analysis is relatively simple.

In the direct problem, $\vec{E}_1$ and $\vec{H}_1$ represent the electric field and magnetic field in the body when currents are ultrasonically induced in the body. Assuming $e^{j\omega t}$ time dependence and adopting the boldface phasor notation, the following equations are valid,

$$\nabla \times \vec{E}_1 = -j\omega\mu_0 \vec{H}_1 \qquad (2.81)$$

37

$$\nabla \times \vec{H}_1 = \sigma\vec{E}_1 + \vec{J}_1 \tag{2.82}$$

where $\vec{J}_1 = \sigma(v \times \vec{B}_0)$ denotes the velocity current due to ultrasonic excitation under a static magnetic field.

In the reciprocal problem there are no current sources in the body. The electric field $\vec{E}_2$ and the magnetic field intensity $\vec{H}_2$ are generated inside the body due to a reciprocal current density $\vec{J}_2$ (or $\vec{J}_R$) inside the receiver coil of the direct problem. In the reciprocal problem the following equation must be satisfied:

$$\nabla \times \vec{E}_2 = -j\omega\mu_0\vec{H}_2 \tag{2.83}$$

$$\nabla \times \vec{H}_2 = \sigma\vec{E}_2 + \vec{J}_2 \tag{2.84}$$

Using Equations (2.81) and (2.84) one obtains the following equation:

$$\vec{H}_2 \cdot \nabla \times \vec{E}_1 - \vec{E}_1 \cdot \nabla \times \vec{H}_2 = -j\omega\mu_0\vec{H}_1 \cdot \vec{H}_2 - \sigma\vec{E}_2 \cdot \vec{E}_1 - \vec{J}_2 \cdot \vec{E}_1 \tag{2.85}$$

Similarly, using Equations (2.82) and (2.83) we obtain

$$\vec{H}_1 \cdot \nabla \times \vec{E}_2 - \vec{E}_2 \cdot \nabla \times \vec{H}_1 = -j\omega\mu_0\vec{H}_1 \cdot \vec{H}_2 - \sigma\vec{E}_2 \cdot \vec{E}_1 - \vec{J}_1 \cdot \vec{E}_2 \tag{2.86}$$

Using the vector identity $\nabla \times (\vec{A} \times \vec{B}) = \vec{B} \cdot (\nabla \times \vec{A}) - \vec{A} \cdot (\nabla \times \vec{B})$, the left hand sides of (2.85) and (2.86) are simplified and equations are put in the following form:

$$\nabla \cdot (\vec{E}_1 \times \vec{H}_2) = -j\omega\mu_0\vec{H}_1 \cdot \vec{H}_2 - \sigma\vec{E}_2 \cdot \vec{E}_1 - \vec{J}_2 \cdot \vec{E}_1 \tag{2.87}$$

$$\nabla \cdot (\vec{E}_2 \times \vec{H}_1) = -j\omega\mu_0\vec{H}_1 \cdot \vec{H}_2 - \sigma\vec{E}_2 \cdot \vec{E}_1 - \vec{J}_1 \cdot \vec{E}_2 \tag{2.88}$$

By subtracting Equation (2.88) from Equation (2.87),

$$\nabla \cdot (\vec{E}_1 \times \vec{H}_2) - \nabla \cdot (\vec{E}_2 \times \vec{H}_1) = \vec{J}_1 \cdot \vec{E}_2 - \vec{J}_2 \cdot \vec{E}_1 \tag{2.89}$$

Taking the volume integral in all universe (in volume V_∞ bounded by S_∞) we obtain

$$\int_{V_\infty} \nabla \cdot (\vec{E}_1 \times \vec{H}_2 - \vec{E}_2 \times \vec{H}_1)dV = \int_{V_\infty} (\vec{J}_1 \cdot \vec{E}_2 - \vec{J}_2 \cdot \vec{E}_1)dV \tag{2.90}$$

38

By applying the divergence theorem to the left hand side it becomes a surface integral,

$$\int_{V_\infty} \nabla \cdot (\vec{E}_1 \times \vec{H}_2 - \vec{E}_2 \times \vec{H}_1) dV = \oint_{S_\infty} \vec{E}_1 \times \vec{H}_2 - \vec{E}_2 \times \vec{H}_1 dS \qquad (2.91)$$

Since the electric and magnetic field intensities vanish at infinity, we obtain the well-known reciprocity relation:

$$\int_{V_\infty} (\vec{J}_1 \cdot \vec{E}_2 - \vec{J}_2 \cdot \vec{E}_1) dV \qquad (2.92)$$

Since the current density $\vec{J}_1$ in the direct problem is nonzero in the conducting body volume (V_{body}) and the current density $\vec{J}_2$ in the reciprocal problem is nonzero in the receiver coil volume (V_{coil}), Equation (2.92) reduces to the following:

$$\int_{V_{body}} \vec{J}_1 \cdot \vec{E}_2 \, dV = \int_{V_{coil}} \vec{J}_2 \cdot \vec{E}_1 \, dV \qquad (2.93a)$$

Recognizing that $\vec{J}_2 dV = I_R d\vec{l}$, the right hand side becomes

$$\int_{V_{body}} \vec{J}_1 \cdot \vec{E}_2 \, dV = I_R \int_{V_{coil}} \vec{E}_1 \cdot d\vec{l} \qquad (2.93b)$$

The integral on the right hand side is the pick-up voltage V_{ab} due to ultrasonically induced harmonic currents in the body. Consequently, V_{ab} is expressed as follows:

$$V_{ab} = \int_{V_{body}} \vec{J}_1 \cdot (\vec{E}_R / I_R) dV \qquad (2.94)$$

where $\vec{E}_2$ is replaced by $\vec{E}_R$. The term in the parenthesis is the electric field in the reciprocal problem when unit current is applied to the receiver coil and it is called as the *lead field vector* ($\vec{L}_M$) for the forward problem of the proposed imaging modality. The subscript M in the lead field vector shows that it is the lead field vector for the

magnetic field measurements. Note that the lead-field vector itself is a function of body conductivity.

To show the relation between the pick-up voltage and conductivity in the medium, the term $\vec{J}_1$ is replaced by $\sigma(v \times \vec{B}_0)$ and the final form is obtained:

$$V_{ab} = \int_{V_{body}} \sigma\left(v \times \vec{B}_0\right) \cdot \vec{L}_M(\sigma)dV \tag{2.95}$$

Note that the pick-up voltage is linearly proportional to the conductivity distribution and the weight of each conductive element is determined by the dot product of the Lorentz field and reciprocal field on that element.

2.8.3.2 General time dependence:

When general time dependence is assumed for the particle velocity $\vec{v}(t)$, the reciprocity relation given in Equation (2.92) does not hold. Instead, the following relation is valid [46]:

$$\int_{-\infty}^{\infty} dt \int_{V_{body}} dV \, \vec{J}_1(\vec{r}, \tau - t) \cdot \vec{E}_2\left(\vec{r}, t\right)$$

$$= \int_{-\infty}^{\infty} dt \int_{V_{coil}} dV \, \vec{J}_2(\vec{r}, t) \cdot \vec{E}_1\left(\vec{r}, \tau - t\right) \tag{2.96}$$

In this expression, $\vec{E}_1$ is the electric field in the direct problem due to velocity current $\vec{J}_1 = \sigma\left(\vec{v}(t) \times \vec{B}\right)$ and $\vec{E}_2$ is the electric field in the reciprocal problem due to reciprocal current $\vec{J}_2 = \vec{J}_R$ in the receiver coil. Here $\vec{r}$ represents the three-dimensional position vector as given in the original article.

For the receiver coil, we may write

$$\int_{V_{coil}} dV\, \vec{J}_R(t) = \int_{Coil} d\vec{l}\, I_R(t)$$

Then the right hand side of equation (2.96) becomes,

$$\int_{-\infty}^{\infty} dt\, I_R(t) \int_{Coil} E_1(\tau - t) \cdot d\vec{l} = \int_{-\infty}^{\infty} dt\, I_R(t) V_{ab}(\tau - t) = I_R * V_{ab} \qquad (2.97)$$

For the left hand side of Equation (2.96), we recognize that the electric field $\vec{E}_R(\vec{r}, t)$ in the reciprocal problem can be written as the product of a position dependent function and energizing reciprocal current $I_R(t)$:

$$\vec{E}_R(\vec{r}, t) = \vec{E}_R^0(\vec{r}) \frac{\partial}{\partial t}(I_R(t)) \qquad (2.98)$$

where $\vec{E}_R^0(\vec{r})$ is the reciprocal electric field normalized with reciprocal current in the receiver coil. Since the body is assumed resistive, Equation (2.98) should be valid. Consequently, we obtain

$$\int_{-\infty}^{\infty} dt \int_{V_{body}} dV\, \vec{J}_1(\vec{r}, \tau - t) \cdot \vec{E}_R(\vec{r}, t) = \int_{-\infty}^{\infty} dt\, \frac{\partial}{\partial t} I_R(t) \int_{V_{body}} dV\, \vec{J}_1(\vec{r}, \tau - t) \cdot \vec{E}_R^0(\vec{r}) \quad (2.99)$$

Let $I'_R(t)$ denotes $\frac{\partial}{\partial t} I_R(t)$. Then the pick-up voltage v_{ab} is obtained as follows:

$$I_R * v_{ab} = \int_{V_{body}} \left[\int_{-\infty}^{\infty} dt\, I'_R(t) L_M(\vec{r}, \tau - t) \right] dV \qquad (2.100)$$

where $L_M(\vec{r}, \tau - t) = \vec{J}_1(\vec{r}, \tau - t) \cdot \vec{E}_R^0(\vec{r})$. Assume that $I_R(t) = tu(t)$, where $u(t)$ is the unit step function. Taking the time derivative with respect to τ of both sides of (2.100), the left hand side becomes:

$$\frac{\partial}{\partial \tau}(I_R(\tau) * v_{ab}(\tau)) = v_{ab}(\tau) * \frac{\partial}{\partial t} I_R(\tau) \qquad (2.101)$$

$$v_{ab}(\tau) * u(\tau) = \int_{-\infty}^{\infty} u(t)\, v_{ab}(\tau - t) dt = \int_{-\infty}^{\infty} v_{ab}(\tau - t) dt \qquad (2.102)$$

The right hand side of (2.100) becomes:

$$\frac{\partial}{\partial \tau} \int_{V_{body}} \left[\int_{-\infty}^{\infty} dt \ I'_R(t) L_M(\vec{r}, \tau - t) \right] dV = \int_{V_{body}} \left[\int_{-\infty}^{\infty} dt \frac{\partial}{\partial \tau} L_M(\vec{r}, \tau - t) \right] dV \qquad (2.103)$$

Rewriting equation (2.100):

$$v_{ab}(\tau - t) = \int_{V_{body}} \left[\int_{-\infty}^{\infty} dt \frac{\partial}{\partial \tau} L_M(\vec{r}, \tau - t) \right] dV$$

The pick-up voltage is then obtained as:

$$v_{ab}(\tau - t) = \int_{V_{body}} \frac{\partial}{\partial \tau} L_M(\vec{r}, \tau - t) \ dV \qquad (2.104)$$

A final form of this equation can be obtained by 1) changing the variables for the time variation, 2) dropping the position vector $\vec{r}$, 3) expressing $\vec{J}_1$ in terms of particle velocity, and 4) setting $\vec{E}_R^0 = \vec{E}_R^0(\sigma)$.

$$v_{ab}(t) = \int_{V_{body}} \frac{\partial}{\partial \tau} \left(\sigma(\vec{v}(t) \times \vec{B}) \cdot \vec{E}_R^0(\sigma) \right) \qquad (2.105)$$

2.9 Receiver coil design considerations

When the ultrasonic transducer position is fixed, the sensitivity in the measurements can be increased by optimizing the reciprocal field distribution. However, even for a fixed transducer position ultrasonic beam steering approaches are applicable using an ultrasound array. Thus, in order to use a different receiver coil for each beam direction, one should be able to acquire the best available data for any propagation direction. This can be achieved by using two coils for data acquisition, namely, x- and y-coils which are sensitive to acoustic propagation in x- and y-directions, respectively. Figure 2.4 and Figure 2.5 shows two realizable coil configurations encircling the body for the development of x- and y-coils.
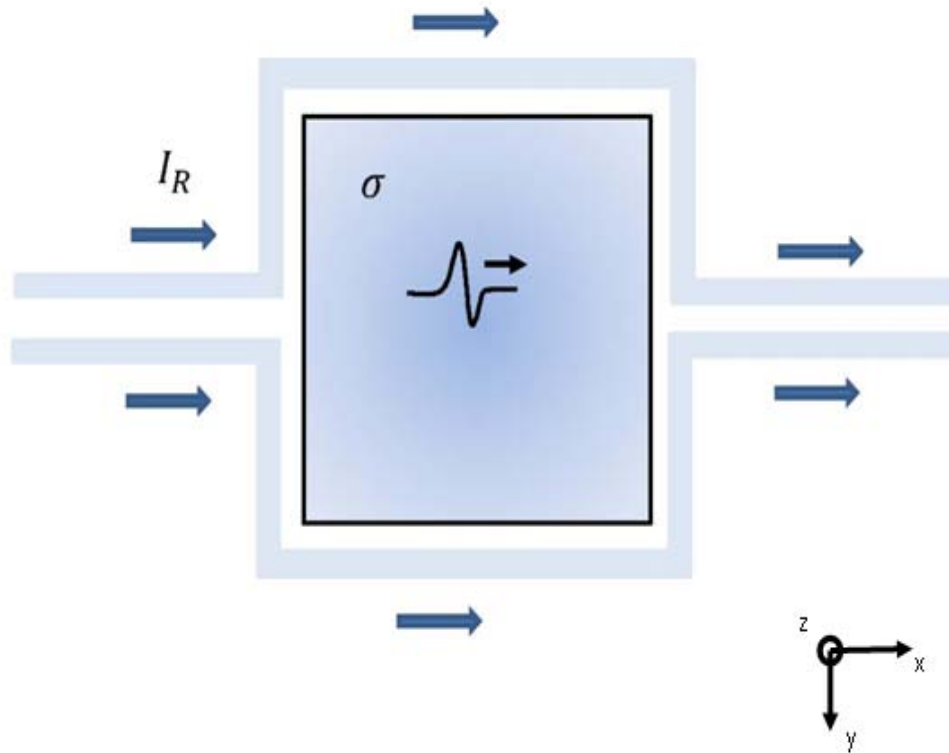
Figure 2-4 x-coil configuration encircling a conductive body of conductivity σ. x-coil is sensitive to an acoustic pulse propagating in the x-direction. The energizing current I_R for the reciprocal problem is also shown.
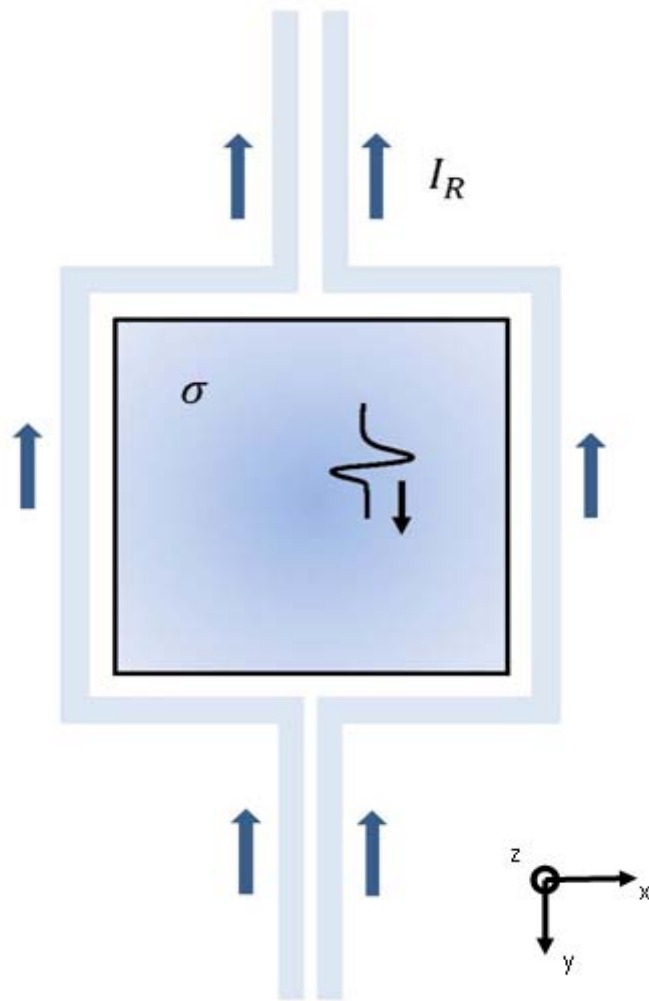
Figure 2-5 y-coil configuration encircling a conductive body of conductivity σ. y-coil is sensitive to an acoustic pulse propagating in the y-direction. The energizing current I_R for the reciprocal problem is also shown.

CHAPTER 3

NUMERICAL MODELING OF THE FORWARD PROBLEM

3.1 Introduction

The proposed imaging modality is based on the Lorentz fields generated by applying ultrasound in the existence of the static magnetic field. The general formulation of the partial differential equations for the scalar and magnetic vector potentials, for the acoustic pressure and for piezoelectricity are explained in Chapter 2. In this chapter, the numerical modeling of the forward problem is described.

To solve the forward problem numerically the COMSOL Multiphysics 3.3 is [44]used. COMSOL is an engineering simulation software environment that gives opportunities of defining geometry of the problem, meshing, specifying the physics, then solving and visualizing the results using post processing [44] tools. To solve the multiphysics problems different modules of COMSOL are employed. In our problem three coupled problems, namely, acoustic, piezoelectric and electromagnetic problems are solved. The related module of each problem is performed by specifying the properties of physics with the coupling parameters, as described below.

3.2 Pressure Acoustic Module

Pressure Acoustics module, a sub-category of Acoustic Module, is used to describe the acoustic properties of each subdomain and boundary conditions. Figure 3-1 shows the geometry of model. In this model, there are four subdomains, namely, normal tissue (Ω_1), tumor (Ω_2), ultrasonic transducer (Ω_3), and surrounding air (Ω_4).

The boundaries of each domain are denoted by $\partial\Omega_1, \partial\Omega_2, \partial\Omega_3$, and $\partial\Omega_4$, respectively.
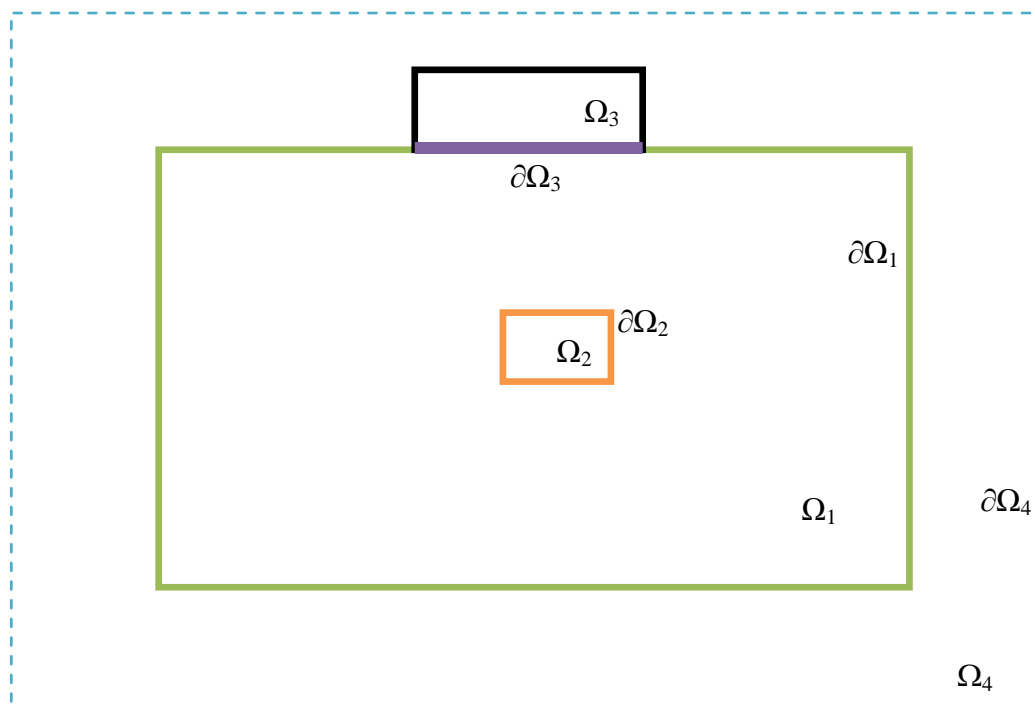
Figure 3-1 Geometry of the acoustic (pressure) problem. Subdomains $\Omega_1, \Omega_2, \Omega_3, \Omega_4$ and associated boundaries $\partial\Omega_1, \partial\Omega_2, \partial\Omega_3, \partial\Omega_4$ represent the normal tissue, tumor, piezoelectric transducer and air, respectively.

The general formulation of the sound waves in a lossless medium for acoustic pressure, p, is given in Equation (2.41). In COMSOL, it is represented as follows:

$$\frac{1}{\rho_0 c_s^2} \frac{\partial^2 p}{\partial t^2} + \nabla \cdot \left[-\frac{1}{\rho_0} (\nabla p - \vec{q}) \right] = Q \tag{3.1}$$

here ρ (kg/m^2) is the density of the medium, c_s (m/s) is the speed of sound. $\vec{q}$ (N/m^3) and Q(1/s^2) represent the (optional) dipole and monopole sources, respectively. In our case there is no monopole source, so the right hand side of the Equation (3.1) is zero. However, there are mechanical forces, such as gravitation and vibration due to Lorentz fields that can be represented as dipole sources. In this study, the body is assumed to stay stationary in space due to external forces, and the effects of gravitational force are ignored.

The Lorentz force (per unit volume) $\vec{q} = \vec{J} \times \vec{B}$, due to the presence of current density $\vec{J}$ and magnetic flux density $\vec{B}$, is nonzero and must appear in the formula. This source term also shows the coupling between acoustic pressure and electromagnetic problems.

Boundary Conditions: There are four different boundaries as shown in Figure 3-1. The properties of each boundary are given below:

On $\partial\Omega_1$ and $\partial\Omega_2$: These boundaries express the continuity of the normal acceleration. The resulting equation is:

$$\vec{n} \cdot \left(\frac{1}{\rho} (\nabla p - \vec{q}) \right)_1 - \vec{n} \cdot \left(\frac{1}{\rho} (\nabla p - \vec{q}) \right)_2 = 0 \tag{3.2}$$

or

$$\vec{n} \cdot \left(\frac{1}{\rho} (\nabla p - \vec{q}) \right)_1 = \vec{n} \cdot \left(\frac{1}{\rho} (\nabla p - \vec{q}) \right)_2 \tag{3.3}$$

On $\partial\Omega_3$: This boundary is the common boundary between the normal tissue and ultrasonic transducer. The ultrasonic pressure is produced from this boundary. It is the boundary where the coupling between the acoustic (pressure) module and piezoelectric module occurs. Since the ultrasonic transducer is excited with a specific voltage at this boundary, the displacement occurs in x-, y- and z-directions. The

47

normal component of the acceleration in the direction of propagation is assigned as follows:

$$\vec{n} \cdot \left(\frac{1}{\rho} (\nabla p - \vec{q}) \right) = a_n \tag{3.4}$$

where a_n represents the inward acceleration. It is obtained as the second time derivative of the displacement at the lower boundary of the crystal in the piezoelectric problem.

On $\partial\Omega_4$: With this boundary condition, the reflections on the boundary are ignored:

$$\vec{n} \cdot \left(\frac{1}{\rho} (\nabla p - \vec{q}) \right) + \frac{1}{c\rho} \frac{\partial p}{\partial t} = \frac{(1 - (\vec{n}_k \cdot \vec{n}))}{c\rho} \cdot \frac{\partial p_0}{\partial t} \tag{3.5}$$

Here p_0 is the pressure source, $\vec{q}$ represents a dipole source and $\vec{n}_k$ denotes the wave direction. Since the body is assumed lossless, the second term on the left hand side of Equation (3.5) is zero. Furthermore, since there are no external pressure sources Equation (3.5) can be rewritten as:

$$\vec{n} \cdot \left(\frac{1}{\rho} (\nabla p - \vec{q}) \right) = 0 \tag{3.6}$$

3.3 Piezoelectric Module

The piezoelectric effect is defined as the transfer of electrical to mechanical energy and vice versa. It is described in the COMSOL manuals as: "Direct piezoelectric effect consists of an electric polarization in a fixed direction, as the piezoelectric crystal is deformed. This polarization is proportional to the deformation and causes an electric potential difference over the crystal. Inverse piezoelectric effect consists of the opposite of direct effect. This means that an applied potential difference induces a deformation of the crystal." [44]

In this study, the inverse piezoelectric effect is employed. By applying a potential difference to the piezoelectric crystal, a deformation that causes pressure on the body is generated.

There are two mathematical forms to express the piezoelectric effects: Stress-charge and Strain-charge. These forms give the relation between the stress, strain, electric field and electrical displacement fields. Stress is known as the load per unit area acting within a material whereas the strain is the change in shape of an object in response to stress. The stress-charge and strain charge relations are as follows:

Stress- Charge:

$$\mathbf{T} = c_E \mathbf{S} - e^T \mathbf{E}$$
$$\mathbf{D} = e\mathbf{S} + \varepsilon_s \mathbf{E}$$

(3.7)

Strain- Charge:

$$\mathbf{S} = s_E \mathbf{T} + d^T \mathbf{E}$$
$$\mathbf{D} = d\mathbf{T} + \varepsilon_T \mathbf{E}$$

(3.8)

where $\mathbf{S}$, $\mathbf{T}$, $\mathbf{E}$, and $\mathbf{D}$ are vectors comprising x-, y-, and z-components of the strain, stress, electric field and the displacement field, respectively. c_E, ε and d are elasticity, piezoelectric stress and piezoelectric strain matrices.

To define the piezoelectric properties of the ultrasonic transducer and set the boundary conditions, the following model (Figure 3-2) is used. In this model, it is assumed that only Ω_3 has the piezoelectric properties.
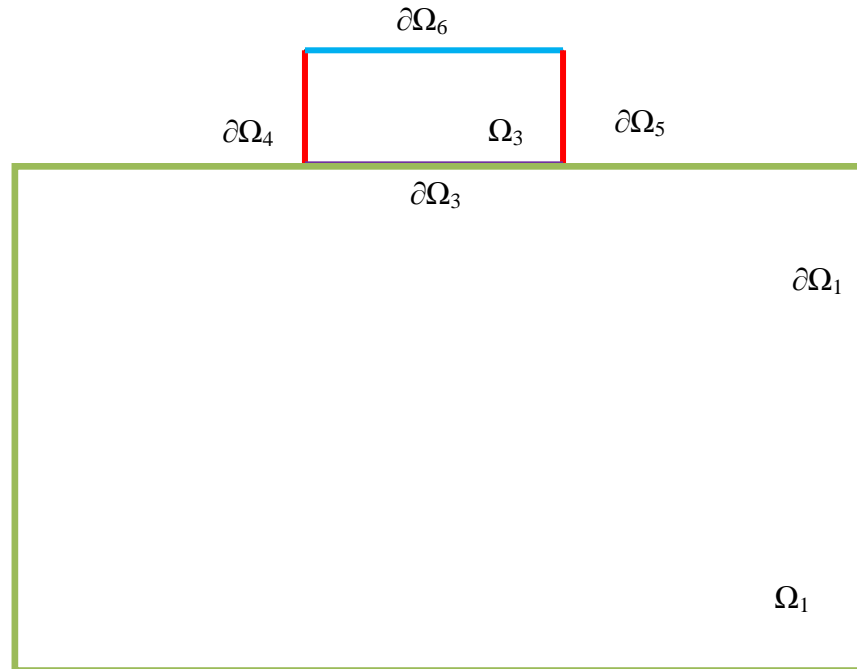
Figure 3-2 Geometry for the piezoelectric module. Subdomains Ω_1, and Ω_3 represent the normal tissue and the piezoelectric transducer, respectively. $\partial\Omega_1$ is the boundary of the normal tissue. $\partial\Omega_3$ represents the surface of the crystal used for voltage application. On $\partial\Omega_4$ and $\partial\Omega_5$ the normal component of the electrical displacement is assumed zero. $\partial\Omega_6$ serves as ground for the electrical problem.

__Electrical Boundary Conditions:__

On $\partial\Omega_3$: (Electric Potential) This boundary condition specifies the voltage applied. Since the piezoelectric problem solves for the potential distribution, the value of the potential at this boundary should be defined.

On $\partial\Omega_6$: (Ground) This boundary condition specifies the ground surface.

On $\partial\Omega_4$ and $\partial\Omega_5$: (Zero Charge/Symmetry) These boundaries specify that the normal component of the electric displacement is zero as $\vec{n} \cdot \vec{D} = 0$.

The boundary $\partial\Omega_1$ is not a common boundary between the piezoelectric transducer and conductive body/tissue. Since the body has no piezoelectric property, this boundary is passive.

Mechanical Boundary Conditions:

On $\partial\Omega_3$, $\partial\Omega_4$ and $\partial\Omega_5$: (Free) It is a standard mechanical boundary condition. Initially it is applied to all boundaries of the domains governed by the piezoelectric interface. It defines the boundary as free to move in any direction without any loads acting on in.

On $\partial\Omega_6$: (Roller) It opposes the standard mechanical condition (free). It specifies that there is no displacement perpendicular to the boundary, but tangential displacements are allowed.

3.4 Electromagnetic Module

In this module, the electromagnetic analysis is performed by solving the Maxwell's equations. The detailed information about the Maxwell's equations is given in Chapter 2. In the forward problem of this thesis study, initially, there is only static magnetic field and there is no electric field in the body. Coupled with the acoustic signal, an electric field, called Lorentz electric field, and current density is formed in the conductive body/tissue. The geometry of electromagnetic problem is shown in Figure 3-3.

In this module, quasi-static analysis is preformed under the assumption that $\frac{\partial \vec{D}}{\partial t} = 0$, namely, the displacement currents are assumed negligible. The partial differential equations governing the behavior of the scalar and magnetic vector potentials are

given in detail in Chapter 2. The final equation to be solved in the electromagnetic module is given in Equation (2.24). The representation of this equation in COMSOL (AC-DC Module, Quasistatic, In Plane Induction and Magnetic Fields) is:

$$\frac{\partial \mu_0 \mu_r \vec{H}}{\partial t} + \frac{\partial \vec{B}_r}{\partial t} + \nabla \times \left(\sigma^{-1}\left(\nabla \times \vec{H} - \vec{J}^e\right) - \vec{v} \times \left(\mu_0 \mu_r \vec{H} + \vec{B}_r\right)\right) = 0 \qquad (3.9)$$
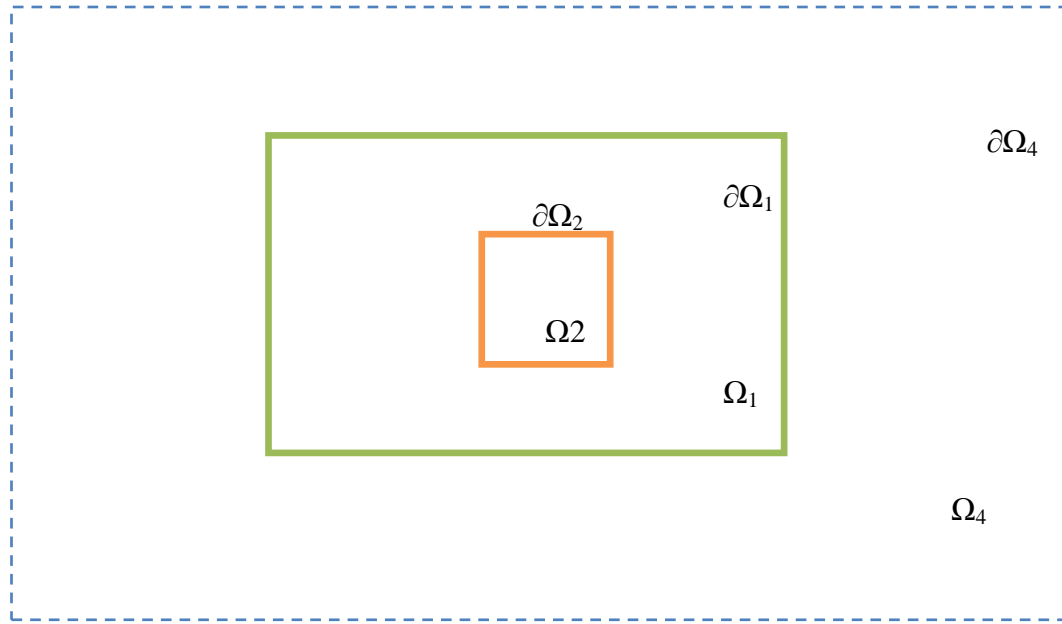
Figure 3-3 Geometry of the electromagnetic problem. Subdomains Ω_1 and Ω_2 are the conductive body and tumor, respectively. Ω_1 represents the air surrounding the body. $\partial\Omega_1$, $\partial\Omega_2$, $\partial\Omega_4$ are boundaries of the conductive tissue, tumor and air, respectively.

Here $\vec{J}^e$ is the external current density and B_r is the remanent flux density. The remanent flux density is defined as the magnetic flux density remaining in a substance in the absence of self-demagnetization field. In this problem, there is neither external current density nor remanent flux density. However, there is a static magnetic flux density (1T) in z-direction. Consequently, the simplified form of Equation (3.9) can be written as follows:

$$\frac{\partial \mu_0 \mu_r \vec{H}}{\partial t} + \nabla \times \left(\sigma^{-1}\left(\nabla \times \vec{H}\right) - \vec{v} \times \left(\mu_0 \mu_r \vec{H}\right)\right) = 0 \qquad (3.10)$$

To solve Equation (3.10), the following boundary conditions are defined:

On $\partial\Omega_1$: On this boundary, the continuity condition is valid, which is the natural boundary condition implying continuity of the tangential component of the electric field:

$$\vec{n} \times (\vec{E}_1 - \vec{E}_2) = 0 \qquad\qquad (3.11)$$

On $\partial\Omega_2$: The same boundary condition (Equation 3.11) is defined on $\partial\Omega_1$.

On $\partial\Omega_4$: On this boundary, the magnetic insulation condition is valid, that sets the tangential component of the electric field zero:

$$\vec{n} \times \vec{E} = 0 \qquad\qquad (3.12)$$

3.5 Coil Configuration

The bridge between the forward and inverse problem is the measurement of the induced fields. For this purpose, one can use different types of measurements, such as electrodes, coils and ultrasound transducers (receiver). In this thesis study, we propose to use magnetic field measurements and introduced a novel coil configuration.

In the proposed coil configuration, there are two similar coils encircling the body as shown in Figure 3-4. Since the resultant current density is in two directions, i.e, x- and y- directions, two coils are employed. The coils are designed to be sensitive in these directions.

To show that the received voltage is a function of conductivity distribution, an approach based on reciprocity theorem is performed. In this theorem it is stated that the location of the detector and source can be changed without affecting the detected signal amplitude.
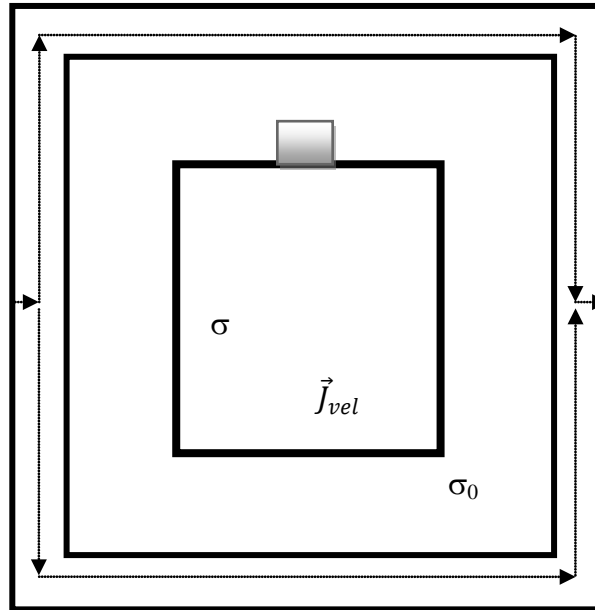
x-coil
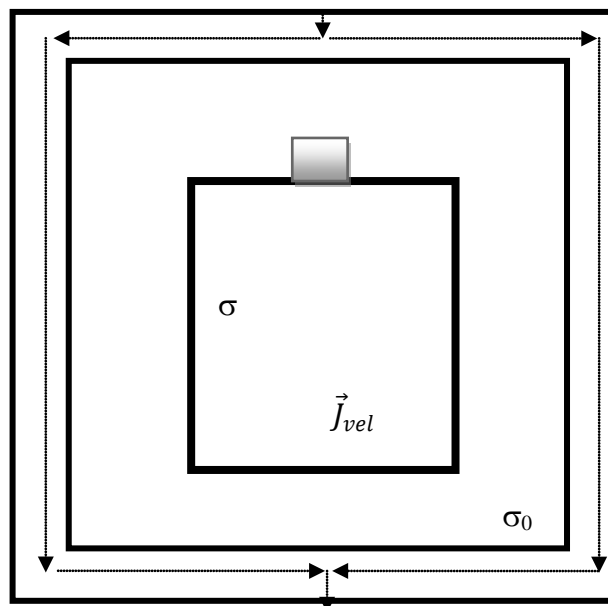
y-coil

Figure3-4   Novel   coil   configuration   to   sense   the   current   density
$(\vec{J}_{vel})$ induced in the conductive body with conductivity σ. The arrows show the path for
current. The coils are encircled the conductive body. The coils are named according to the
sensing direction of currents, as x-coil and y-coil.

The detected signal is expressed in terms of the volume integral of the source (dipole) distribution. To determine the sensitivity of the measurement to a specific dipole the scalar product of a lead vector field with the selected dipole is satisfied. The lead vector field is the electric field generated by a reciprocal unit current in the detector coil. To solve the lead field vector for a specific detector, each detector called as x-coil and y-coil are excited by (reciprocal) unit current. Detailed information about lead field vector is given in Chapter 2.

The simulation of lead field vector is performed by exciting x- and y- coils with unit current (1 A). The detecting coils are encircling the conductive body with 5cm x 5 cm size. The coils simulated in Comsol are represented with lines to show the path of the current.
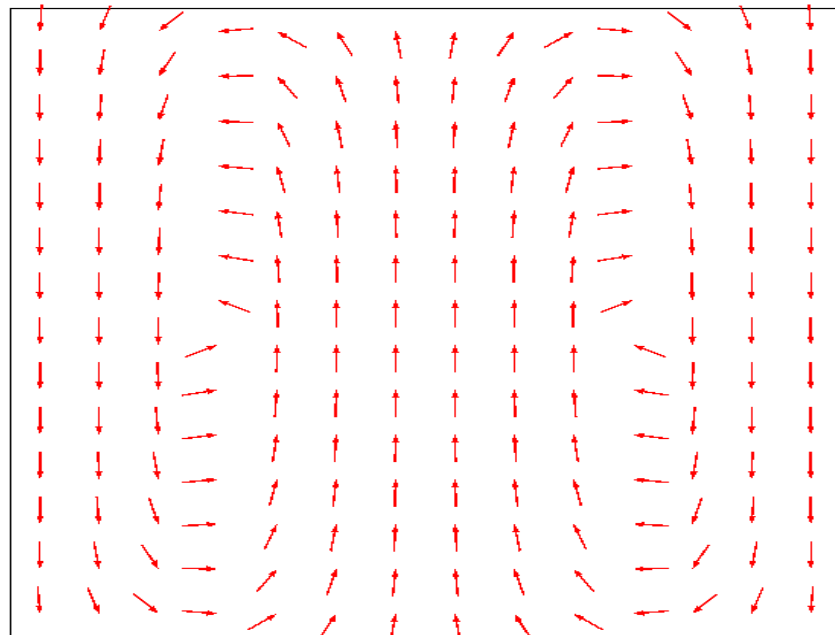
Figure 3-5 Electric field distribution shown with arrows in conductive body by encircling with y-coil configuration and in air.

It is seen from the results of simulations, electric fields induced by y-coil are in y-direction and electric fields induced by x-coil are in x-direction (Figure 3-5 and Figure 3-6). Both of them have maximum electric field distribution around the center of coils. Since the coils encircle the conductive bodies, maximum electric field is induced in the conductive bodies, especially around the center of conductive bodies. If these coils are used as receiver coils, the current in x-direction and y-direction are sensed by x-coil and y-coil, respectively.
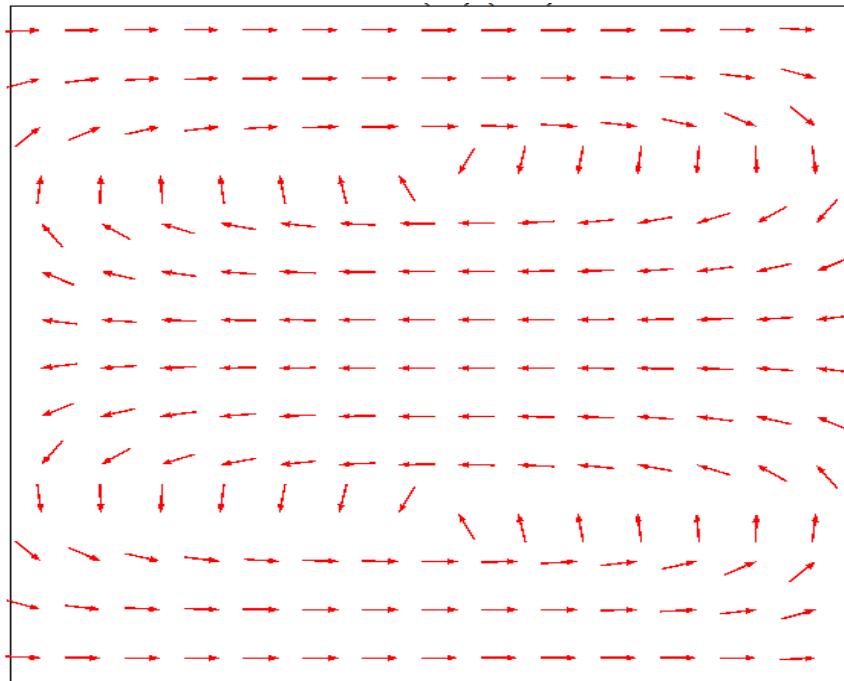
Figure 3-6 Electric field distribution in conductive body encircling with x-coil configuration

3.6 Model Geometry

To make the numerical solutions of proposed coupled problem, 2D model geometry is drawn (Figure 3-7). The geometry consist of ultrasonic transducer, receiver coils (x-coil and y-coil), conductive body, tumor and surrounding air.

3.6.1 Ultrasonic Transducer

As an ultrasonic transducer a single element transducer and 16-element linear phased array transducer is modeled (Figure 3-8). In medical ultrasound ferroelectric materials are used to exhibit the piezoelectric effects. A well-known ferroelectric material PZT is used as a standard transducer material. Detail information about PZT is given in Appendix A. In our simulations we modeled the ultrasonic transducer using PZT-5H material. The properties of PZT-5H are taken from the material library of COMSOL software as given below [44]:

$$c_E = \begin{bmatrix} 127 & 80.2 & 84.7 & 0 & 0 & 0 \\ 80.2 & 127 & 84.7 & 0 & 0 & 0 \\ 84.7 & 84.7 & 117 & 0 & 0 & 0 \\ 0 & 0 & 0 & 23 & 0 & 0 \\ 0 & 0 & 0 & 0 & 23 & 0 \\ 0 & 0 & 0 & 0 & 0 & 23.5 \end{bmatrix} GPa$$

$$e = \begin{bmatrix} 0 & 0 & 0 & 0 & 17.03448 & 0 \\ 0 & 0 & 0 & 17.03448 & 0 & 0 \\ -6.22812 & -6.22812 & -23.2403 & 0 & 0 & 0 \end{bmatrix} \frac{C}{m^2}$$

$$\varepsilon = \begin{bmatrix} 1.3 & 0 & 0 \\ 0 & 1.5 & 0 \\ 0 & 0 & 1.5 \end{bmatrix} \times 10^{-8} \frac{F}{m}$$

3.6.2 Conductive Body and Tumor Modeling

The conductive body and tumor are modeled as 5 cm x 5cm and 5 mm x 5 mm in size, respectively. For conductive body and tumor electrical and acoustic properties of breast fat and blood are represented. Electrical conductivities of breast fat and tumor are 0.0257 S/m and 0.8221 S/m, respectively at 1 MHz For the other tissues

the dielectric permittivity and conductivity values are given in Appendix B at 50 kHz, 100 kHz, 500 kHz and 1 MHz frequencies.

For solving acoustic problem the acoustic properties of bodies/tissues should be defined. The acoustic properties of breast fat and tumor are defined as: density of breast fat is 980 kg/m^3, the speed of sound in it is 1520 m/s; density of tumor is 1040 kg/m^3, the speed of sound in it is 1550 m/s. The acoustic properties of some tissues are given in Appendix B.

3.6.3 Meshing

In finite element modeling mesh size is very important for results. It must be sufficiently small, comparable to the wavelength. It is known that the mesh size is must be 5-10 times smaller than the wavelength of the operating frequency to have exact results. In these simulations, triangular elements are used to mesh the whole geometry. The conductive body and tumor consist of the triangular elements with 2 times smaller than the wavelength in mesh size (Figure 3-8).

The number of mesh elements for each domain is given in Table 3-1.

Table 3-1Number of mesh elements (triangular elements) of each subdomain.

Subdomain	Number of mesh elements
Breast fat (5cm x5cm)	18731
Tumor (5mm x 5mm)	180
Air(1m x1m)	11741
Each crystal of ultrasonic transducer (1 mm x 1mm)	16
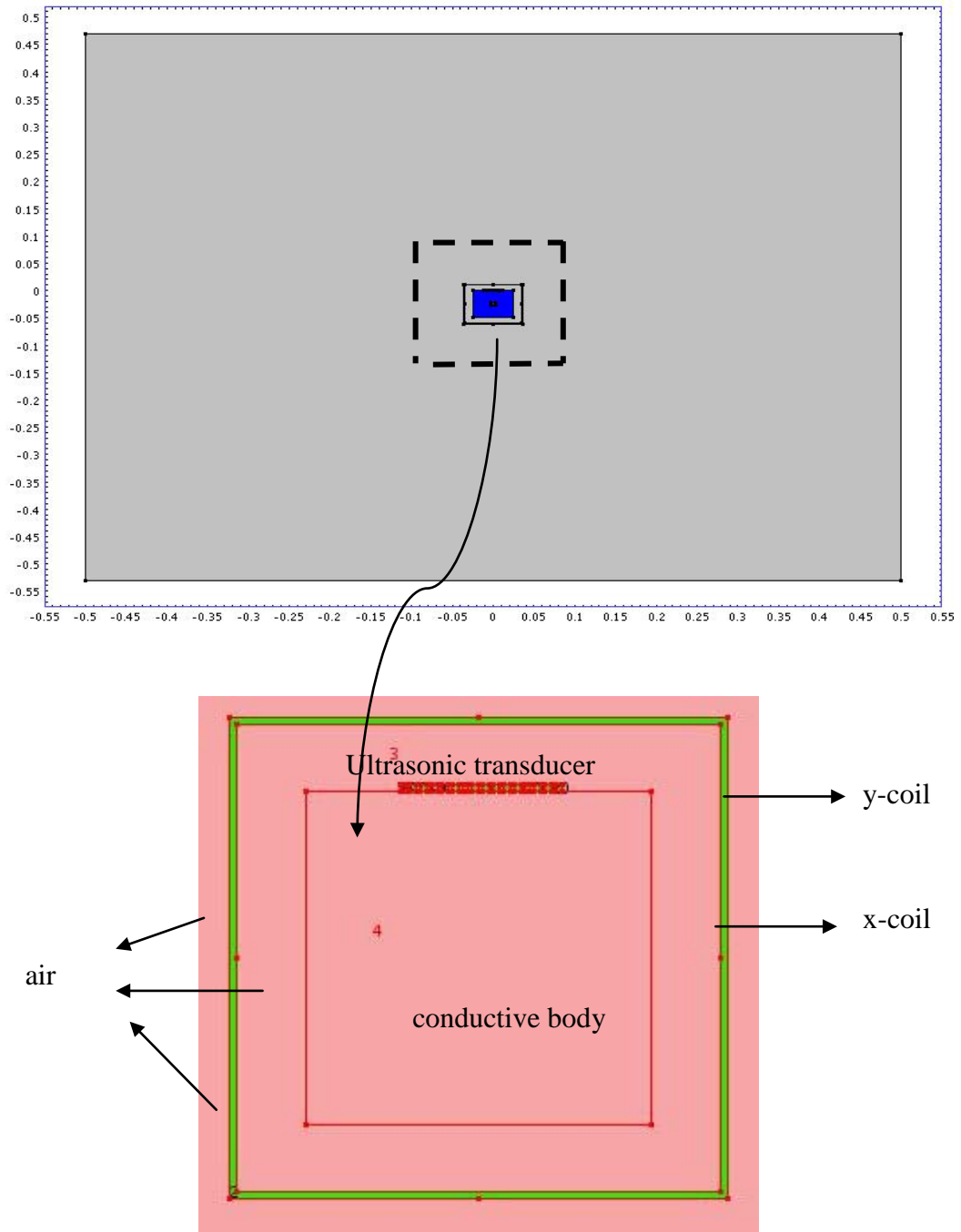
Figure 3-7 Geometry of problem solved with FEM. The surrounding air is 1m x1m in size. In the above figure the conductive body, transducers and receiver coils are not clear. In the below figure it is clear that the transducers are positioned at the upper boundary the conductive body and the receiver coils are encircle the conductive body.
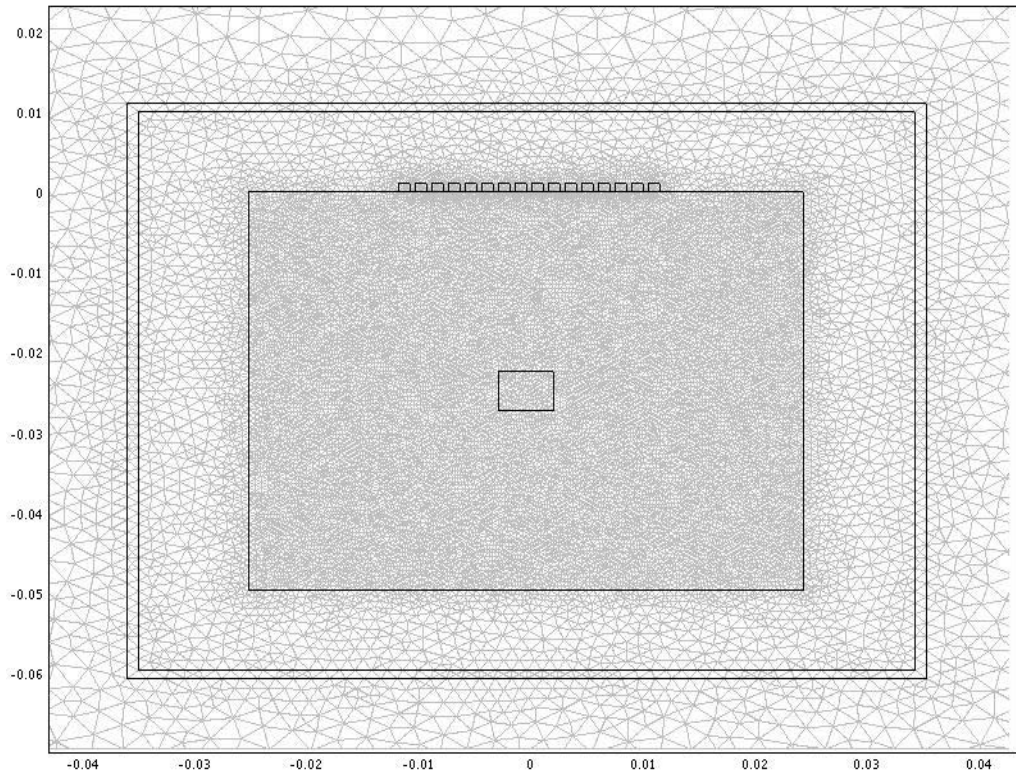
Figure 3-8 Mesh view of the geometry.

CHAPTER 4

RESULTS

4.1 Introduction

For an arbitrary body geometry and conductivity distribution, Lorentz fields cannot be obtained using analytical methods. To obtain a solution, numerical methods must be employed. In this study, numerical solutions are obtained using the Finite Element Method (FEM). In this chapter, results obtained for various simulation studies are presented. The next two sections investigate the pressure and velocity current density distributions for different ultrasonic transducers and different excitation types. The sensitivity matrix analysis for a homogeneous body configuration and reconstructed images are presented in the latter sections.

4.2 Transducer Excitation

In this study, a sinusoidal voltage V is applied to the surface of a piezoelectric crystal for one period of the excitation frequency f, i.e.,

$$V(t) = \mathrm{Asin}(2\pi f t) \qquad (t < 1/f) \qquad (4.1)$$

where the amplitude term A =1V. The corresponding voltage waveform is given in .

The depth of the conductive body is assumed 5 cm. Since the speed of sound in the body is 1520 m/s, to obtain information about the body data should be taken in duration calculated as:

$$x = vt \rightarrow t = \frac{x}{v} = \frac{5cm}{1520m/s} \cong 32.8\ \mu s$$

In this study, the run-time for each simulation is chosen as 32.8 µs with 0.1µs intervals.
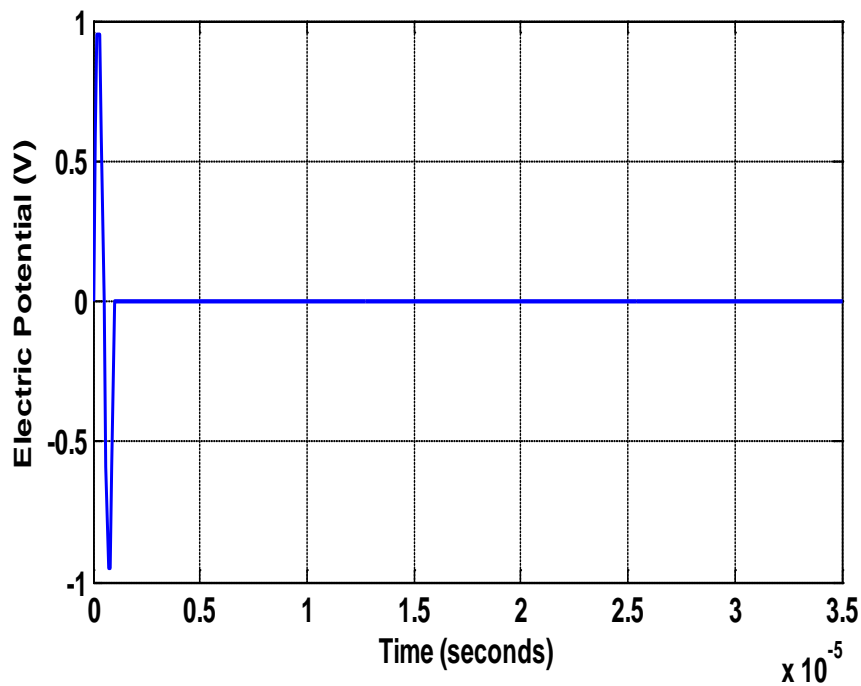
Figure 4-1 Applied voltage (V) to each piezoelectric crystal. The amplitude of the electrical signal is selected as 1 V as given in y-axis. The x-axis shows time in seconds.

4.3 Transducer Types (Single Element, Linear Phased Array)

Two different types of ultrasonic transducers are used in the simulations: single element transducer and linear phased array transducer with 16-elements (crystals).

The geometry of piezoelectric crystal changes with the resonance frequency of the transducer. The relation between the thickness and resonance frequency of the piezoelectric element is given with the following equation:

$$f_R = \frac{c}{2t} \tag{4.2}$$

where f_R is the resonance frequency, c is the speed of sound in the crystal, and t is the thickness of the crystal. Note that the resonance frequency increases as the crystal thickness decreases. In this study, the resonance frequency of piezoelectric element is considered as 1MHz. The sound speed of PZT-5H is 4000 m/s, therefore the thickness of piezoelectric is chosen as 1 mm.

4.3.1 Single Element

The two-dimensional model of a single element transducer has 1 mm thickness and 1 cm length (Figure 4-2). When the transducer is excited with a pulse waveform (as shown in Figure 4-1) a pressure wave propagates inside the body. The pressure distributions at different time instants inside a homogenous and inhomogeneous body are shown in Figure 4-3 through Figure 4-5 and, Figure 4-12 through Figure 4-14 respectively. The corresponding velocity current density distributions are given in Figure 4-9 through Figure 4-11 and Figure 4-18 through Figure 4-20, respectively. Note that the maxi mum velocity current density induced in the body is approximately 0.2 mA/m^2, which is below the safety limit at 1MHz. The pressure waves in a homogeneous body at different points along the main propagation axis are shown in Figure 4-4.
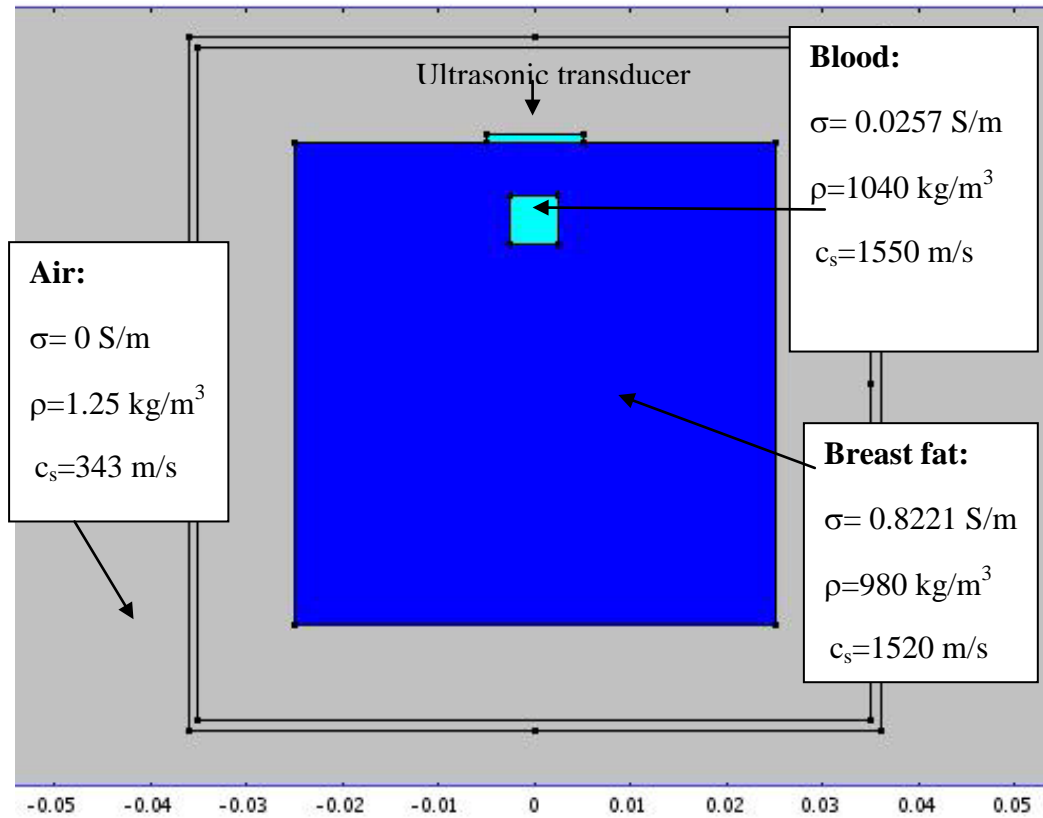
Figure 4-2 Electrically and acoustically inhomogeneous body. A single element transducer and two receiver coils are also shown. The inhomogeneous body models blood in a homogeneous breast tissue.

Note that, as the pressure wave moves away from the transducer, the amplitude of the pressure decreases (Figure 4-6 through Figure 4-8). The peak pressure values at 1cm, 2.5 cm and 4.5 cm below the transducer are approximately 8100 Pa, 7900 Pa and 4900 Pa, respectively.
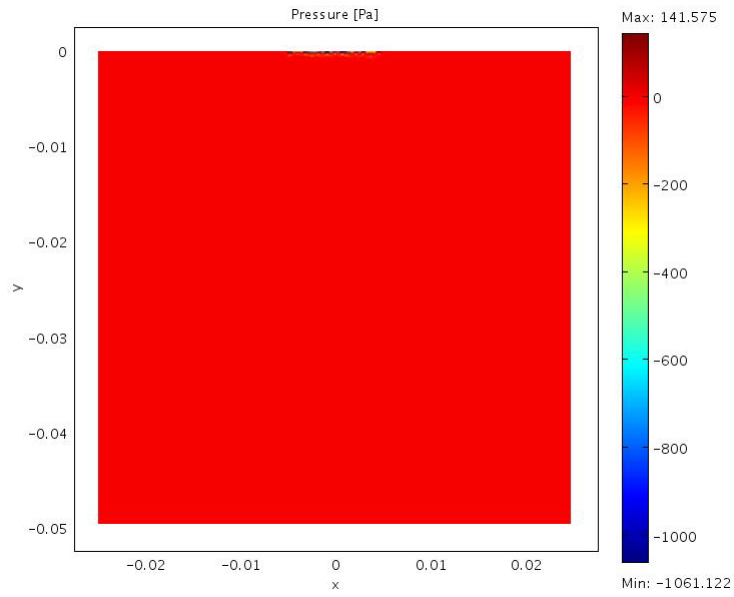
Figure 4-3 Pressure distributions due to single element transducer for   t = 0.1 μ in a homogeneous body
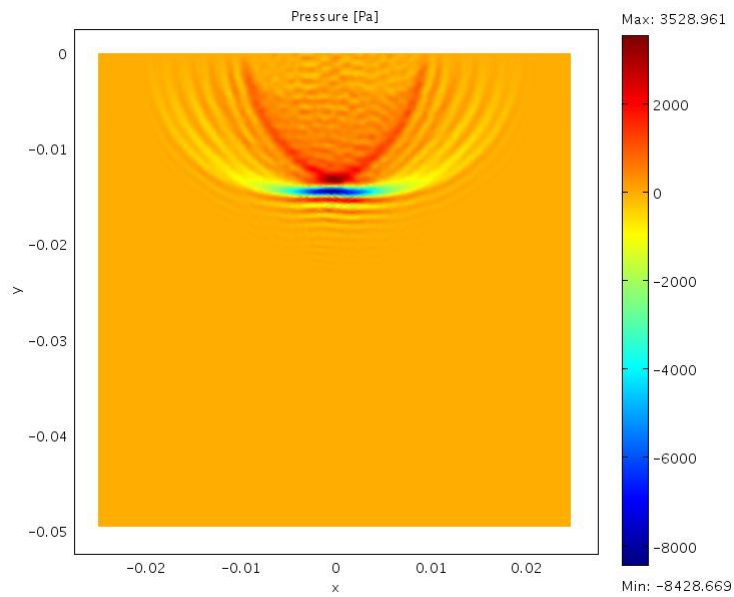
Figure 4-4 Pressure distributions due to single element transducer for t = 10 μs in a homogeneous body

65
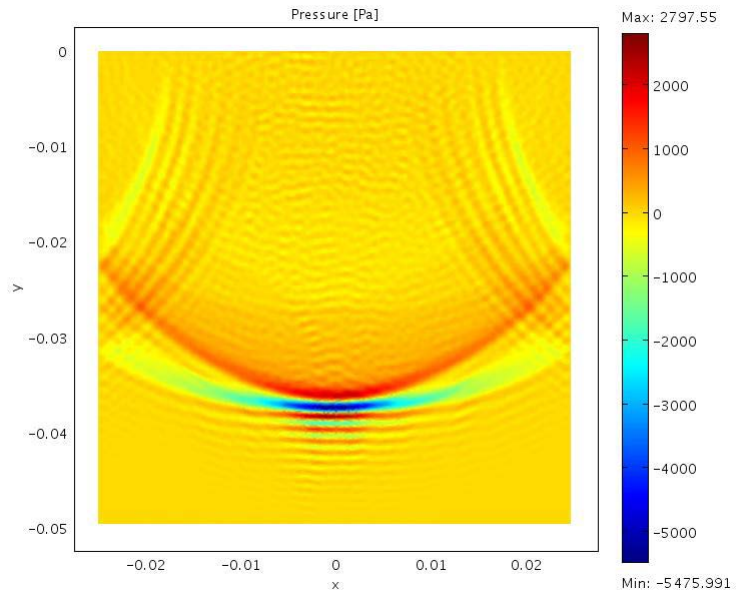
Figure 4-5 Pressure distributions due to single element transducer for t = 25 μs in a homogeneous body
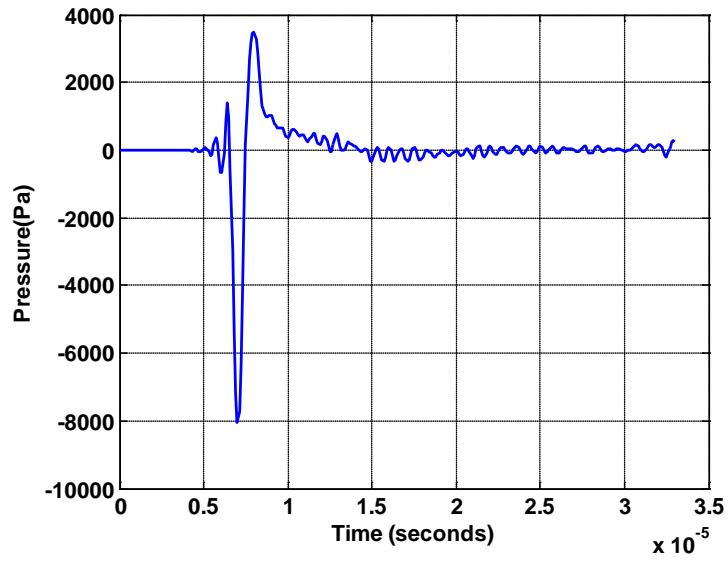
Figure 4-6 Pressure waves in the homogeneous body at 1cm below the transducer along the main axis of the transducer
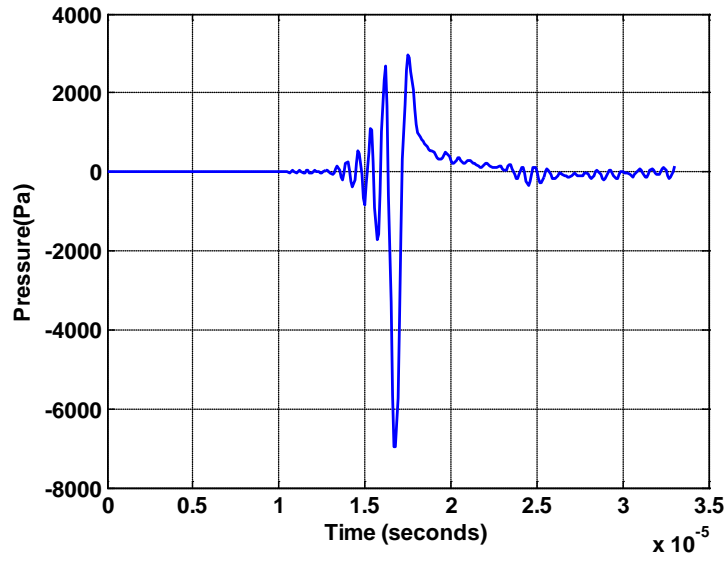
Figure 4-7 Pressure waves in the homogeneous body at 2.5 cm below the transducer along the main axis of the transducer
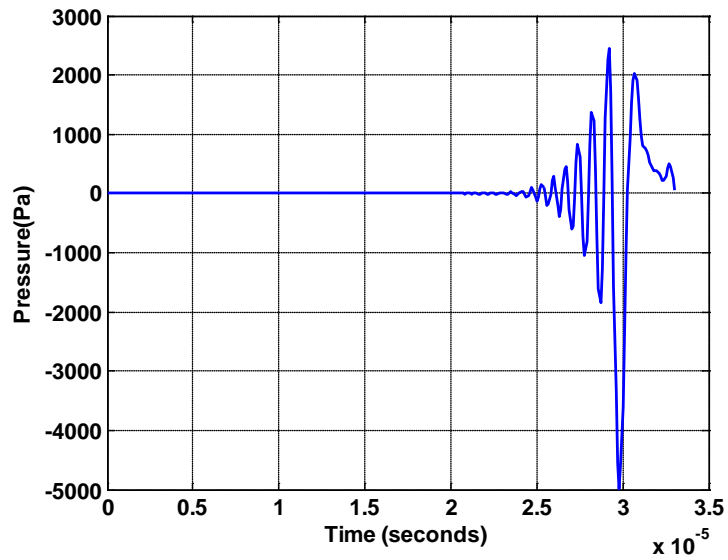
Figure 4-8 Pressure waves in the homogeneous body at 4.5 cm below the transducer along the main axis of the transducer
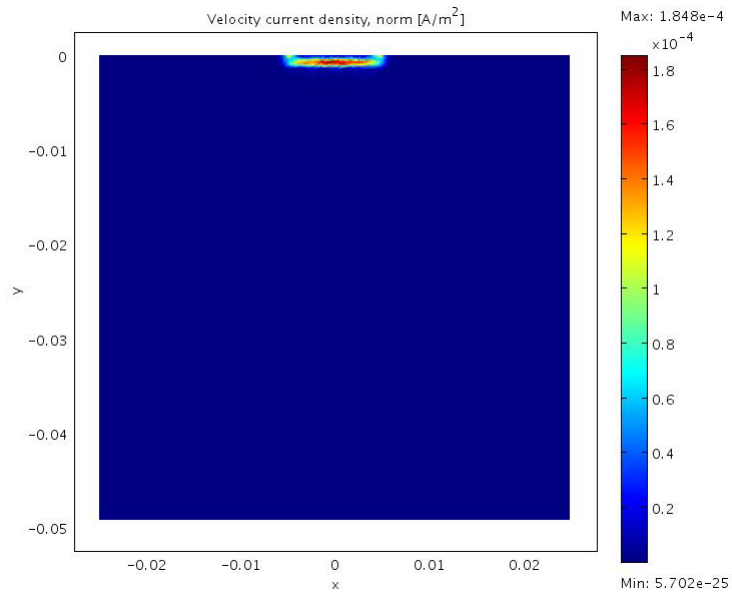
Figure 4-9 Velocity current density distributions for t = 1 μs in the homogeneous body
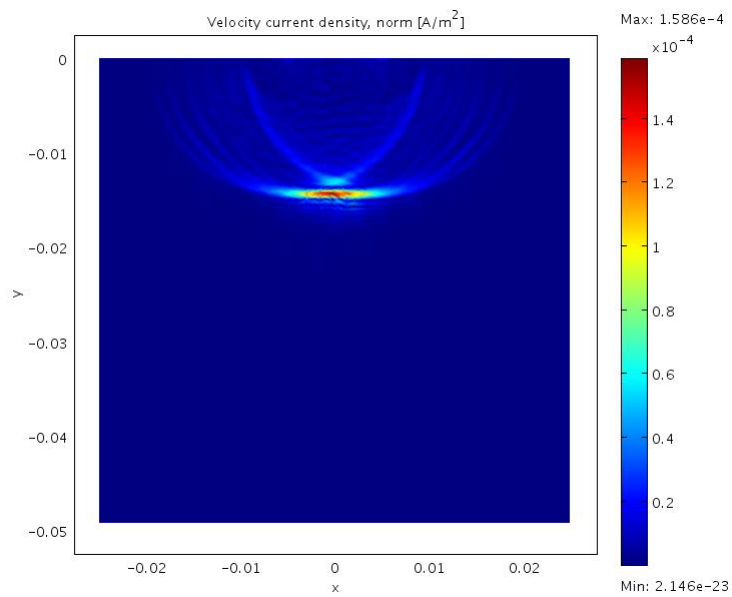
Figure 4-10 Velocity current density distributions for t = 10 μs in the homogeneous body

68
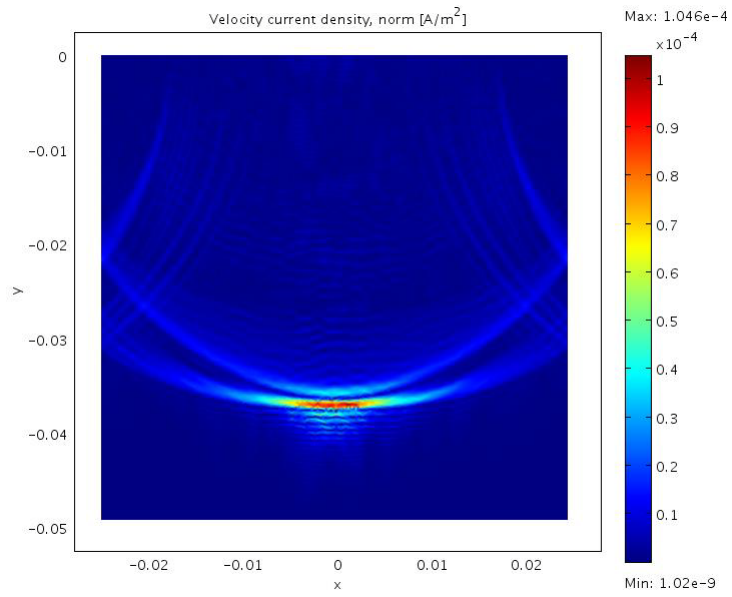
Figure 4-11 Velocity current density distributions for t = 25 µs in the homogeneous
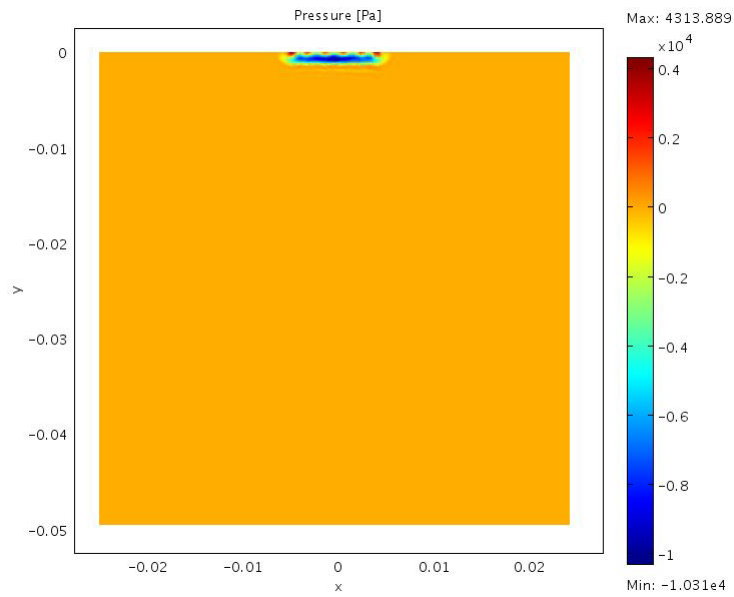
Figure 4-12 Pressure distributions generated with single element transducer for t = 0.1 µs in inhomogeneous body (with blood)
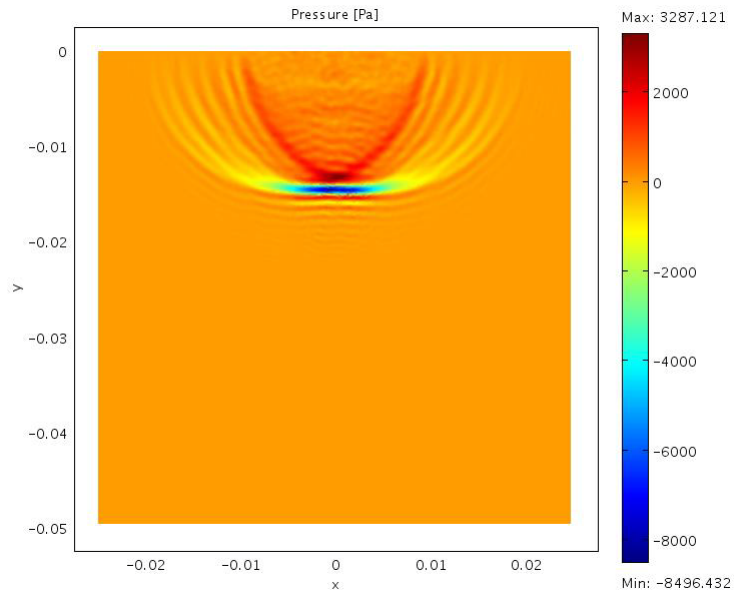
Figure 4-13 Pressure distributions generated with single element transducer for t = 10 μs in inhomogeneous body (with blood)
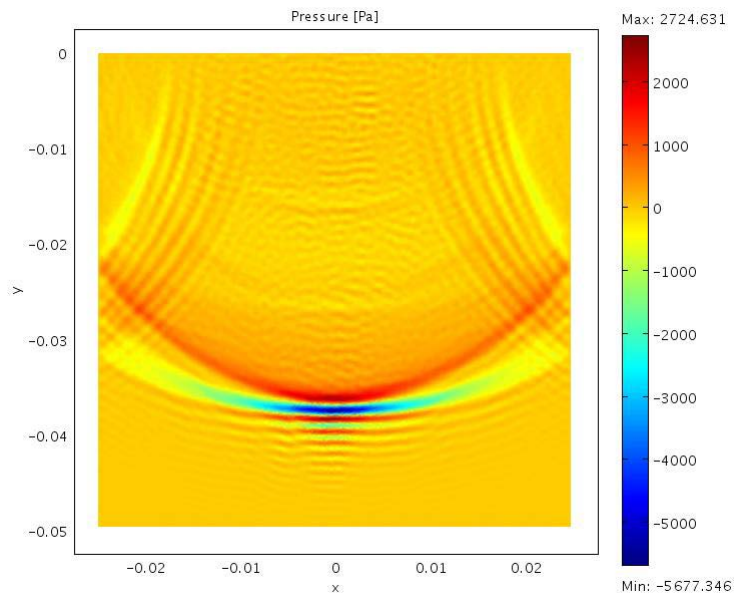
Figure 4-14 Pressure distributions generated with single element transducer for t = 25 μs in inhomogeneous body (with blood)
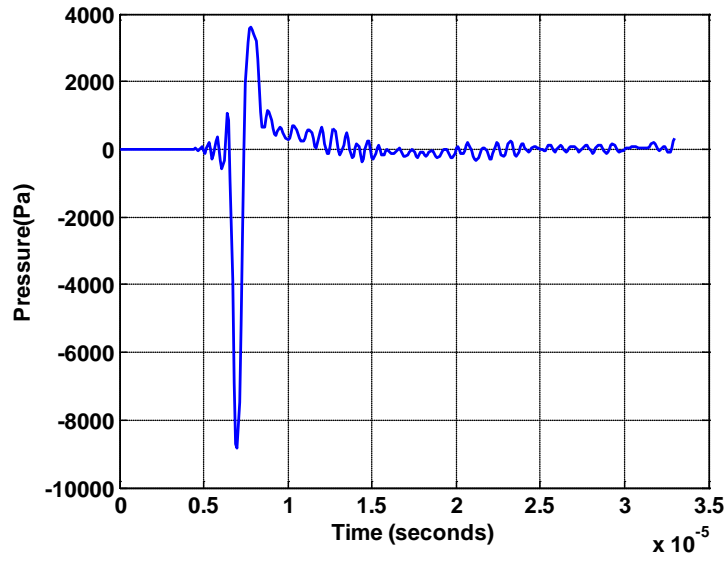
Figure 4-15 Pressure waves in the inhomogeneous body at 1cm below the transducer along the main axis of the transducer
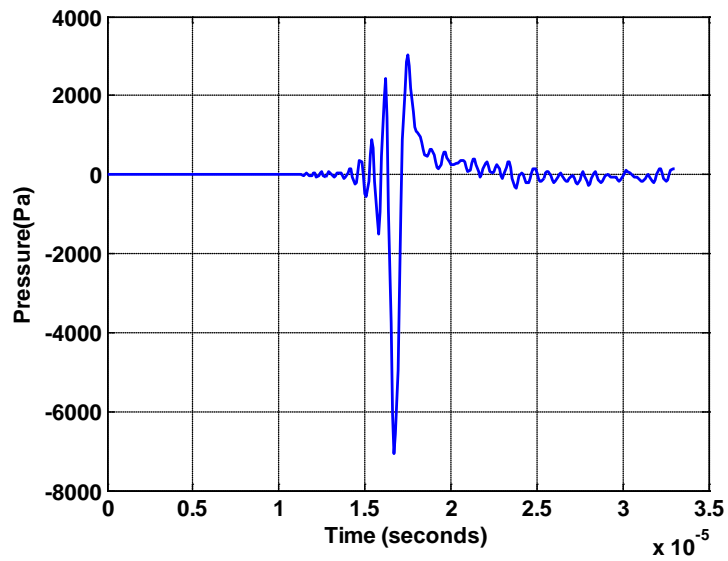
Figure 4-16 Pressure waves in the inhomogeneous body at 2.5 cm below the transducer along the main axis of the transducer
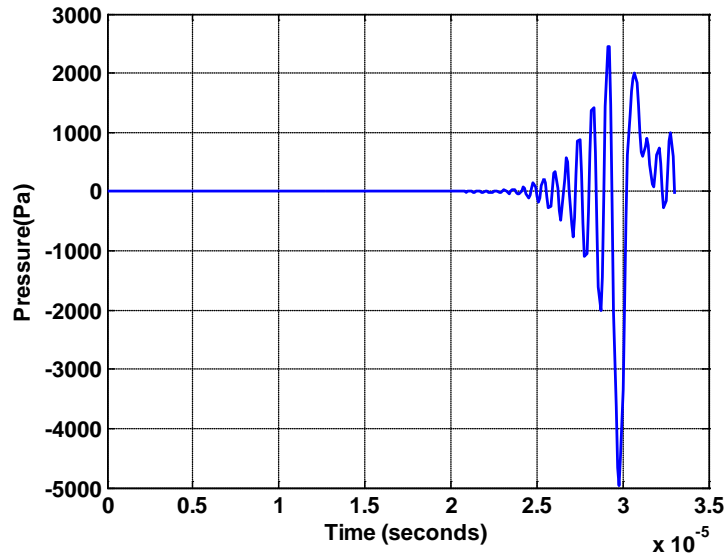
Figure 4-17 Pressure waves in the inhomogeneous body at 4.5 cm below the transducer along the main axis of the transducer

Figure 4-15 through Figure 4-17 show the pressure distributions in inhomogeneous body at 1 cm, 2.5 cm and 4.5 cm below the single element transducer. As the pressure wave moves away from the transducer, the amplitude of the pressure wave decreases. The peak pressure values at 1 cm, 2.5 cm and 4.5 cm below the transducer are calculated as 8200 Pa, 7700 Pa and 5000 Pa, respectively.

In the inhomogeneous body (4 mm x 5 mm blood, 8 mm below the transducer), the electrical conductivity of blood is higher compared to the breast fat ($\sigma_{blood} = 0.8221$ S/m, $\sigma_{breast\ fat} = 0.0257$ S/m at 1MHz). Consequently, the induced current density in the blood must be higher than the rest of the body (Figure 4-18 through Figure 4-20). Note that the velocity current density induced in this domain must be under the safety limit (Maximum induced current is about 5 mA/m^2). In the homogeneous domain maximum current is approximately 0.2 mA/m^2.
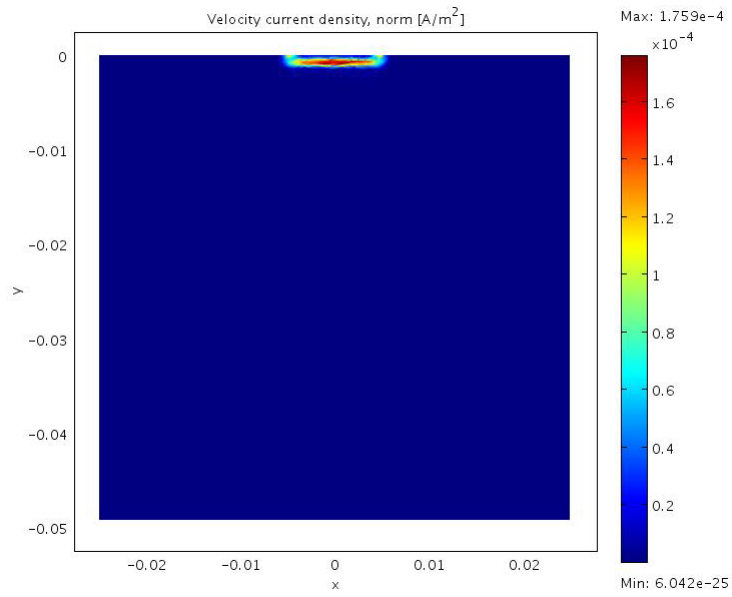
Figure 4-18 Velocity current density distributions for t= 0.1 µs in the inhomogeneous body
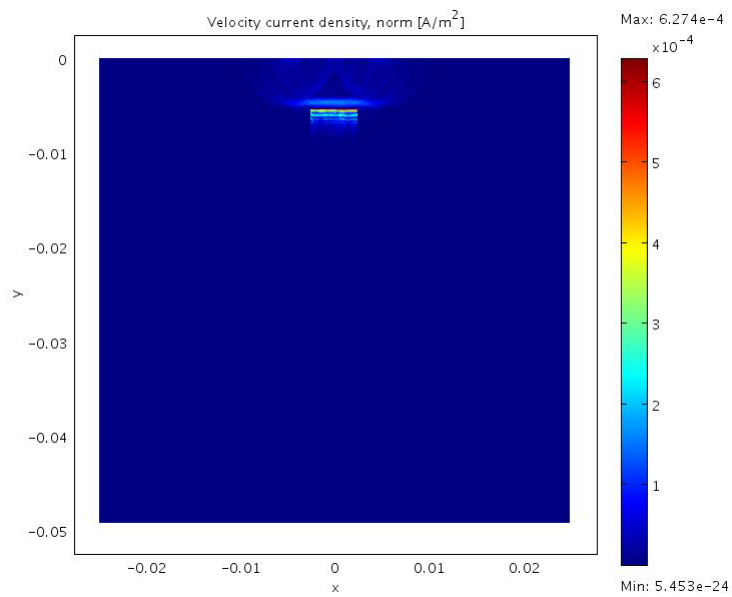
Figure 4-19 Velocity current density distributions for t= 3.6 µs in the inhomogeneous body
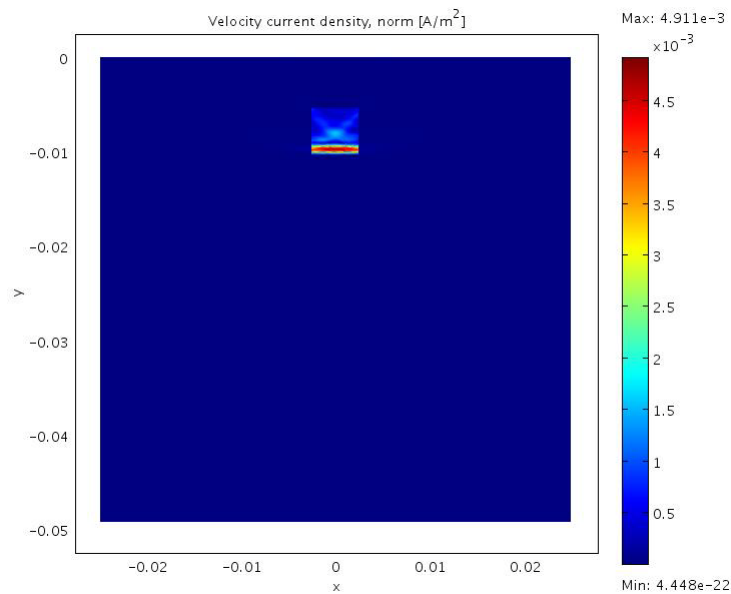
Figure 4-20 Velocity current density distributions for t= 6.9 μs in the inhomogeneous body

4.3.2 Linear Phased Array

For the linear phased array transducer, the number of piezoelectric crystals is 16 (Figure 4-21). Each element of the transducer is modeled with 1 mm thickness, and is excited with the same electrical potential (as given in Equation (4.1)). For the homogeneous body, the pressure distributions and pressure waves at selected positions are shown in Figure 4-22 through Figure 4-24 and Figure 4-25 through Figure 4-27, respectively. Figure 4-28 through Figure 4-30 show the velocity current density distributions corresponding to the pressure distributions (as given in Figure 4-22 through Figure 4-24). The same plots are also prepared for the inhomogeneous body. Figure 4-31 through Figure 4-33 and Figure 4-37 through Figure 4-39 show the pressure and velocity current distributions when there is an inhomogeneity as displayed in Figure 4-21. Figure 4-34 through Figure 4-36 present the pressure waves at the selected locations on the main propagation axis.

74

For both cases (homogeneous and inhomogeneous) as the pressure wave moves away from the transducer, the amplitude of the pressure decreases. The peak pressure values at 1 cm, 2.5 cm and 4.5 cm are calculated as 3000 Pa, 2700 Pa and 2400 Pa for the homogeneous body, respectively. For the inhomogeneous body, the peak pressure values at the same positions are calculated as 3100 Pa, 2600 Pa and 2400 Pa, respectively.

The velocity current density distributions show that the induced current in the blood is under the safety limit (Maximum induced current density is about 2 mA/m^2). In the homogeneous body, however, maximum current density is even less, i.e., it is approximately 0.1 mA/m^2.
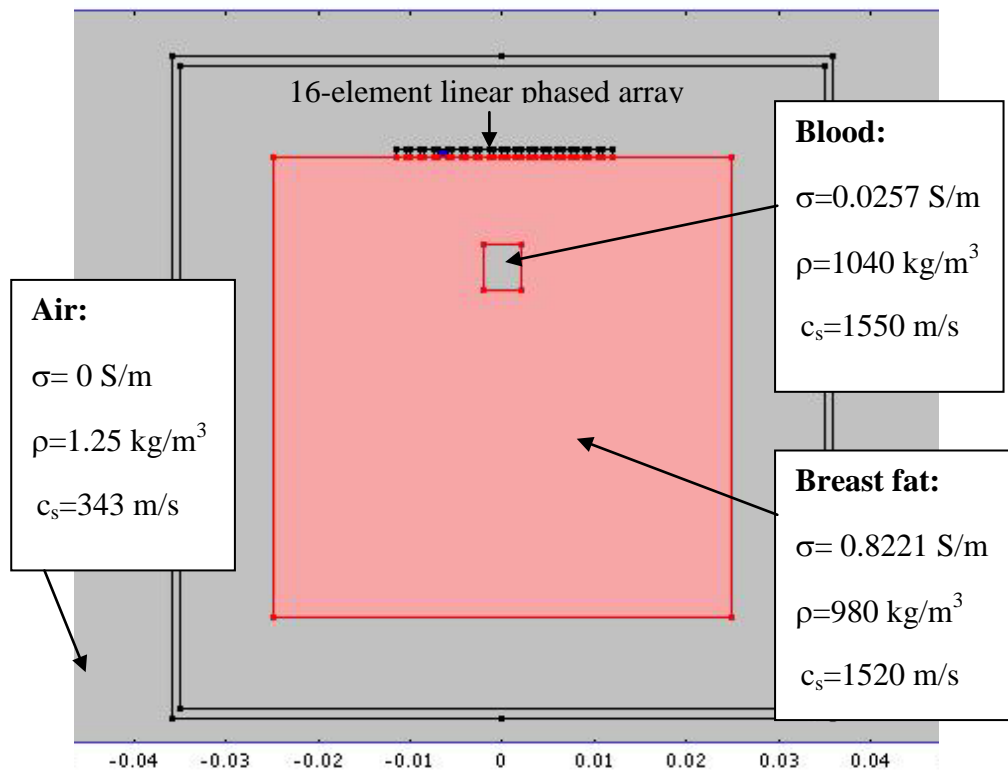
Figure 4-21 Electrically and acoustically inhomogeneous body. A 16-element linear phased array transducer and two receiver coils are also shown. The inhomogeneous body models blood in a homogeneous breast tissue.
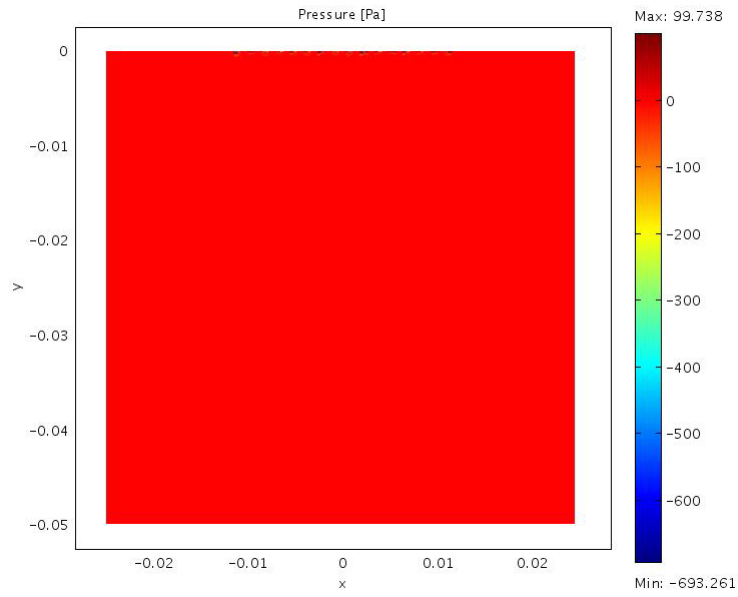
Figure 4-22 Pressure distributions due to 16-element linear phased array transducer for t = 0.1 μs in a homogeneous body
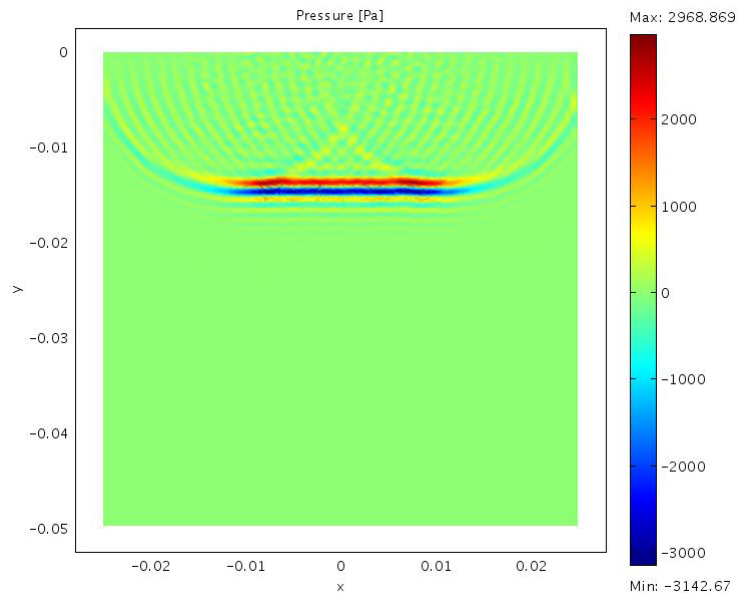
Figure 4-23 Pressure distributions due to 16-element linear phased array transducer for t = 10 μs in a homogeneous body

76
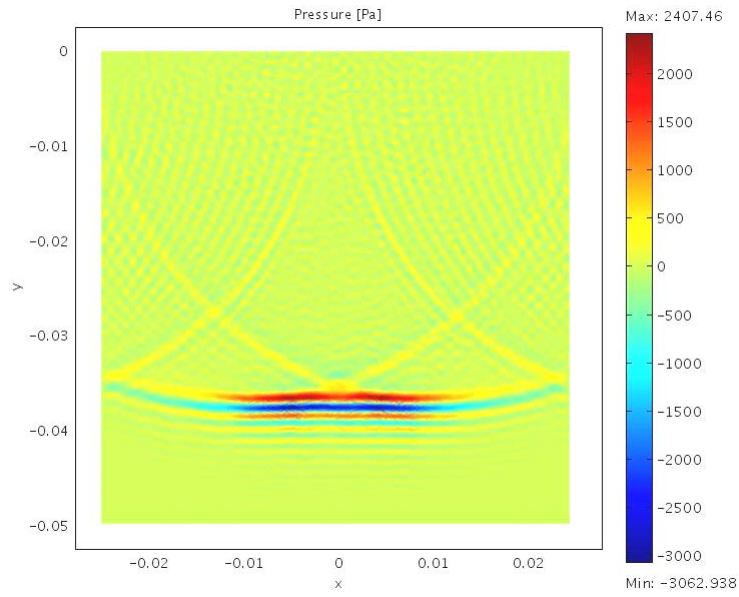
Figure 4-24 Pressure distributions due to 16-element linear phased array transducer for t = 25 μs in a homogeneous body
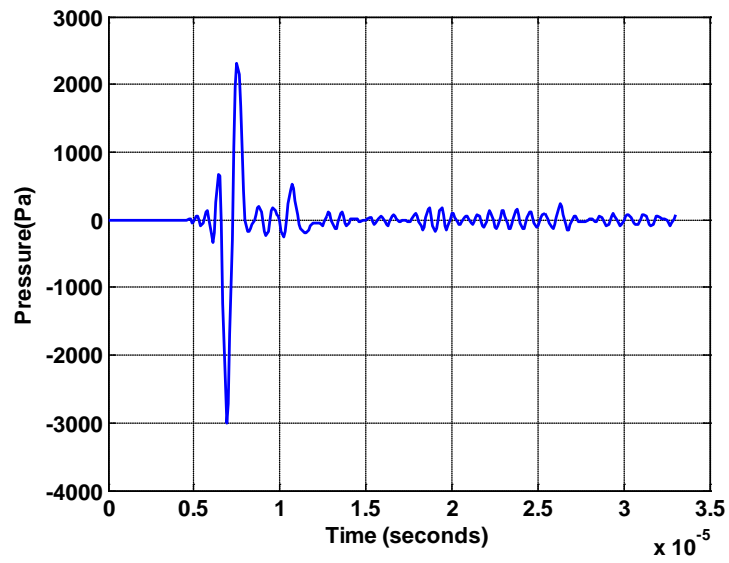
Figure 4-25 Pressure waves in the homogeneous body at 1 cm below the transducer along the main axis of the transducer (16-element linear phased array)
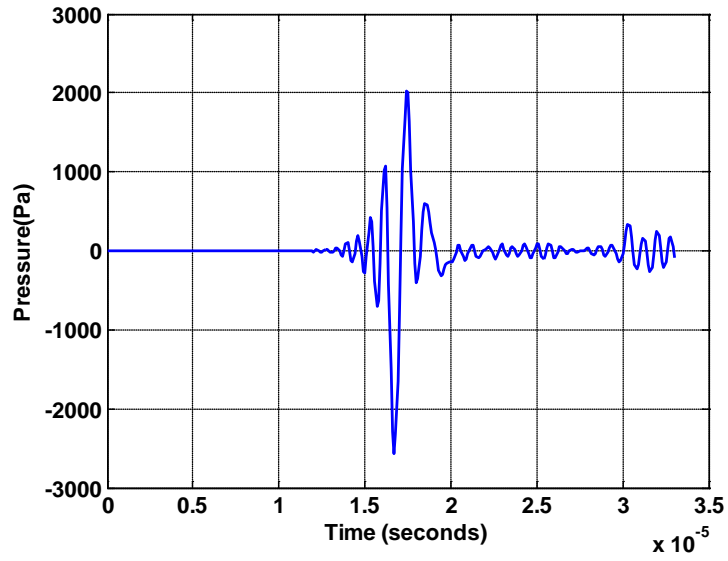
Figure 4-26 Pressure waves in the homogeneous body at 2.5 cm below the transducer along the main axis of the transducer (16-element linear phased array)
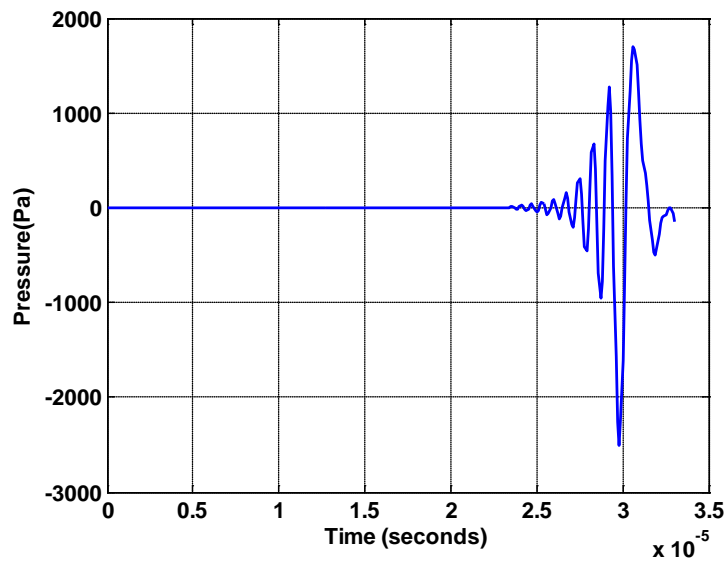
Figure 4-27 Pressure waves in the homogeneous body at 4.5 cm below the transducer along the main axis of the transducer (16-element linear phased array)
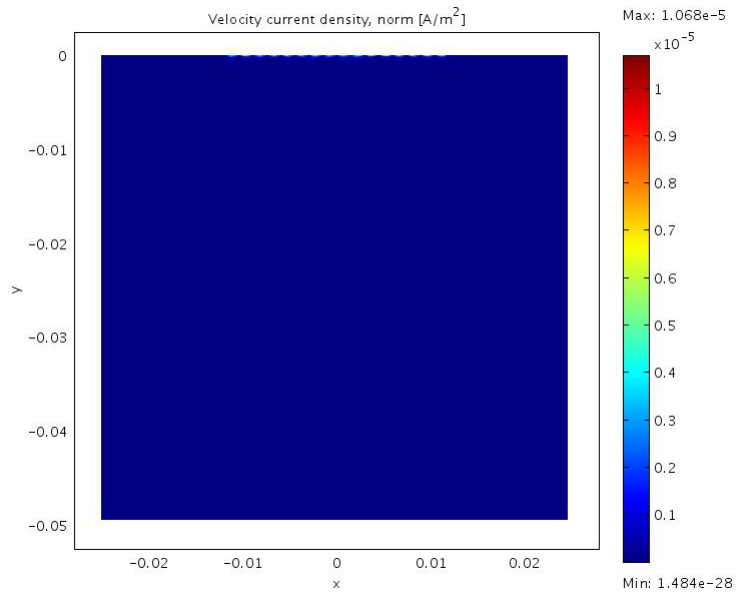
Figure 4-28 Velocity current density distributions for t = 0.1 μs in the homogeneous body (16-element linear phased array transducer)
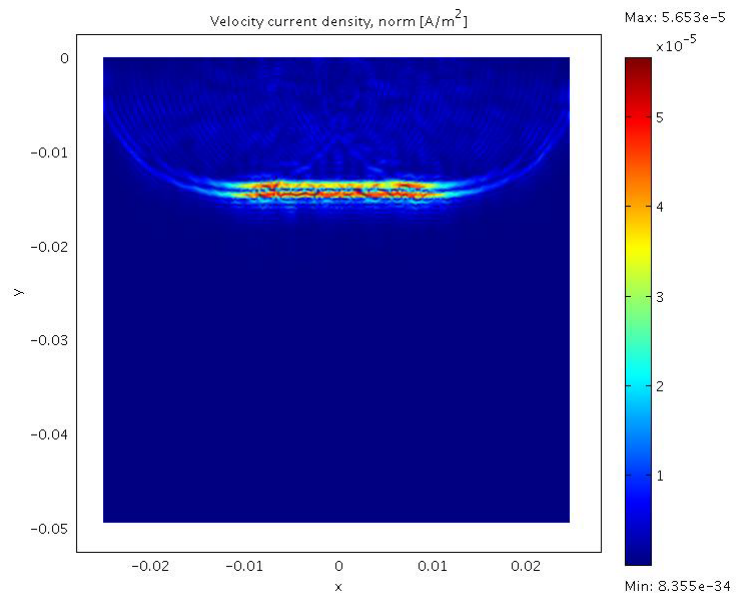
Figure 4-29 Velocity current density distributions for t =10 μs in the homogeneous body (16-element linear phased array transducer)
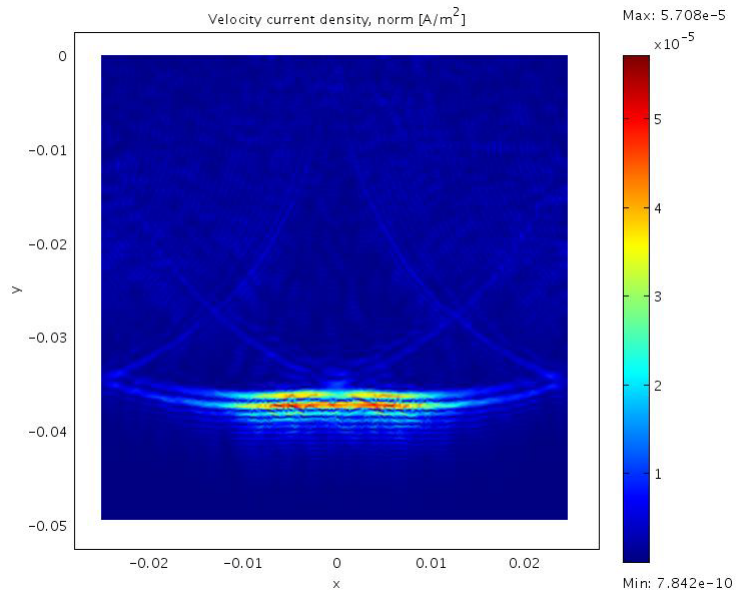
Figure 4-30 Velocity current density distributions for t =25 µs in the homogeneous body (16-element linear phased array transducer)
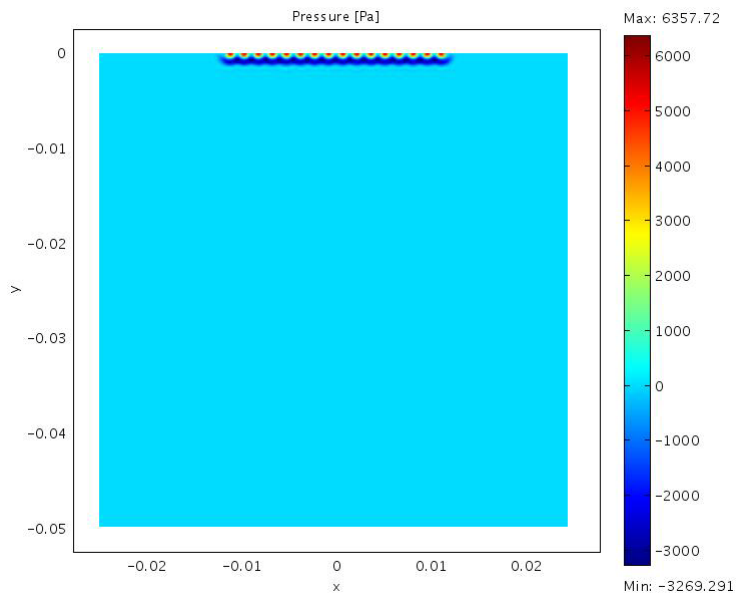
Figure 4-31Pressure distributions due to 16-element linear phased array transducer for t = 0.1 µs in the inhomogeneous body
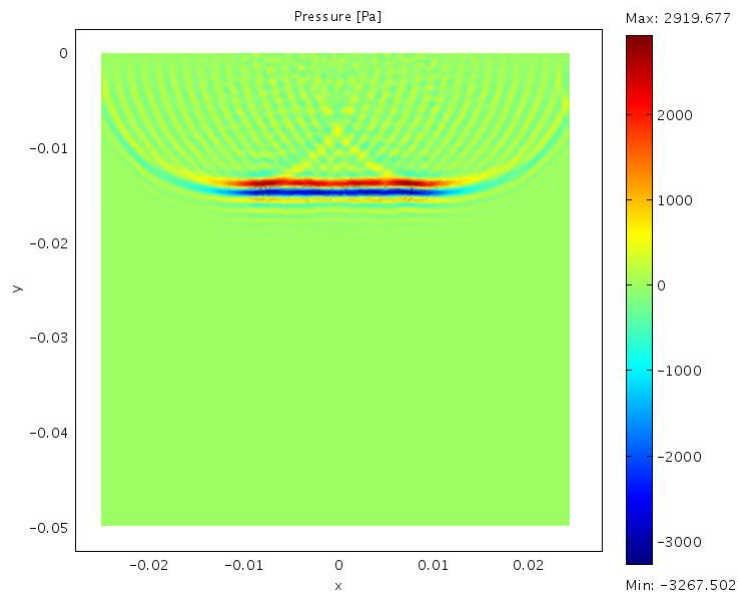
Figure 4-32 Pressure distributions due to 16-element linear phased array transducer for t = 10 μs in the inhomogeneous body
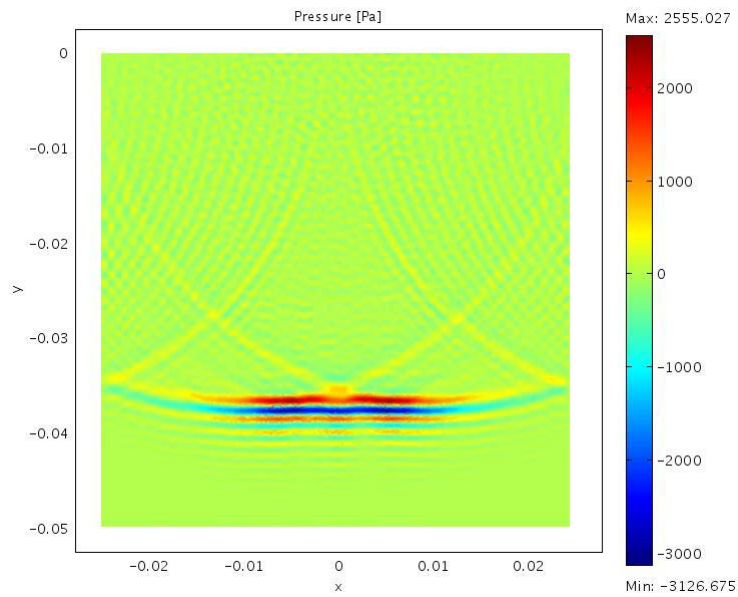
Figure 4-33 Pressure distributions due to 16-element linear phased array transducer for t = 25 μs in the inhomogeneous body
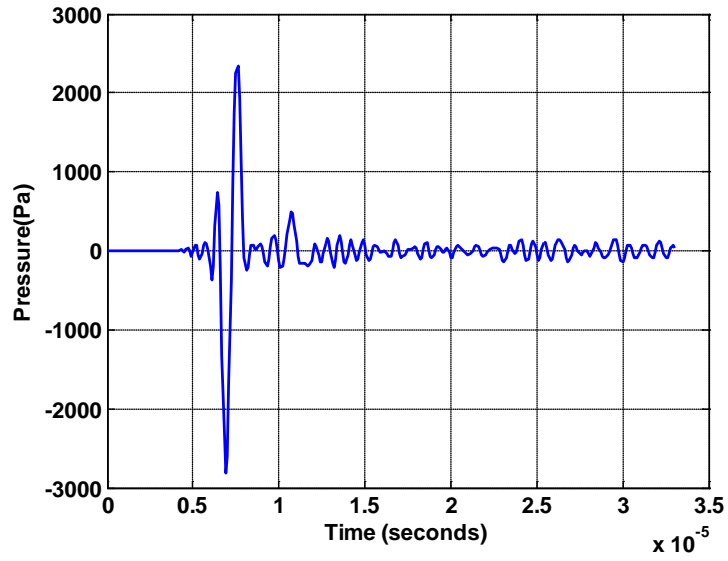
Figure 4-34 Pressure waves in the inhomogeneous body at 1cm below the transducer along the main axis of the transducer (16-element linear phased array)
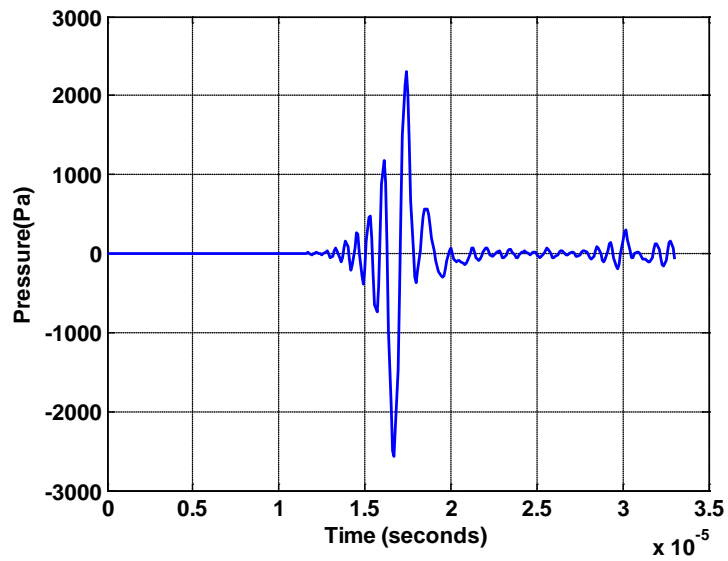
Figure 4-35 Pressure waves in the inhomogeneous body at 2.5 cm below the transducer along the main axis of the transducer (16-element linear phased array)
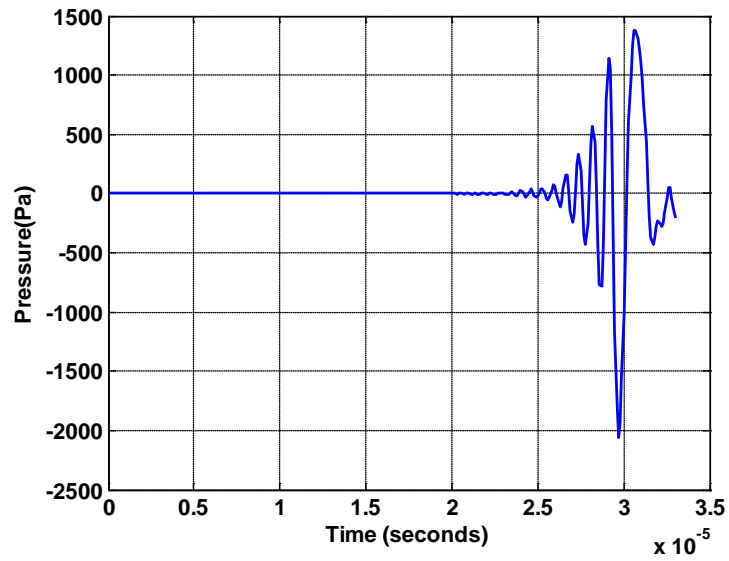
Figure 4-36 Pressure waves in the inhomogeneous body at 4.5 cm below the transducer along the main axis of the transducer (16-element linear phased array)
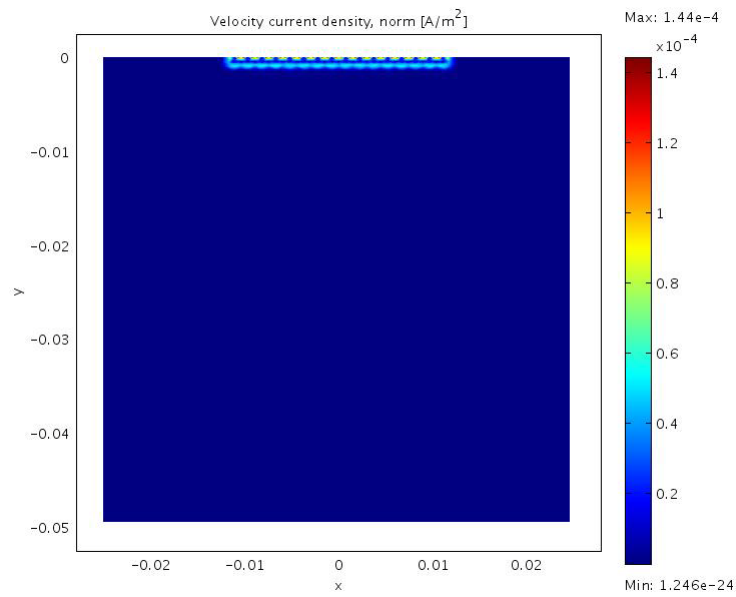
Figure 4-37 Velocity current density distributions for t = 0.1 μs in the inhomogeneous body
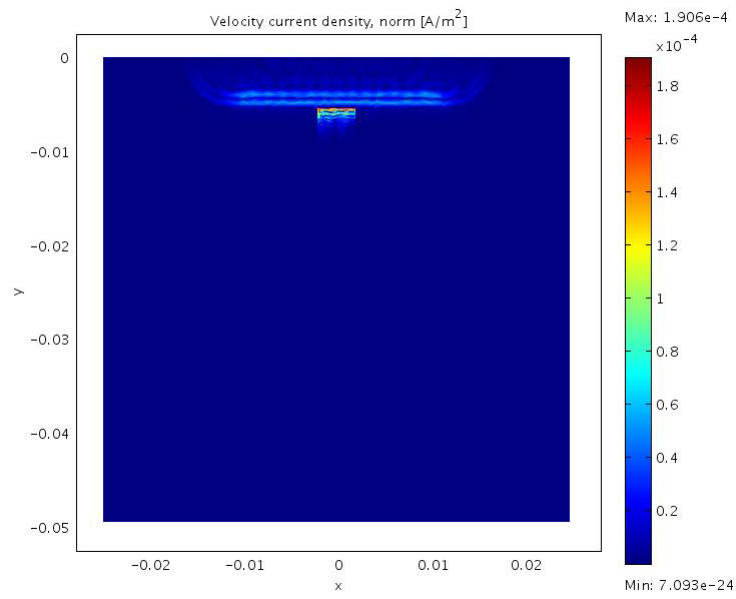
Figure 4-38 Velocity current density distributions for t = 3.6 μs in the inhomogeneous body
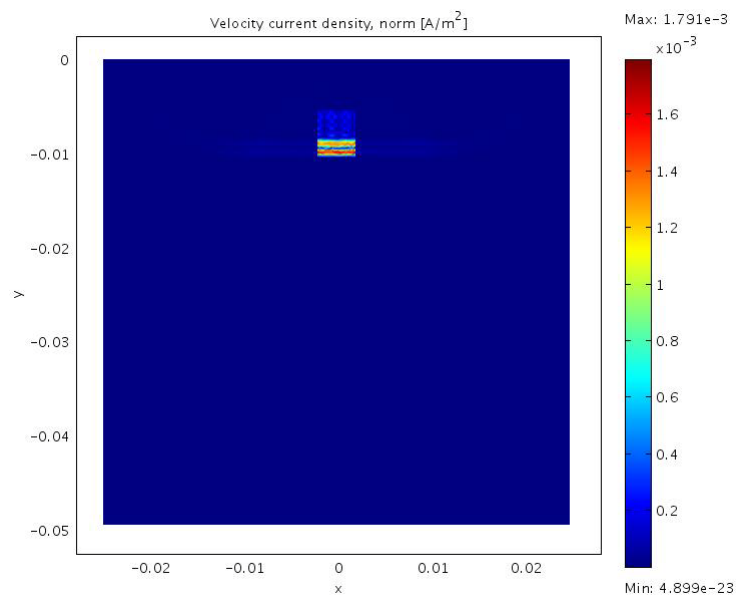
Figure 4-39 Velocity current density distributions for t = 6.9 μs in the inhomogeneous body

4.4 Measurement of Induced Voltage along Receiver Coils

In order to measure the velocity current density induced in the conductive body and tumor tissue, we use two receiver coils, namely, x-coil and y-coil. Detailed information about the receiver coils is given in Chapter 3 Coil Configuration part. These coils are encircling the conductive body. The induced voltages in the receiver coils can be calculated using the following line integral:

$$V_{ind} = - \int \vec{E}_{ind} \cdot d\vec{l} \tag{4.3}$$

where $\vec{E}_{ind}$ represents the electric field along the receiver coil geometry and $d\vec{l}$ denotes the differential element on the coil path. Note that, a different approach is presented in Chapter 2 that expresses the measurements in terms of the lead-fields. To verify the lead field formulation, the receiver voltages are calculated using the two approaches: 1) using the lead field equation (Equation (2.101)) and 2) using the line integral equation (Equation 4.3). For this comparison 16-element linear phased array transducer is placed on the upper edge of the body. The steering angle is chosen as zero degree.

Figure 4-40 shows the normalized voltage waveforms for the homogeneous body. Figure 4-41 shows the normalized receiver voltages for the inhomogeneous body. For both cases, the voltage waveforms obtained by the lead-field approach closely follow the waveforms obtained by the line integral expression. Consequently, one may conclude that the lead field approach correctly models the forward problem of the proposed approach. The lead field formulation will be the basis of the inverse problem studies presented in the latter sections.

Normalized Induced Voltage along the x-coil

a)

Normalized Induced Voltage Calculated with Lead Fields
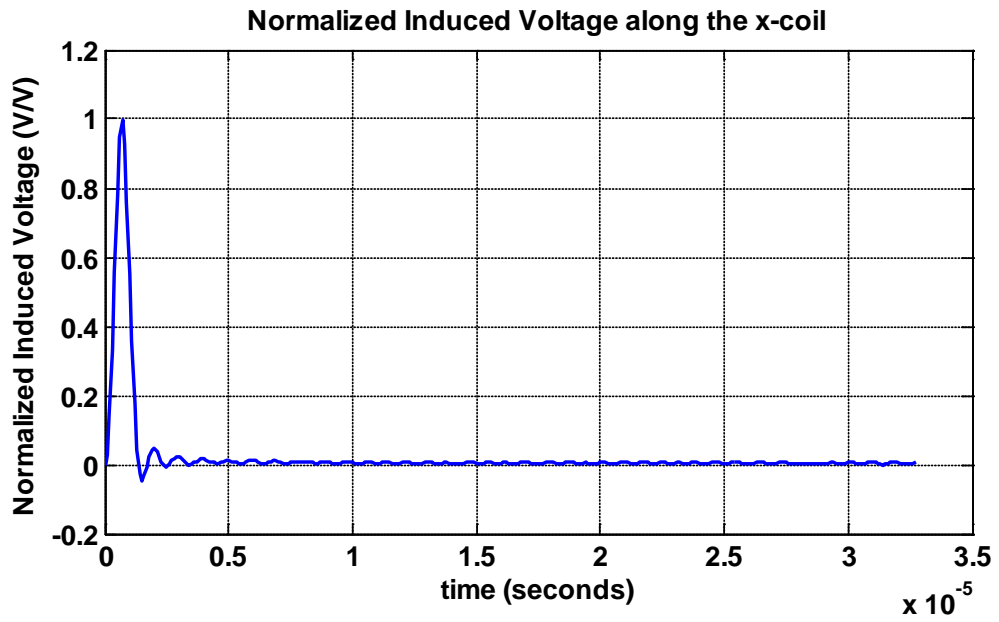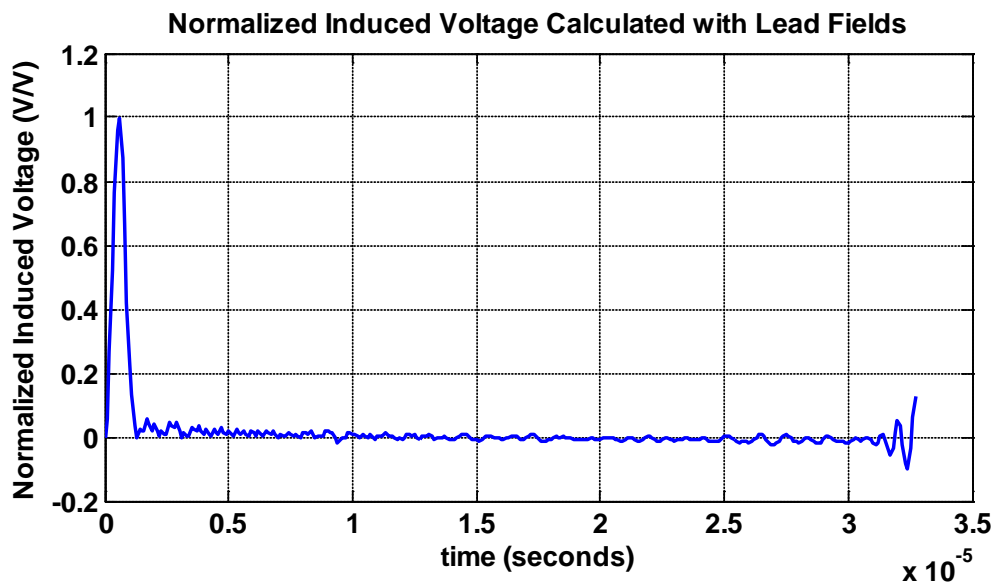
b)

Figure 4-40 Induced voltage along x-coil for homogeneous conductive body with 16-element linear phased array transducer   a) using Equation (4.3)   b) using the lead field equation (Equation (2.101))

Normalized Induced Voltage along the x-coil

a)

Normalized Induced Voltage Calculated with Lead Fields
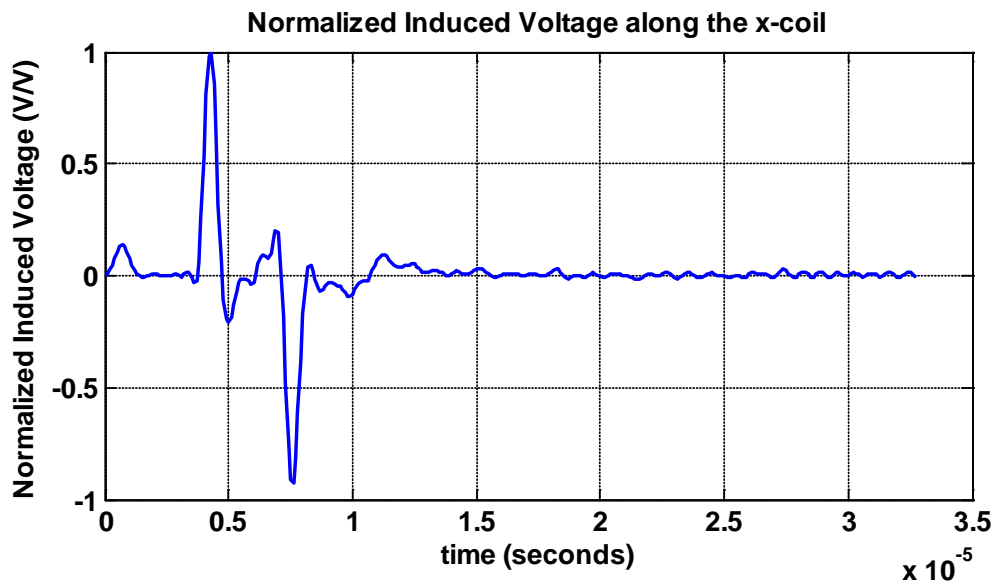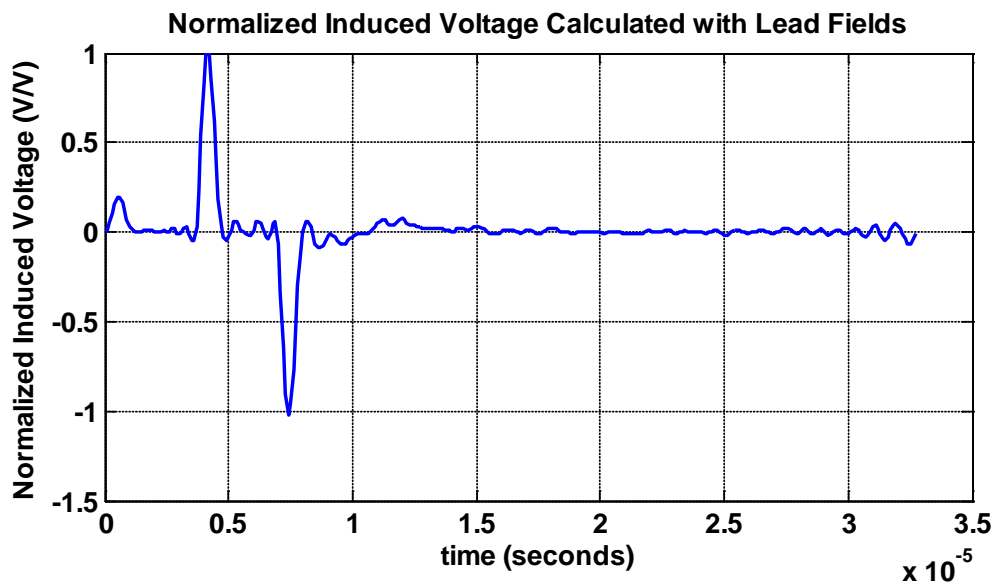
b)

Figure 4-41 Induced voltage along x-coil for inhomogeneous conductive body (blood is placed 8 mm below the transducer, with 5 mm x 5mm geometry) with 16-element linear phased array a) using Equation (4.3)   b) using the lead fields (Equation (2.101))

4.5 Inverse Problem Solution

The aim of this imaging modality is to reconstruct the electrical impedance distribution $\kappa = \sigma + j\omega\varepsilon$ (or its change $\Delta\kappa$ relative to a known distribution). With the proposed approach this can be achieved in two ways:

1) **Time-Harmonic excitation:** In this way, the ultrasonic transducer is excited sinusoidally at its resonance frequency and a steady-state current distribution is developed inside the body. The magnetic fields of the induced current can be measured by detector coils placed nearby the body or by encircling coils. The number of measurements can be increased by changing the transducer position. Ww   The relation between the pick-up voltages and conductivity distribution in the body is already derived and given by equation (2.105):

$$V(\sigma) = \int_{V_{body}} \frac{\partial}{\partial t} \sigma\left(\vec{v} \times \vec{B_0}\right) \cdot \vec{L_M}(\sigma) dV \qquad (4.4)$$

where $\vec{L_M}$ (the lead field vector) is the electric field in the reciprocal problem when unit current is applied to the receiver coil.

The relation between the measurement and conductivity is a non-linear mapping. However the first-order variation in the measurement related to conductivity perturbation can be determined. The measurement for a known conductivity distribution σ_0 can be written as

$$\mathbf{V}(\sigma_0) = \int_{V_{body}} \frac{\partial}{\partial t} \sigma_0\left(\vec{v} \times \vec{B_0}\right) \cdot \vec{L_M}(\sigma_0) dV \qquad (4.5)$$

Equation (4.5) can be rewritten when σ is replaced by $\sigma_0 + \Delta\sigma$,

$$V(\sigma_0 + \Delta\sigma) = \int_{V_{body}} \frac{\partial}{\partial t} (\sigma_0 + \Delta\sigma)(\vec{v} \times \vec{B_0}) \cdot \vec{L}_M(\sigma_0 + \Delta\sigma) dV \tag{4.6}$$

When we approximate $\vec{L}_M(\sigma)$ with the lead field of the initial conductivity distribution, i.e., $\vec{L}_M(\sigma) \cong \vec{L}_M(\sigma_0)$, then the following relation is valid,

$$V(\sigma_0 + \Delta\sigma) - V(\sigma_0) = \int_{V_{body}} \Delta\sigma \frac{\partial}{\partial t} (\vec{v} \times \vec{B_0}) \cdot \vec{L}_M(\sigma_0) dV \tag{4.7}$$

A discretized version of Equation (4.7) can be written as

$$\Delta V = \sum_{j=1}^{N} (\vec{E}_{vel} \cdot \vec{L}_M) \Delta\sigma \tag{4.8}$$

where N represents the number of elements in the discrete conductivity model. By changing the coil/transducer configuration it is possible to obtain M independent measurements yielding the following matrix equation relating the change in measurements to a perturbation in conductivity:

$$\Delta \mathbf{V} = \mathbf{S}_{TH} \Delta\boldsymbol{\sigma} \tag{4.9}$$

Here $\mathbf{S}_{TH}$ represents the sensitivity matrix for the time-harmonic excitation. In this study, the performance of imaging using time-harmonic excitation is not studied in detail, though the theory behind is clarified.

2) Pulse type excitation: When the transducer is excited with an electrical pulse, then a pressure wave is generated inside the body. In such a case, the particle velocity is a function of time, i.e., $\vec{v} = \vec{v}(t)$ yielding a velocity current density distribution propagating inside the body. The relation between the pick-up voltage and conductivity distribution will be very similar to the time-harmonic case as shown by equation (2.101). However, the measurement in such a case is time varying:

$$V(\sigma, t) = \int_{V_{body}} \sigma \left(\vec{\boldsymbol{v}}(t) \times \vec{\boldsymbol{B}}_0 \right) \cdot \vec{L}_M(\sigma) dV \tag{4.10}$$

The first order variation in the measurements can now be written in the data acquisition period (T_D) as,

$$V(\sigma_0 + \Delta\sigma, t) - V(\sigma_0, t) = \int_{V_{body}} \Delta\sigma \left(\vec{v}(t) \times \vec{B}_0 \right) \cdot \vec{L}_M(\sigma_0) dV \tag{4.11}$$

The discretized version can be written as:

$$\Delta V(t) = \sum_{j=1}^{N} \left(\vec{E}_{vel}(t) \cdot \vec{L}_M \right) \Delta\sigma \qquad t < T_D \tag{4.12}$$

This relation can be written for M different time instants ($\Delta t = T_D/M$) as follows:

$$\Delta V(i\Delta t) = \sum_{j=1}^{N} \left(\vec{E}_{vel}(i\Delta t) \cdot \vec{L}_M \right) \Delta\sigma \qquad i = 1 \dots M \tag{4.13}$$

Consequently, a matrix equation can be obtained for a specific transducer position and coil configuration:

$$\Delta \mathbf{V} = \boldsymbol{S_P} \, \Delta\boldsymbol{\sigma} \tag{4.14}$$

where $\boldsymbol{S_P}$ represents the $M \times N$ sensitivity matrix for a pulse type excitation.

In this study, a novel receiver coil configuration is proposed which consists of an x-coil and y-coil (Details are given in Chapter 2 and 3). As their name implies each coil is more sensitive to the currents in the corresponding direction. To specify which coil is used for the measurements an appropriate subscript (i.e., x or y) is added to the relevant terms in equation (4.14) and pick-up voltages are written in the following forms:

$$\Delta \mathbf{V_x} = \boldsymbol{S_{Px}} \, \Delta\boldsymbol{\sigma} \tag{4.15}$$

$$\Delta \mathbf{V_y} = \boldsymbol{S_{Py}} \, \Delta\boldsymbol{\sigma} \tag{4.16}$$

or a larger system of equations can be obtained as

$$\begin{bmatrix} \Delta V_x \\ \Delta V_y \end{bmatrix} = \begin{bmatrix} S_{Px} \\ S_{Py} \end{bmatrix} \Delta \sigma \tag{4.17}$$

Equation (4.17) can also be written in the following form:

$$\Delta V_{xy} = S_{Pxy} \, \Delta \sigma \tag{4.18}$$

where S_{pxy} is an $2MxN$ sensitivity matrix and ΔV_{xy} is a $2Mx1$ measurement vector.

Note that Equation (4.17) is written for a specific transducer position. It is always possible to increase the number of measurements by changing the transducer location.

In this thesis study, to obtain the sensitivity matrix two electromagnetic problems are solved. Firstly, electric fields are computed due to the reciprocal currents in the receiver coils. Thereafter, electric fields (Lorentz Electric Fields) are computed due to the excitation of the ultrasonic transducer in the main static magnetic field. The dot product of the electric fields for each pixel gives the corresponding entries in the sensitivity matrix.

To understand the characteristics of the imaging system, the sensitivity matrix must be analyzed. For this purpose, the transducer-body-receiver coil configuration should be specified. In this study, the body is chosen as 5 cm x 5 cm square object and it is divided into 0.5 mm x 0.5 mm elements, yielding 10000 pixels (N =10000). As it is mentioned in Section 4.2 (Transducer Excitation), the run-time for each simulation is 32.8μs with 0.1μs time intervals. Thus, for each simulation the number of measurements (M) is 328. The linear phased array transducer is assumed to be located at two positions, namely, the upper and the right edges of the body. For each transducer position, the sensitivity matrix is calculated for seven steering angles (-22.5°, -15°, -7.5°, 0°, 7.5°, 15°, 22.5°). Thus, the sensitivity matrix **S** is of dimension 9184x10000. Note that the number of measurements (NM) is obtained using the following formula:

91

$$NM = NST \times NTP \times NRC \times NSE$$

where

NST: number of steering angles for each transducer position,

NTP: number of transducer positions,

NRC: number of receiver coils,

NSE: number of samples for each excitation.

To get insight about the characteristics of the sensitivity matrix, a specific row is displayed for a 16-element linear phased array transducer. Figure 4-42 shows the problem geometry used for the sensitivity calculations. In this study, the steering angle 0° is chosen, i.e., the pressure wave is propagating in the main axis (y-axis) of the transducer. Since the resultant velocity field is in x-direction, the sensitivity profile obtained for the x-coil is analyzed. The Lorentz field is calculated at t=10 μs and shown in Figure 4-43. Figure 4-44 shows the electric field distribution inside the body due to a unit reciprocal current in the x-coil. The corresponding row of the sensitivity matrix is shown in Figure 4-45.
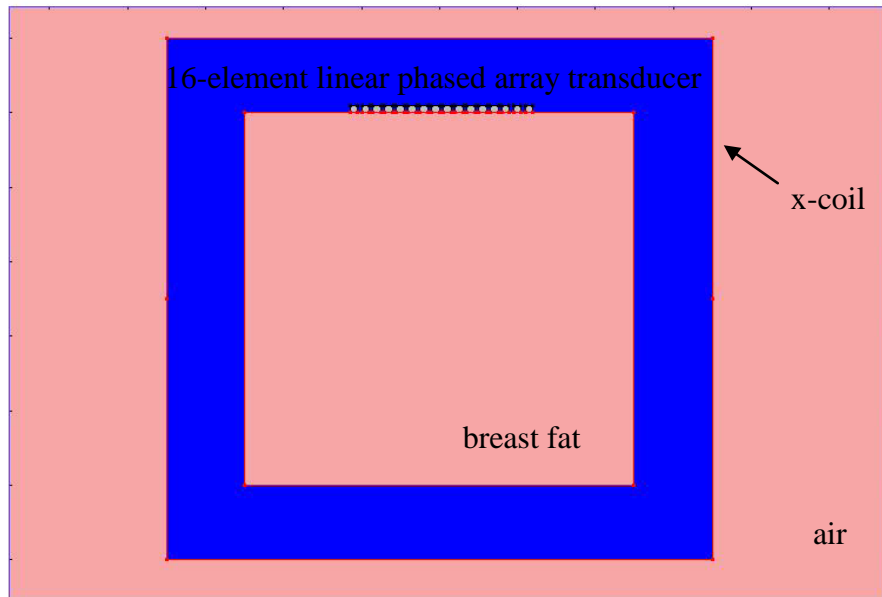
Figure 4-42 A linear 16 element phased- array transducer positioned at the upper boundary
of the body. The geometry of the receiver coil (x-coil) is also shown.
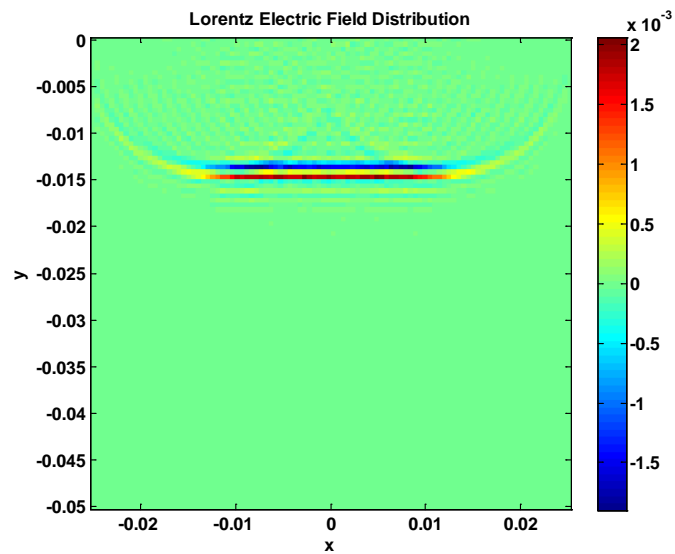
Figure 4-43 Lorentz electric field (V/m) distribution at t = 10 μs due to 16-element linear
phased array transducer.
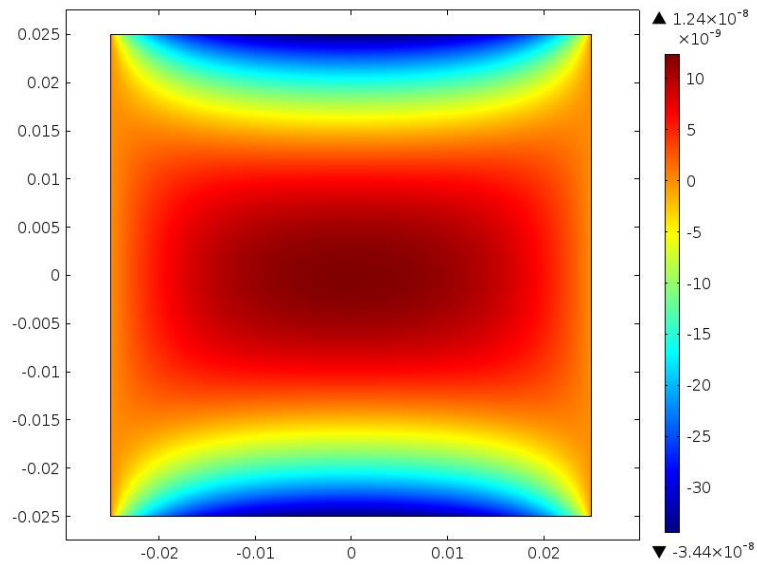
Figure 4-44 Electric field (V/m) distribution induced by the reciprocal current in the x-coil.
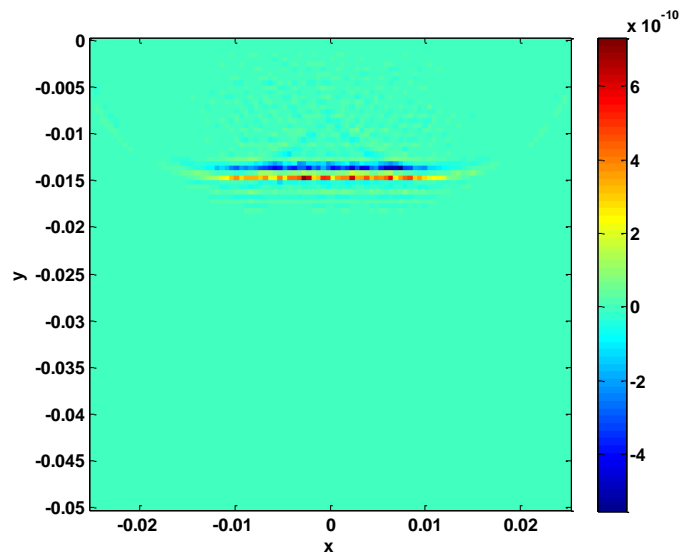
Figure 4-45 Image of the sensitivity (V·m/S) pattern for the selected transducer-coil

configuration (as shown in Figure 4-42) at t = 10 μs.

94
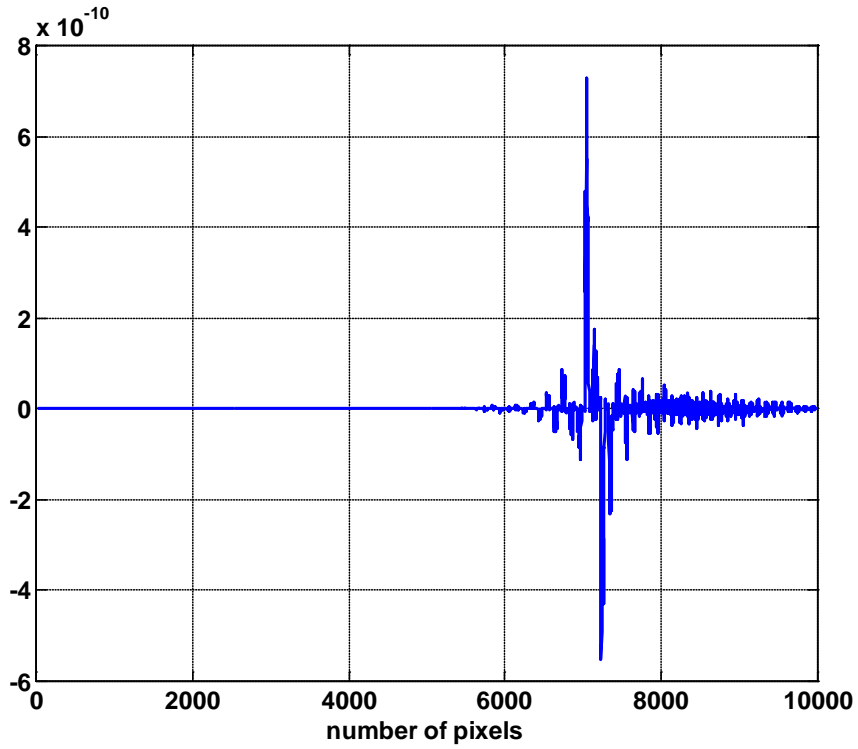
Figure 4-46 One-dimensional plot of the sensitivity (V·m/S) distribution for the specific transducer-coil configuration (Figure 4-42) at time instant t = 10 μs.

To understand the performance of the imaging system, the sensitivity matrix is analyzed using the Singular Value Decomposition (SVD). SVD of a matrix A is given as:

$$A = USV^T \qquad (4.9)$$

where U and $\mathbf{V}$ matrices are orthonormal matrices. The columns of U and V are the left-singular vectors and right-singular vectors of A, respectively. $\mathbf{S}$ is a diagonal matrix whose diagonal entries (the *singular values* of A) are arranged in the order of decreasing magnitude. The *resolution matrix* [47] calculated as,

$$R = VV^T \qquad (4.10)$$

is usually used to test the resolution properties of a linear imaging system. If n is the number of pixels in the imaging domain, then R is an nxn matrix. Note that each column or row of the resolution matrix shows the reconstructed image due to a single pixel perturbation. If the number of right singular vectors is equal to the number of unknowns, then R becomes an identity matrix (showing identical reconstruction for each perturbation). However, if there is noise in the measurements, some singular vectors corresponding to small singular values must be truncated. This yields a reduction in the number of image basis vectors used in image reconstruction and R differs from the identity matrix (Appendix C).

The resolution matrix of the proposed system is calculated assuming an SNR of 80dB. This results in limited number of basis vectors (5648) to be used in the calculation of the resolution matrix. Figure 4-47 shows a specific part of the 10000x10000 resolution matrix under this condition. The diagonal characteristic of the resolution matrix is evident; however, the magnitudes differ depending on the pixel position.

The resolution matrix can be further analyzed by generating the so-called *resolution map* of the imaging system. This map is formed using only the diagonal elements of the resolution matrix which usually represent the peak response of the system to single pixel perturbations. Figure 4-48 shows the resolution map of the generated 10000x10000 resolution matrix. It is clearly seen that the proposed imaging configuration has higher sensitivity to pixels under the transducers and has lower sensitivity to pixels away from both transducer locations. The maximum steering angle (22.5°) is also effective in this response.

Figure 4-49 shows the singular values of the sensitivity matrix normalized with the maximum singular value. The condition number is calculated as 3.29×10^{7}.
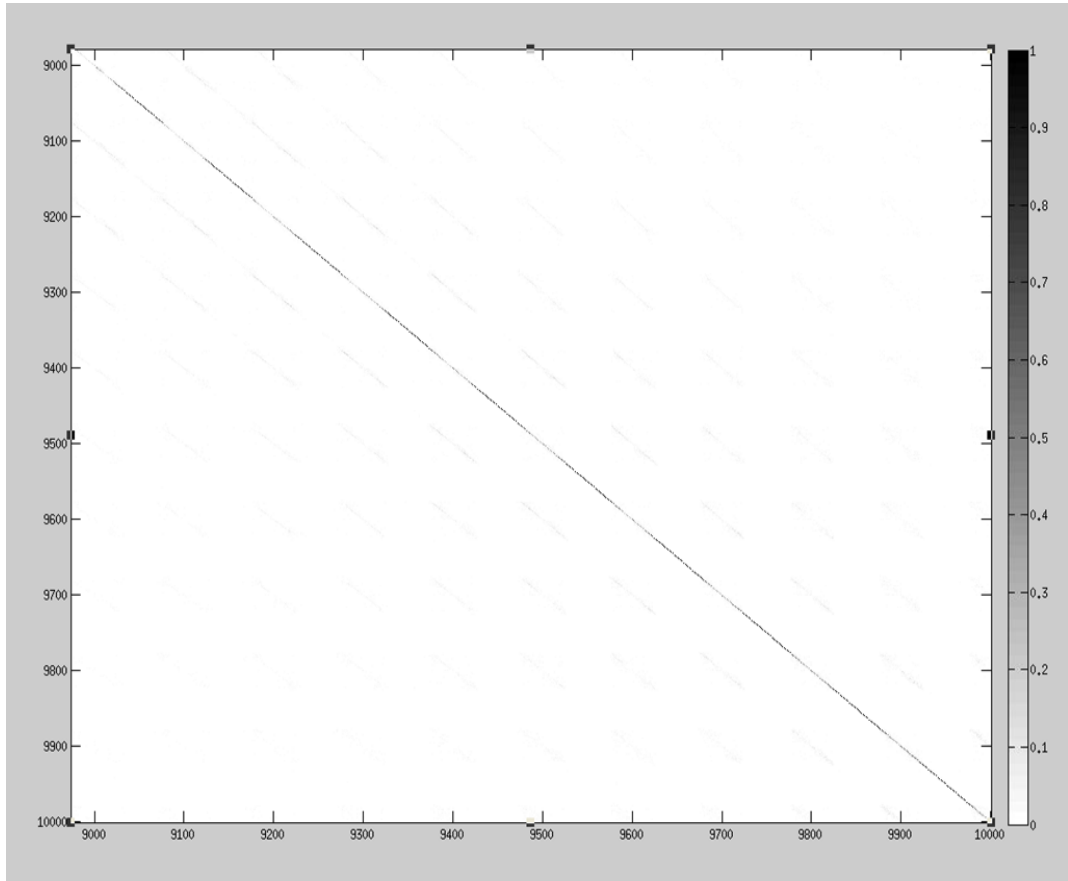
Figure 4-47 A specific portion of the resolution matrix (10000x10000) corresponding to the proposed transducer-receiver coil configuration. The receiver coils record data for a period of 32.8μs with 0.1μs sampling intervals. The transducer is located at two positions, namely, the upper and the left edges of the body. For each transducer position, the sensitivity matrix is calculated for seven steering angles   (-22.5°, -15°, -7.5°, 0°, 7.5°, 15°, 22.5°).
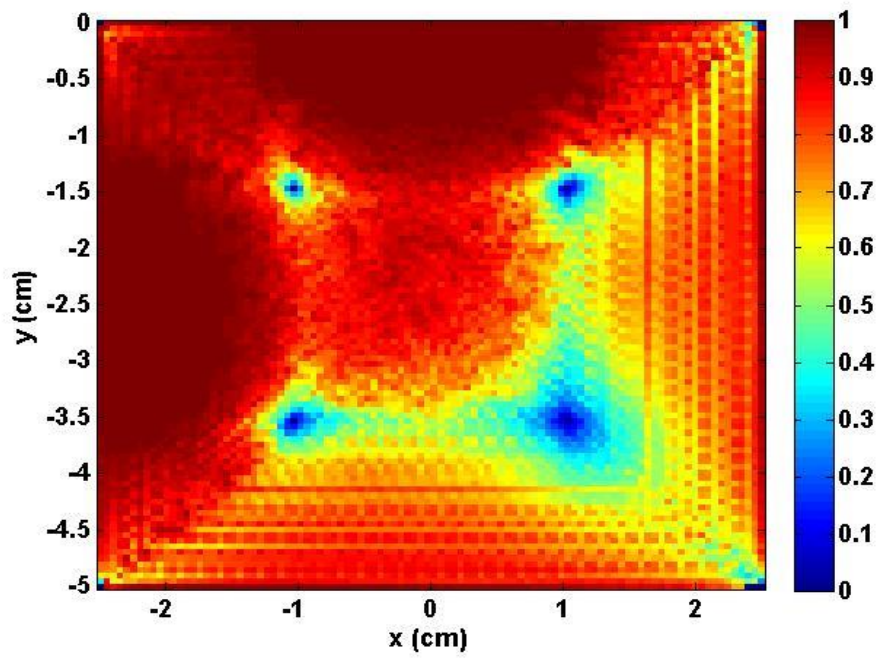
Figure 4-48 Resolution map of the 10000x10000 resolution matrix (SNR 80 dB)
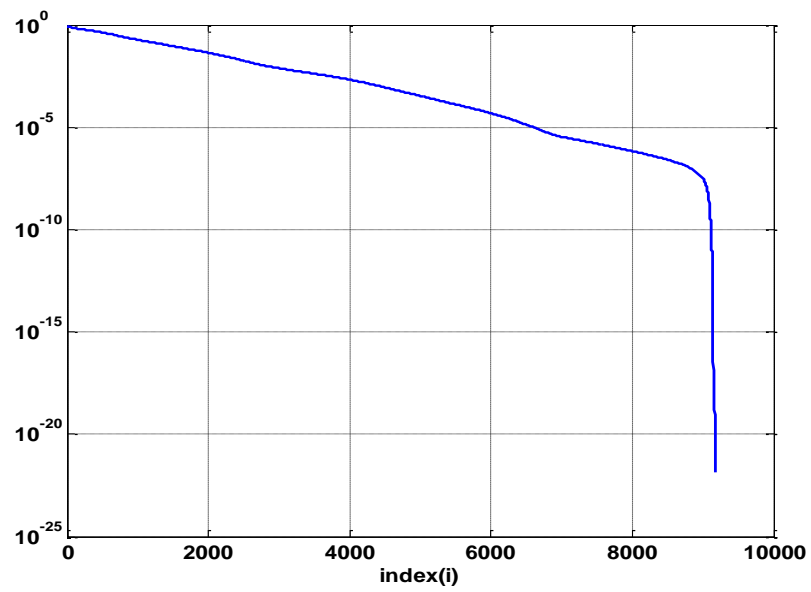
Figure 4-49 Normalized singular values of the sensitivity matrix

4.6 Image Reconstruction

In this thesis study, the Truncated SVD method is used to reconstruct the images of the conductivity distribution. If the resolution matrix R is an identity matrix, any perturbation in the imaging domain can be identically reconstructed. However, due to the noise level in the measurements the number of image basis vectors used in image reconstruction may change (Appendix C). If the number of image basis vectors (r) is less than n, then V will be $n \times r$ matrix. Consequently, the characteristics of resolution matrix R will change according to the number of truncated basis vectors.

The performance of the proposed imaging system can be assessed by simulation studies. For this purpose, two body models are prepared:

a) Model 1: A single inhomogeneity (square domain of conductivity 0.8221 S/m) located at the center of the body (at a distance of 2.5 cm from the transducers) (Figure 4-50 and Figure 4-51).

b) Model 2: Five identical inhomegeneities (square domain of conductivity 0.8221 S/m) located symmetrically in the imaging domain. One is at the center of the body; others are at 1 cm distance from the body surfaces (Figure 4-52 and Figure 4-53).

Initially, a single transducer (16 –element linear phased array) is used for excitation as shown in Figure 4-26. The sensitivity matrix is calculated for seven steering angles (-22.5°, -15°, -7.5°, 0°, 7.5°, 15°, 22.5°). Thus, the sensitivity matrix S_{Px} is of dimension 4592x10000.To assess the reconstruction performance in the case of noisy data Gaussian noise is added to the measurements. Images of the first model (Model 1) are reconstructed according to the SNRs of 20dB, 40 dB, 80 dB and with maximum SNR. Figures 4-54 through Figure 4-57 present the reconstructed images. The number of basis vectors used for different SNRs is given in Table 4-1. The

resolution in the images increases as the SNR in the measurements increases. It is observed that SNR is more demanding to improve resolution in y-direction whereas the resolution in x direction is high even at the lowest SNR in the measurements. One dimensional plots (Figures 4-58 through Figure 4-61) of the reconstructed conductivities (along x=0 line) shows that behavior more clearly.

To equalize the resolution in both directions, data is acquired for a second transducer position (Figure 4-51). Thus the number of measurements is doubled. The resultant sensitivity matrix S_{Pxy} is of dimension 9184x10000. Figure 4-62 through Figure 4-65 are the reconstructed images of Model 1. The number of basis vectors used for different SNRs is given in Table 4-2. One dimensional plots (Figures 4-66 through Figure 4-69) of the reconstructed conductivities (along x=0 line) shows the improvement in resolution.

Table 4-1Number of basis vectors for different SNRs. Single transducer excitation.

SNR (dB)	Number of basis vectors
20	783
40	1509
80	3051
137 (max)	4500

Table 4-2 Number of basis vectors for different SNRs. Two transducer excitations.

SNR (dB)	Number of basis vectors
20	1453
40	2821
80	5641
182 (max)	9100

Figure 4-70 through Figure 4-73 are the reconstructed images of Model 2. As expected, the resolution in the reconstructed images improves as the SNR in the measurement increases. A notable feature of the system is that even an SNR of 20dB yields images that show the positions and sizes of the objects correctly.
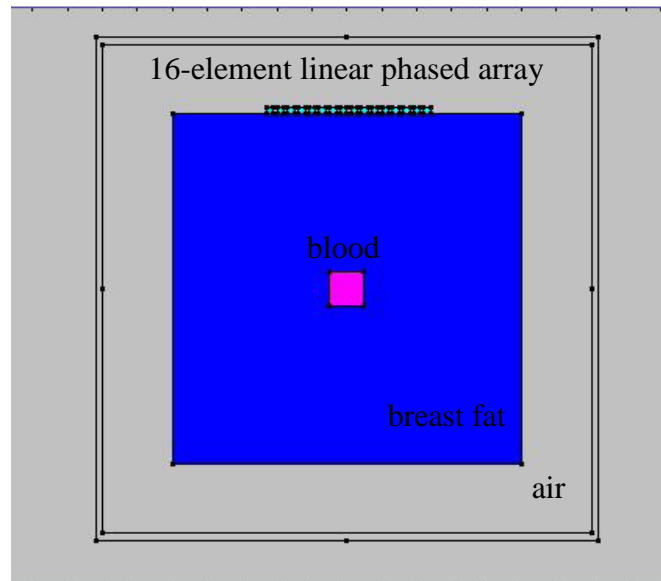
Figure 4-50 A single inhomogeneity (square domain of conductivity 0.8221 S/m) is located at the center of the body (Model 1). The transducer is placed is on the **top** side of the conductive body.
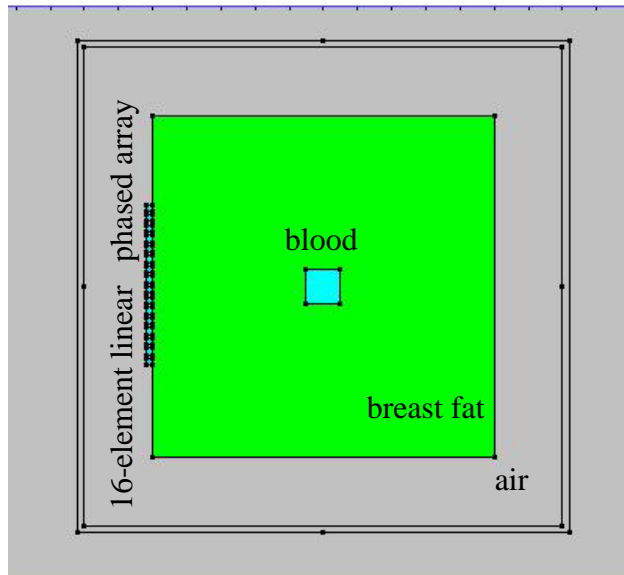
Figure 4-51 A single inhomogeneity (square domain of conductivity 0.8221 S/m) is located at the center of the body (Model 1). The transducer is placed is on the **left** side of the conductive body.
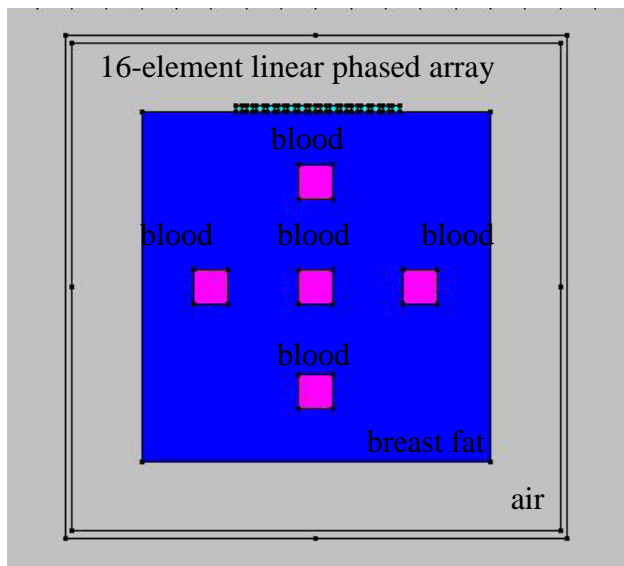
Figure 4-52 Five identical inhomegeneities (square domain of conductivity 0.8221 S/m) located symmetrically in the imaging domain (Model 2). The transducer is placed is on the **top** side of the conductive body.
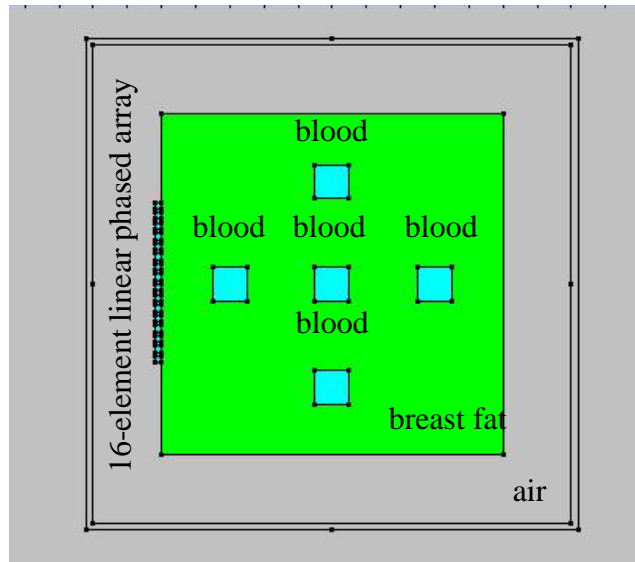
Figure 4-53 Five identical inhomegeneities (square domain of conductivity 0.8221 S/m) are located symmetrically in the imaging domain (Model 2). The transducer is placed is on the **left** side of the conductive body.
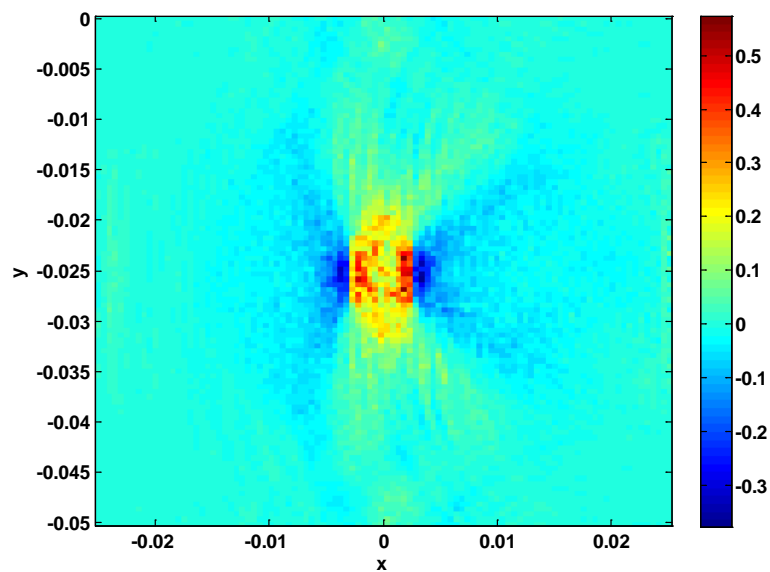
Figure 4-54 The reconstructed image of Model 1 when the SNR is 20 dB. Data is acquired using a single transducer located on the top edge of the body.
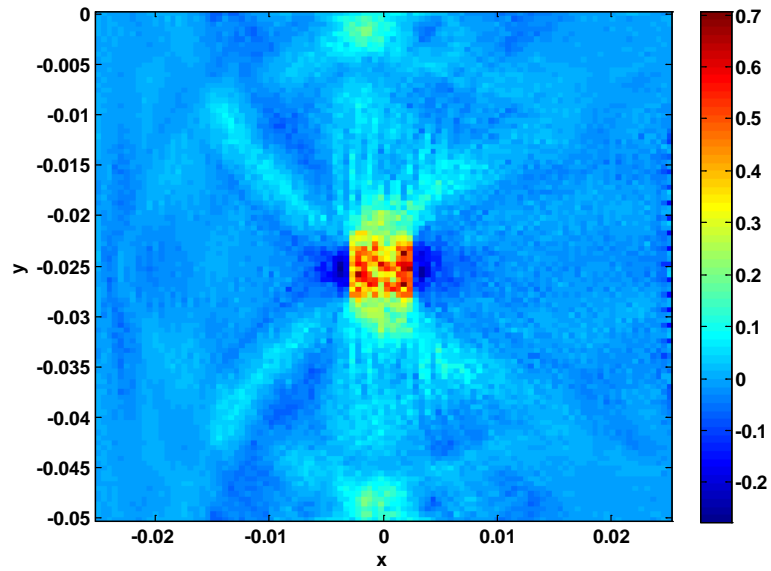
Figure 4-55 The reconstructed image of Model 1 when the SNR is 40 dB. Data is acquired using a single transducer located on the top edge of the body
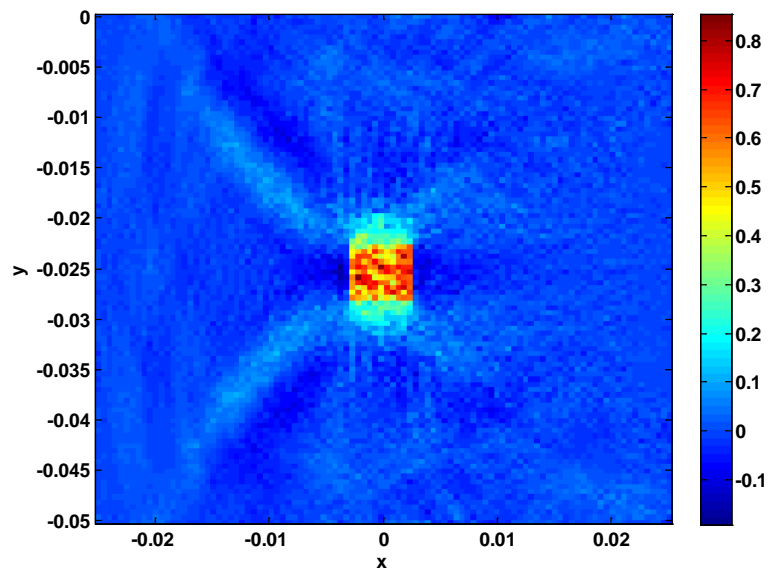
Figure 4-56 The reconstructed image of Model 1 when the SNR is 80 dB. Data is acquired using a single transducer located on the top edge of the body.
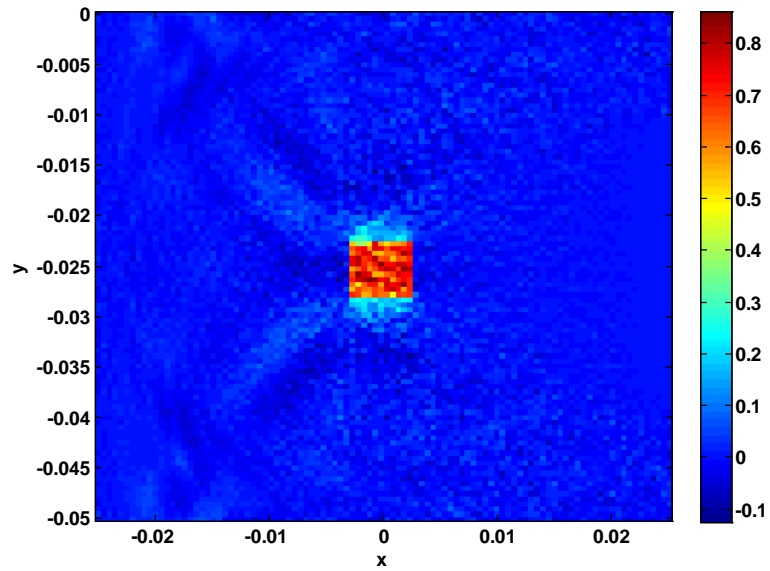
Figure 4-57 The reconstructed image of Model 1 when the SNR is maximum. Data is acquired using a single transducer located on the top edge of the body.
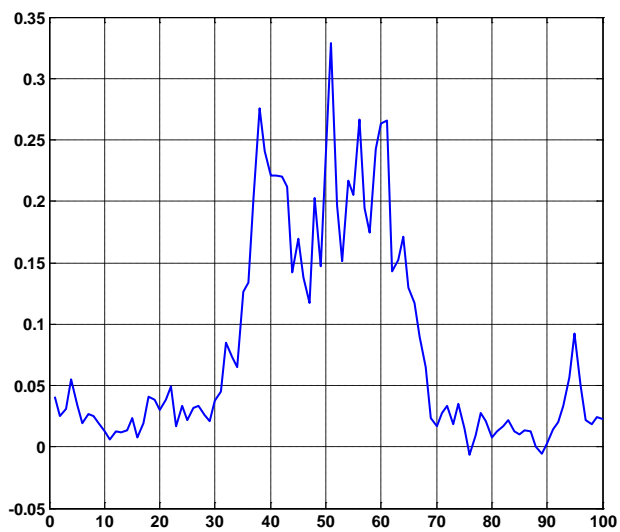
Figure 4-58 One-dimensional plot of the reconstructed conductivities (Figure 4-54) along x=0 line. SNR = 20dB.
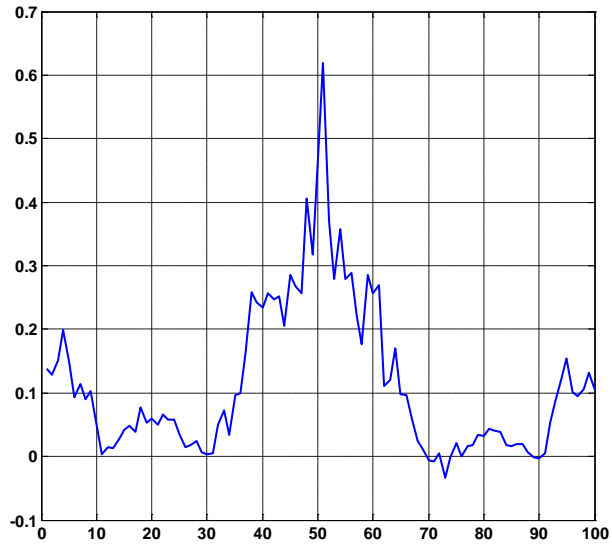
Figure 4-59 One-dimensional plot of the reconstructed conductivities (Figure 4-55) along x=0 line. SNR = 40dB
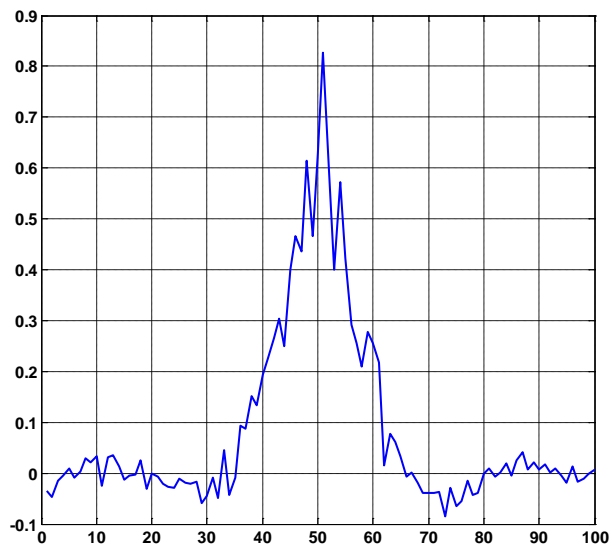
Figure 4-60 One-dimensional plot of the reconstructed conductivities (Figure 4-56) along x=0 line. SNR = 80dB

106
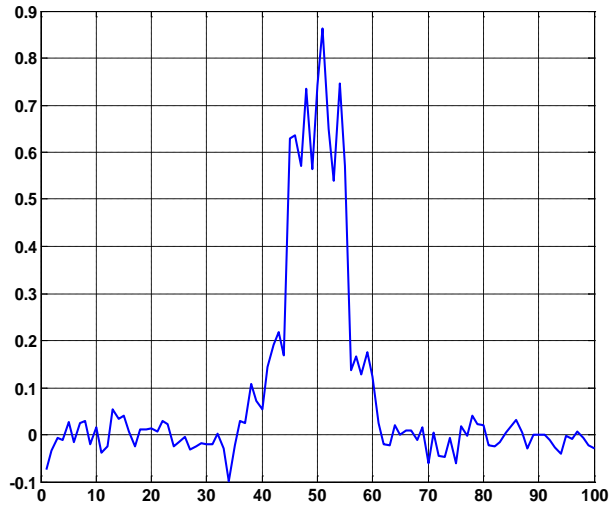
Figure 4-61 One-dimensional plot of the reconstructed conductivities (Figure 4-57) along x=0 line. SNR = 182dB
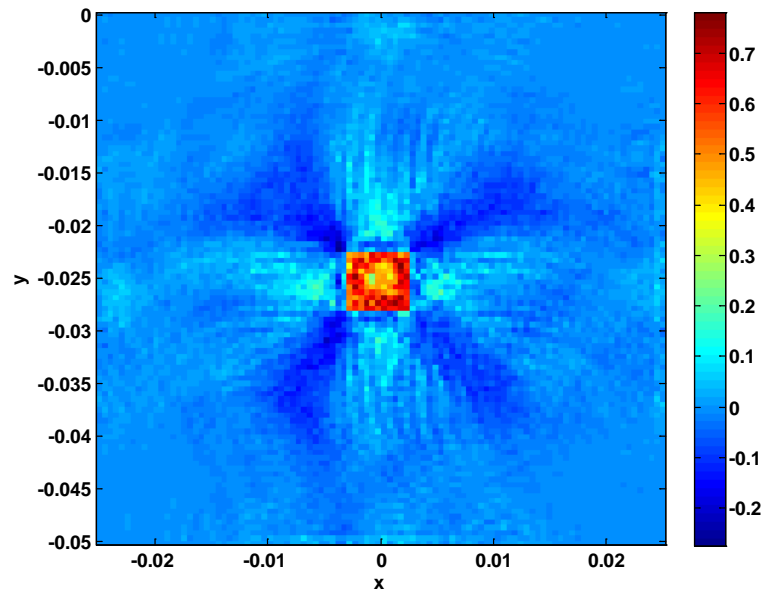
Figure 4-62 The reconstructed image of Model 1 when the SNR is 20 dB. Data is acquired using two transducer positions.

107
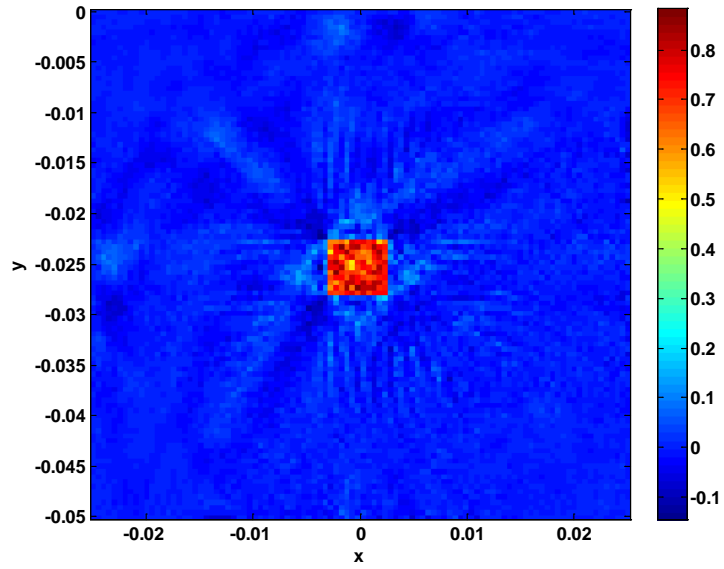
Figure 4-63 The reconstructed image of Model 1 when the SNR is 40 dB. Data is acquired using two transducer positions.
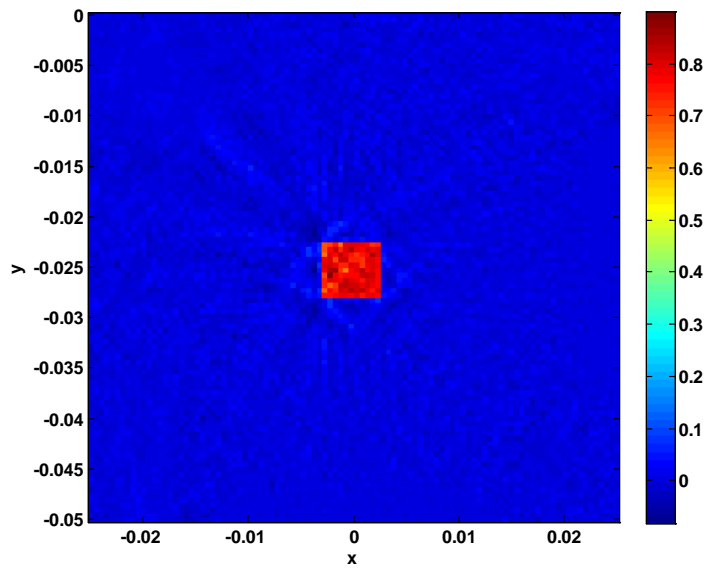
Figure 4-64 The reconstructed image of Model 1 when the SNR is 80 dB. Data is acquired using two transducer positions.
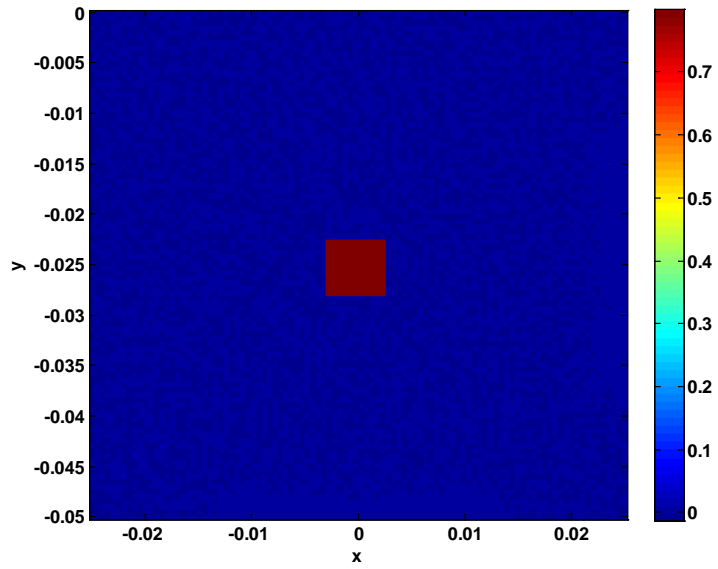
Figure 4-65 The reconstructed image of Model 1 when the SNR is 182 dB. Data is acquired using two transducer positions.
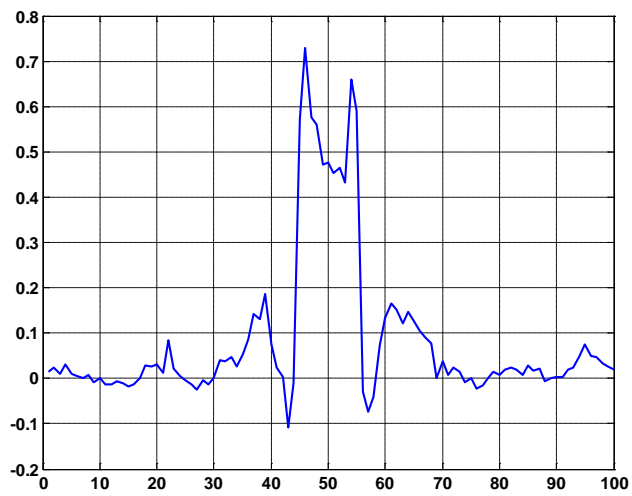
Figure 4-66 One-dimensional plot of the reconstructed conductivities (Figure 4-62) along x=0 line. SNR = 20dB.
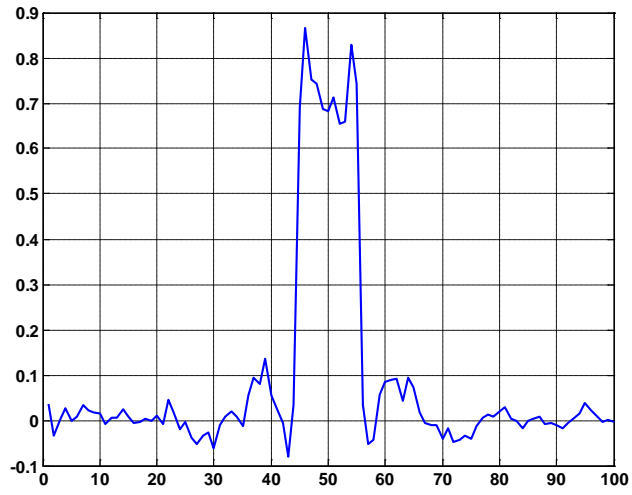
Figure 4-67 One-dimensional plot of the reconstructed conductivities (Figure 4-63) along x=0 line. SNR = 40dB.
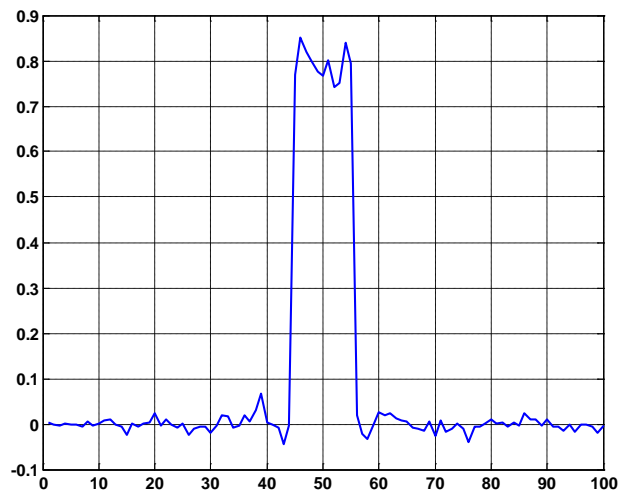
Figure 4-68 One-dimensional plot of the reconstructed conductivities (Figure 4-64) along x=0 line. SNR = 80dB.

110
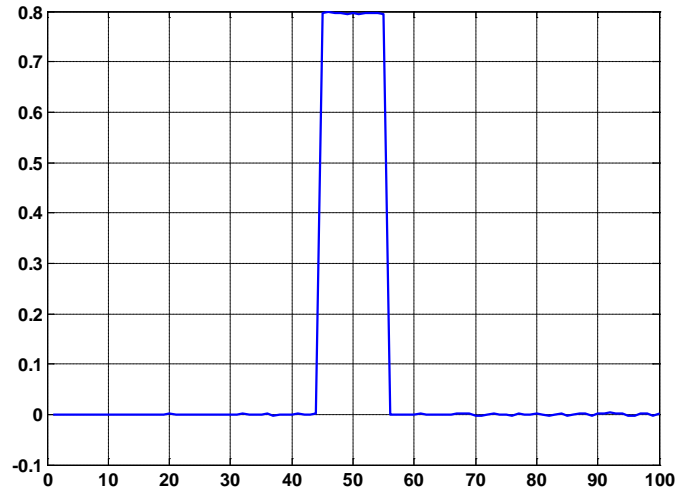
Figure 4-69 One-dimensional plot of the reconstructed conductivities (Figure 4-65) along x=0 line. SNR = 182dB.
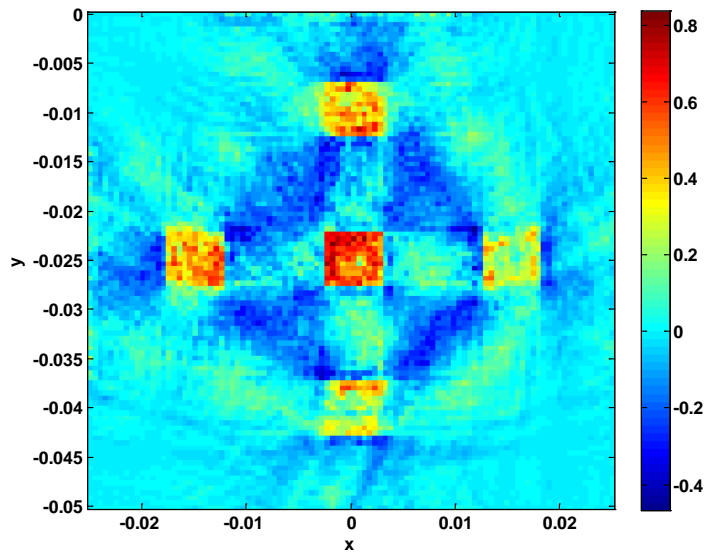
Figure 4-70 The reconstructed image of Model 2 when the SNR is 20 dB. Data is acquired using two transducer positions.
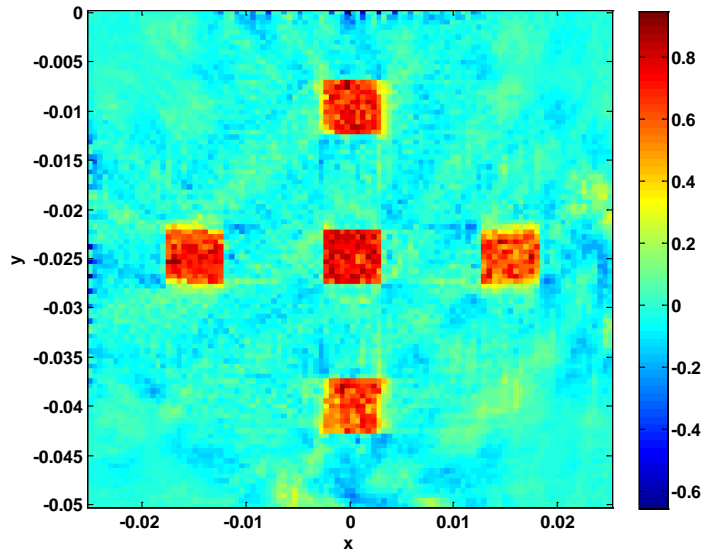
Figure 4-71 The reconstructed image of Model 2 when the SNR is 40 dB. Data is acquired using two transducer positions.
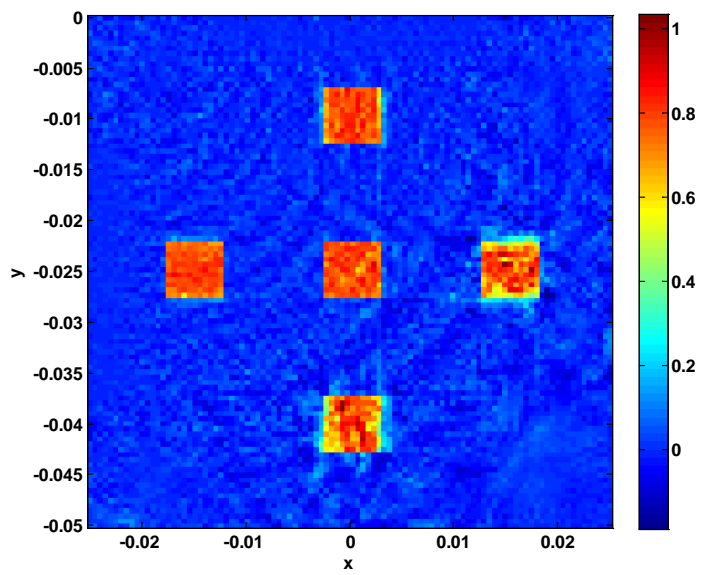
Figure 4-72 The reconstructed image of Model 2 when the SNR is 80 dB. Data is acquired using two transducer positions.
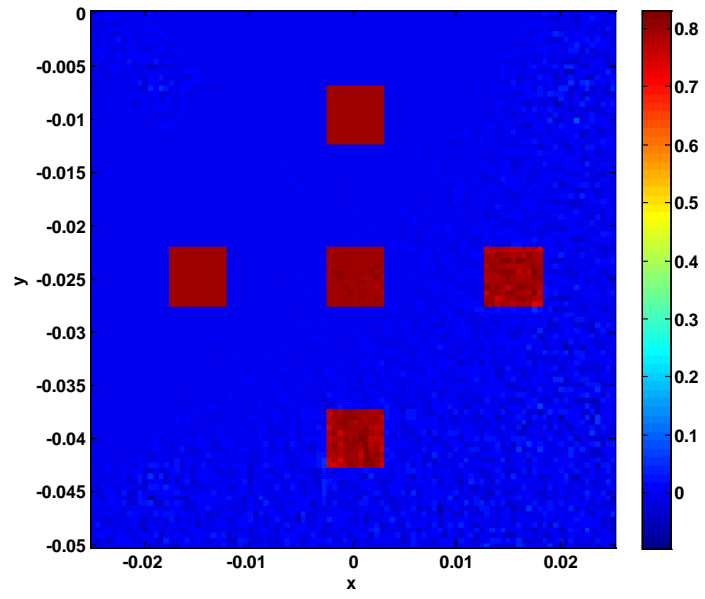
Figure 4-73 The reconstructed image of Model 2 when the SNR is 80 dB. Data is acquired using two transducer positions.

CHAPTER 5

CONCLUSION AND DISCUSSION

In this study a new imaging modality is proposed to image electrical conductivity of body tissues. This modality is based on the magnetic field measurements generated by ultrasonically induced Lorentz fields. The magnetic fields are measured using two coils encircling the body. The two coil configurations (x- and y-coils) are designed to be sensitive to currents in x- and y- directions, respectively. The properties of the proposed approach are revealed by exploiting the multiphysics characteristics (acoustic, piezoelectric, and electromagnetic) involved in its different phases. Basic field equations governing the behavior of the time-varying acoustic and electromagnetic fields are reviewed. The relation between the measurements and conductivity distribution is derived. The resulting formulation is linearized around an initial conductivity distribution. The characteristics of the imaging system are studied by analyzing the sensitivity matrix using the SVD. The performance of the imaging system is investigated using simulation studies.

This proposed imaging modality is based on the results reported for Hall Effect Imaging [48]. Since the theory and basic assumptions behind the forward problem of Hall Effect Imaging was not discussed elsewhere, the initial phase of this thesis study is to reveal the corresponding theory. Thereafter, the forward problem of the proposed approach is described. Magnetic fields of the induced velocity current propagation and their relation to body conductivity distributions are explained. The lead field analyses are described for the new measurement system for two different

114

excitations, namely, the time harmonic excitation, and pulse type excitations. The imaging performance for the pulse-type excitations are discussed in detail. The results show the potent of this new imaging modality.

Comments and discussions on different phases of this study are listed below.

Numerical Modeling: The characteristics of the forward problem are analyzed using finite element based commercial software (Comsol Multiphysics). In the numerical modeling, the pressure acoustic, piezoelectric and electromagnetic modules are coupled whenever it is necessary in the solution of the forward problem. In the *piezoelectric module*, a single element transducer and 16-element linear phased array transducer are modeled with PZT-5H material. Inverse piezoelectric effect is performed by exciting each transducer with time-varying electrical potentials. In this study, the transducers are excited with a sinusoidal potential of one cycle. The piezoelectric crystals can be excited with longer sinusoidal potentials or tone burst potentials that may yield different characteristics in the imaging system.

In the *pressure acoustic module*, the acoustic properties of the homogeneous and inhomogeneous regions are modeled with the two major tissues in the breast (i.e., breast fat and breast fat with blood). The pressure generated in the body should be originated from a pressure source. In this study, the outputs of the piezoelectric module are assumed as the primary pressure source. The interaction of the velocity currents with the static magnetic field is also taken into account as an acoustic dipole source to the pressure module. In this study, the acoustic fields of crystals with a resonance frequency of 1 MHz are considered. The acoustic behavior and corresponding effects in the image reconstruction performance must be investigated for different excitation frequencies.

In this study, only two-dimensional numerical models are used. The performance of the system must be further investigated using three-dimensional models.

Receiver coil design: A novel coil configuration is proposed to detect the ultrasonically induced Lorentz fields. This coil configuration is consisting of two

coils (x- and y-coils). A better coil (or even a dipole antenna) can be designed to improve the system properties.

Note that, once the excitation is known, by simply analyzing the induced voltages in the receiver coils, one can have an insight about the inhomogeneity inside the bodies. Specific coils can be designed to follow the conductivity changes on a specific line. Time gated amplification can be employed to remove the attenuation affects with depth.

Sensitivity Matrix Analysis: The geometry and location of the transducer and receiver coils are important parameters in sensing the inhomogeneity in the body. In this study, a 16-element linear phased array transducer is assumed on the upper edge of the conductive body. To improve the sensitivity, the transducer is also placed on the left edge. The receiver coils are placed encircling the body and transducer. The characteristics of the system are revealed by analyzing the sensitivity matrix and resolution maps. It is observed that the proposed system has higher sensitivity under the transducer and around the center of body; however, it has lower sensitivity around the corners. The developed analysis tools must be employed to design a better transducer/coil configuration that yields homogeneous sensitivity to the conductivity perturbations.

Image Reconstruction: In this thesis study, the mathematical basis of a new imaging modality is presented. To reconstruct the conductivity images only a single algorithm, namely, the Truncated SVD is used. The performance of other reconstruction algorithms must be further investigated.

To develop a more practical and faster imaging system, techniques must be developed to reconstruct images without using matrix inversions.

Safety considerations: Precautions should be taken by keeping the excitation potential of ultrasound transducers below a threshold in order not to cause destructive heating. Ultrasonic transducers used for diagnostic purposes do not cause destructive heating in the human body [49]. The ultrasonic transducers used in our

simulations are excited with amplitude of 1V at 1 MHz frequency and definitely do not cause any harm to the body tissues.

The induced current density in the body should also be under the safety limits. In our simulations the induced velocity current densities are approximately 0.2 mA/m^2 and 5 mA/m^2 for homogeneous and inhomogeneous body, respectively. These current densities are below the safety limits at 1 MHz [50].

Future Work: The following topics can be further investigated:

- Time-harmonic imaging and corresponding coil configurations.
- The effects of the number of steering angles on the image resolution.
- The focusing property of the linear phased array transducers.
- The use of the proposed approach employing other ultrasonic transducers (see Appendix A).
- The use of multi-frequency excitations.
- Three-dimensional simulations for different transducer types and for different perturbations.
- Data acquisition system design for time-harmonic and pulse excitations.
- Experimental studies conducted using phantoms and animals and research on clinical applications.
- In this study, the beam steering properties of linear phased array transducers are employed to steer electrical currents inside a conductive body. The methodology can be further extended to obtain magnetic field measurements inside the body using Magnetic Resonance Imaging systems. This will definitely improve the resolution in the resultant conductivity images.

REFERENCES

[1]   Foster KR. Dielectric Properties of Tissues. The Biomedical Engineering Handbook: Second Edition, vol. 89. CRC Press, 2000.

[2]   Peters MJ, Stinstra JG, Hendriks M. Estimation of the electrical conductivity of human tissue. Electromagnetics 2001;21:545.

[3]   Chauveau N, Ayeva B, Rigaud B, Morucci JP. A multifrequency serial EIT system. Physiological Measurement 1996;17:A7.

[4]   Fedorowski A, Steciwko A. Biological effects of non-ionizing electromagnetic radiation. Med. Pr., 1998.

[5]   Barber DC, Brown BH. Applied Potential Tomography. Journal of Physics E-Scientific Instruments 1984;17:723.

[6]   Paulson K, Lionheart W, Pidcock M. Optimal Experiments In Electrical-Impedance Tomography. Ieee Transactions on Medical Imaging 1993;12:681.

[7]   Metherall P, Barber DC, Smallwood RH, Brown BH. Three-dimensional electrical impedance tomography. Nature 1996;380:509.

[8]   Gencer NG. Electrical impedance tomography using induced currents. Electrical and Electronics Engineering, vol. Ph.D.: Middle East Technical University, 1993.

[9]   Gencer NG, Kuzuoglu M, Ider YZ. Electrical-Impedance Tomography Using Induced Currents. Ieee Transactions on Medical Imaging 1994;13:338.

[10]   Freeston IL, Tozer RC. Impedance Imaging Using Induced Currents. Physiological Measurement 1995;16:A257.

[11]   Brandstatter B, Hollaus K, Hutten H, Mayer M, Merwa R, Scharfetter H. Direct estimation of Cole parameters in multifrequency EIT using a regularized Gauss-Newton method. Physiological Measurement 2003;24:437.

[12]   Fitzgerald AJ, Thomas BJ, Cornish BH, Michael GJ, Ward LC. Extraction of electrical characteristics from pixels of multifrequency EIT images. Physiological Measurement 1997;18:107.

[13]   Hampshire AR, Smallwood RH, Brown BH, Primhak RA. Multifrequency And Parametric Eit Images Of Neonatal Lungs. Physiological Measurement 1995;16:A175.

119

[14]   Mayer M, Brunner P, Merwa R, Smolle-Juttner FM, Maier A, Scharfetter H. Direct reconstruction of tissue parameters from differential multifrequency EIT in vivo. Physiological Measurement 2006;27:S93.

[15]   Zhang S, Xu G, Wu H, Geng D, Yan W. Multi-frequency EIT Hardware System Based on DSP.

[16]   Scott GC, Joy MLG, Armstrong RL, Henkelman RM. Sensitivity Of Magnetic-Resonance Current-Density Imaging. Journal of Magnetic Resonance 1992;97:235.

[17]   Scott GC, Joy MLG, Armstrong RL, Henkelman RM. Measurement Of Nonuniform Current-Density By Magnetic-Resonance. Ieee Transactions on Medical Imaging 1991;10:362.

[18]   Joy M, Scott G, Henkelman M. Invivo Detection Of Applied Electric Currents By Magnetic-Resonance Imaging. Magnetic Resonance Imaging 1989;7:89.

[19]   Zhang N. Electrical impedance tomography based on current density imaging. Electrical Engineering, vol. MS: University of Toronto, 1992.

[20]   Gao N, He B. Noninvasive imaging of bioimpedance distribution by means of current reconstruction magnetic resonance electrical impedance tomography. Ieee Transactions on Biomedical Engineering 2008;55:1530.

[21]   Ider YZ, Onart S. Algebraic reconstruction for 3D magnetic resonance-electrical impedance tomography (MREIT) using one component of magnetic flux density. Physiological Measurement 2004;25:281.

[22]   Kwon O, Woo EJ, Yoon JR, Seo JK. Magnetic resonance electrical impedance tomography (MREIT): Simulation study of J-substitution algorithm. Ieee Transactions on Biomedical Engineering 2002;49:160.

[23]   S A-Z, D G, G L, Z YZ, J PA, S BM. A feasibility study of electromagnetic induction tomography. 9th Int Conf On Electrical Bio-Impedance. Heidelberg, 1995. p.426.

[24]   Al-Zeibak S, Goss D, Lyon G, Yu ZZ, Peyton AJ, Beck MS. A feasibility study of electromagnetic induction tomography. 9th Int Conf On Electrical Bio-Impedance. Heidelberg, 1995. p.426.

[25]   Gencer NG, Tek N. Imaging Tissue Conductivity via Contactless Measuremens: A Feasibility Study. vol. 6(3). Turkish Journal of Electrical Engineering ELEKTRIK, 1998. p.167.

[26]   Griffiths H. Magnetic induction tomography. Measurement Science & Technology 2001;12:1126.

[27]   Towe BC, Islam MR. A Magnetoacoustic Method For The Noninvasive Measurement Of Bioelectric Currents. Ieee Transactions on Biomedical Engineering 1988;35:892.

[28]   Roth BJ, Basser PJ, Wikswo JP. A Theoretical-Model For Magnetoacoustic Imaging Of Bioelectric Currents. Ieee Transactions on Biomedical Engineering 1994;41:723.

[29]   Roth BJ, Wikswo JP. Comments on "Hall effect imaging". Ieee Transactions on Biomedical Engineering 1998;45:1294.

[30]   Xu Y, He B. Magnetoacoustic tomography with magnetic induction (MAT-MI). Physics in Medicine and Biology 2005;50:5175.

[31]   Li X, Xu Y, He B. Magnetoacoustic tomography with magnetic induction for imaging electrical impedance of biological tissue. Journal of Applied Physics 2006;99.

[32]   Xia RM, Li X, He B, Ieee. Magnetoacoustic tomography of biological tissue with magnetic induction, 2007.

[33]   Brinker K, Roth BJ. The effect of electrical anisotropy during magnetoacoustic tomography with magnetic induction. Ieee Transactions on Biomedical Engineering 2008;55:1637.

122

[34]   Webb AG. Introduction to Biomedical Imaging, 2002.

[35]   Erikson KR, Fry FJ, Jones JP. Ultrasound In Medicine - Review. Ieee Transactions on Sonics and Ultrasonics 1974;SU21:144.

[36]   Wells PNT. Biomedical Ultrasonics. London: Academic Press, 1977.

[37]   Plonsey R, Collin R. Principles and Applications of Electromagnetic Fields. NewYork: Mc.Graw-Hill, 1961.

[38]   Gabriel C, Gabriel S, Corthout E. The dielectric properties of biological tissues .1. Literature survey. Physics in Medicine and Biology 1996;41:2231.

[39]   Gabriel S, Lau RW, Gabriel C. The dielectric properties of biological tissues .2. Measurements in the frequency range 10 Hz to 20 GHz. Physics in Medicine and Biology 1996;41:2251.

[40]   Gabriel S, Lau RW, Gabriel C. The dielectric properties of biological tissues .3. Parametric models for the dielectric spectrum of tissues. Physics in Medicine and Biology 1996;41:2271.

[41]   Cheng DK. Fundamentals of Engineering Electromagnetics, 1993.

[42]   Carley M. Some Notes on Acoustics. 2001.

[43]   Zielinski TG. Fundamentals of multiphysics modelling of piezo-poro-elastic structures. Archives of Mechanics 2010;62:343.

[44]   Comsol Help.

[45]   Mortarelli JR. A Generalization Of The Geselowitz Relationship Useful In Impedance Plethysmographic Field Calculations. Ieee Transactions on Biomedical Engineering 1980;27:665.

[46]   Cheo BR. A Reciprocity Theorem For Electromagnetic Fields With General Time Dependence. Ieee Transactions on Antennas and Propagation 1965;AP13:278.

[47]   Gencer NG, Tek MN. Electrical conductivity imaging via contactless measurements. Ieee Transactions on Medical Imaging 1999;18:617.

[48]   Wen H, Shah J, Balaban RS. Hall effect imaging. Ieee Transactions on Biomedical Engineering 1998;45:119.

[49]   Azhari H. Basics of Biomedical Ultrasounds for Engineers: A John Wiley & Sons , Inc., Publication, 2010.

[50]   Lionheart WRB, Kaipio J, McLeod CN. Generalized optimal current patterns and electrical safety in EIT. Physiological Measurement 2001;22:85.

[51]   Curie P, Curie J. Development par pression de l'elctricite polaire dans les cristaux hemiedres a faces encliness. Comp Rend, 1980.

[52]   Goldberg RL, Smith SW, Moottley JG, Ferrara KW. Ultrasound. In: Mudry KM, Plonsey R, Bronzino JD, editors. Principles and Applications in Engineering Series- Biomedical Imaging. 2003.

[53]   Allen JL. Array antennas: New applications for an old technique. IEEE Spect, vol. 1, 1964.

[54]   Bobber RJ. Underwater Electroacoustic Measurements. Washington: Naval Reseach Laboratory, 1970.

[55]   Somer JC. Electronic Sector Scanning For Ultrasonic Diagnosis. Ultrasonics 1968;6:153.

[56]   Vonramm OT, Thurstone FL. Cardiac Imaging Using A Phased-Array Ultrasound System .1. System-Design. Circulation 1976;53:258.

[57]   Goss SA, Johnston RL, Dunn F. Comprehensive Compilation Of Empirical Ultrasonic Properties Of Mammalian-Tissues. Journal of the Acoustical Society of America 1978;64:423.

APPENDIX A

ULTRASONIC TRANSDUCERS

A.1 Transducers

The acoustic waves can be generated in many ways. These waves are induced by converting magnetic, thermal and electrical energy into mechanical energy. In medical applications of ultrasound the piezoelectric effect plays a key role in several techniques. Piezoelectric effect was first introduced in 1880 [51] which implies that applying a stress to the quartz crystal causes an electrical potential across opposite face of the material. In addition, the inverse event was observed, which shows applying an electric field across the crystal could result in mechanical deformation. By the leading of this innovation, many significant advances have been observed in ultrasound imaging. As one of these advances we can mention to the development of linear-array transducers. At first, transducer was moving manually to the region of interest, which had taken many seconds. In this approach, only static objects could be scanned. As a result of fast scanning, moving objects can also be scanned for real-time imaging. For this purpose, researchers developed different types of ultrasound transducers which steer the acoustic beam, rapidly. Some of them can steer the beam mechanically, and some other can steer and focus electronically. Linear phased array transducers are the ones that can steer and focus the beam electronically [52].

A.1.1 Transducer Materials- PZT

The ferroelectric materials are the well-known materials in medical ultrasound to exhibit the piezoelectric effect. Having low intrinsic losses and high electromechanical conversion efficiency makes a ferroelectric material called ceramic lead zirconate-titanate (PZT), a proper choice as a standard transducer material for medical ultrasound [52] . In Table A-1 the properties of linear array elements made of PZT are shown.

Table A-1 Material Properties of Linear-Array Elements Made of PZT-5H [52]

Parameter	Symbol	Value	Units
Density	ρ	7500	kg/m^3
Speed of sound	c	3970	m/s
Acoustic impedance	Z	29.75	MRayls
Relative dielectric constant	$\varepsilon/\varepsilon_0$	1475	None
Electromechanical coupling coefficient	k	0.698	None
Mechanical loss tangent	$\tan \delta_m$	0.015	None
Electrical loss tangent	$\tan \delta_e$	0.02	None

Advantages of PZT [52]:

- PZT has a high dielectric constant.
- Ceramic is mechanically strong.
- Ceramic can be performed to different shapes and sizes.
- PZT is suitable for 100° C or higher.
- PZT is stable for long periods of time.

Disadvantages of PZT [52]:

- PZT has high acoustic impedance (Z=30 MRayls) as compared with human body (Z=1.5 MRayls).
- PZT has lateral modes in array elements.

However, the first disadvantage can be eliminated by using acoustic matching layer to compensate the acoustic impedance mismatch. The second disadvantage can be diminished by using appropriate element sizes. There are also some different piezoelectric materials which can be used for various applications [52].

A.2 Scanning with Array Transducers

The principles of acoustic lenses are used exactly the same way in array transducers. For acoustic lenses and array transducers, during the transducer aperture different delays are applied. Since delays can be directed electronically, the beam can be focused in different regions [52]. Linear phased arrays were first introduced for radar, sonar and radio astronomy [53, 54] . The applications of them in medical ultrasound was introduced by Somer in 1968 [55, 56].

In electronically scanning where the transducers do not move, only the focal point can be changed, dynamically. To have high-quality ultrasound images, many identical array elements are required; generally 128 and more number of array elements is used. Typically, an array element is less than a millimeter on one side. There is a connection between each side of element for transmitter and receiver electronics [52].

A.2.1 Focusing and Steering with Phased Arrays

A phased array transducer can focus and steer an acoustic beam in different directions. By repeating this process several times in 2D or 3D medium, an ultrasound image can be obtained [52].

An example for focusing the transmitted beam with six-element array is shown in Figure A-1. Each element acts as a point source and radiates a spherically shaped wave front into the medium. In this example, the first element is excited first, since it is located in the farthest place from the focus. The other elements are excited with different time delays so that all excitation signals arrive to the transmit focus at the same time. Due to the Huygens's principle, the final acoustic signal is the sum of all arrived signal to the focus point [52].
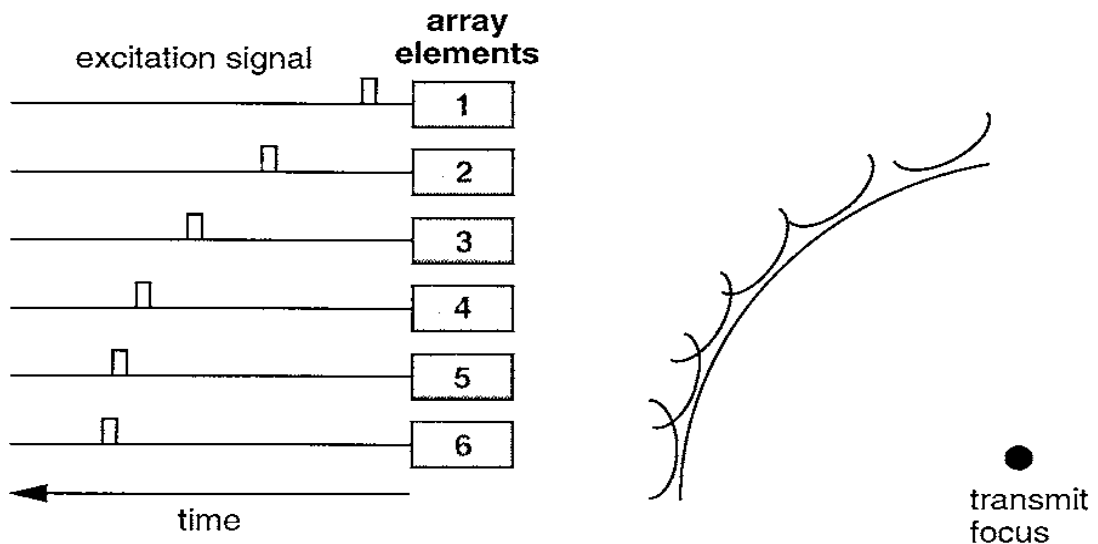
Figure A-1 Focusing and steering an acoustic beam with a six-element linear array in the transmit mode [52]

The phased array works in reverse for receiving an ultrasound echo. In Figure A-2 echo comes from focus 1. At a different time delays this echo is incident on each element. The resultant (received) signals are electronically delayed. These delayed signals add in phase for an echo originating at the focal point.

The focal point can be dynamically adjusted in the receive mode. After an acoustic pulse is transmitted, the initial echoes return from the targets that placed near the transducer. Thus, the ultrasound scanner can focus on these targets which can be seen in Figure A-2 as focus 1. When echoes return from more distant targets, the scanner can focus at a greater depth as focus 2 (Figure A-2). To make the targets to be in focus in receive mode, focal zones are set with adequate depth. This process is called as dynamic receive focusing [56].
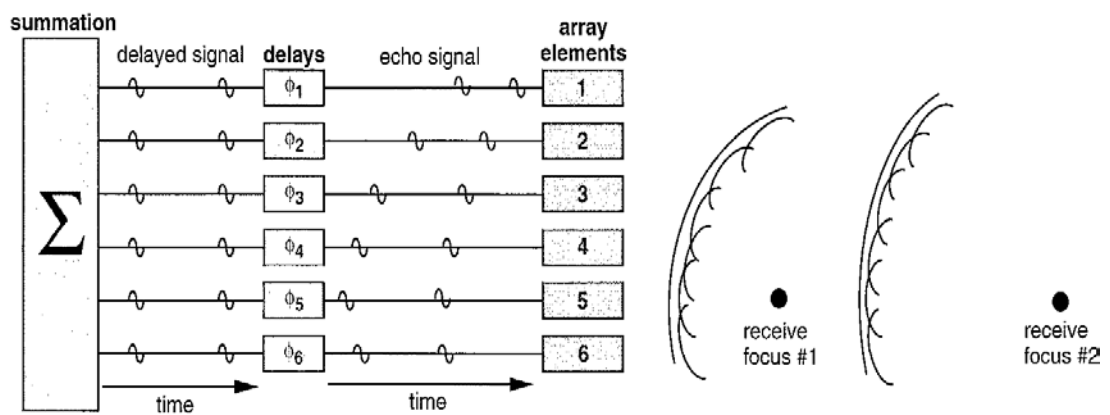
Figure A-2 Focusing and steering an acoustic beam with a six-element linear array in the receive mode [52]

131

A.2.2 Array-Element Configurations

By repeating scanning process as steering or focusing many times, an ultrasound image of tissue is formed in 2D or 3D region. In 2D image, azimuth dimension represents the scanning plane; the elevation dimension is perpendicular to the scanning plane. With different array-element configurations, the shape of the region scanned is determined. The following descriptions are for different array-element configurations [52]:

Linear Sequential Arrays:

These arrays have 512 elements in commercial scanners. The acoustic beam is focused, since the scanning lines are directed perpendicular to the face of the transducer. However, the acoustic beam cannot steer. Since the beam is directed straight ahead, the array elements have high sensitivity. However, the field of view is limited to the rectangular region where is placed directly in front of the transducer [52]. In Figure A-3 this configuration is shown.
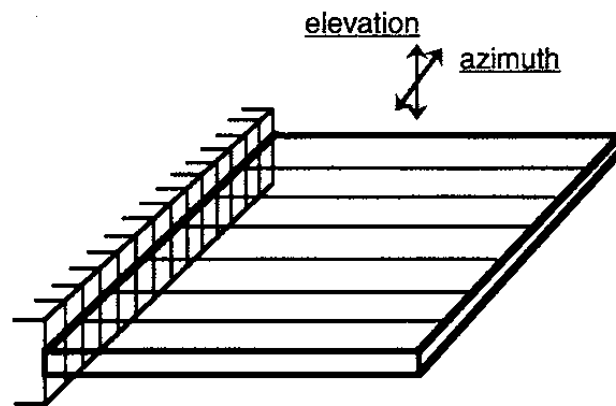
Figure A-3 Array-element configuration for linear sequential array [52]

Curvilinear Arrays:

The shape of these arrays is different than linear arrays, but their operation is in the same manner. However, curvilinear arrays can scan a wider field of view because of their convex shapes [52], as in Figure A-4.
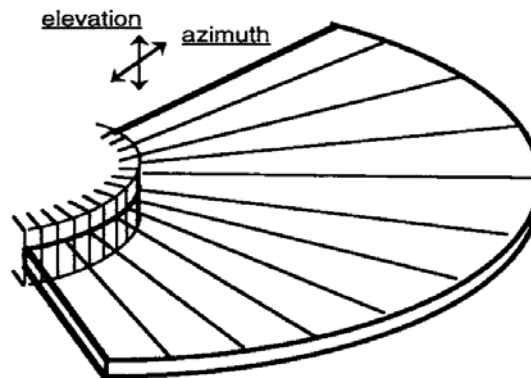
Figure A-4 Array-element configuration for curvilinear array [52]

Linear Phased Arrays:

All elements of linear phased array are used to transmit and receive each line of data. Generally, they have 128 elements. In medical imaging linear phased arrays are used in common. These arrays are built from many small rectangular elements lined up with a very thin gap between each element. Figure A-5. shows these arrays as steering the beam through a sector-shaped region [52].
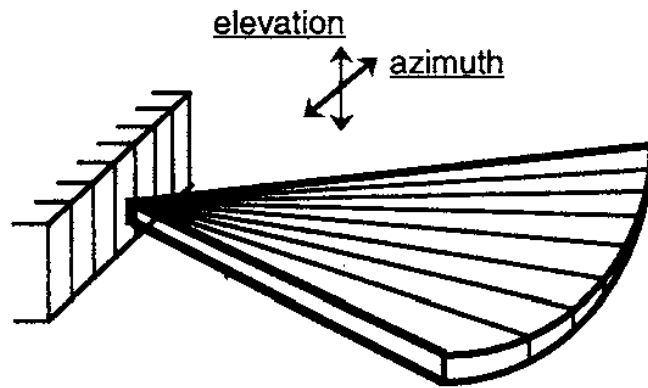
Figure A-5 Array-element configuration for linear phased array [52].

1.5D Arrays:

In construction they are similar to 2D arrays, but in operation they are similar to 1D arrays. They have elements in azimuth and elevation dimensions. To have high quality image dynamic focusing and phase correction can be done in both directions. In elevation dimension, they have limited numbers of elements, so that it is impossible to steer in this direction. Figure A-6. shows an example 1.5 array made for B-scan [52].
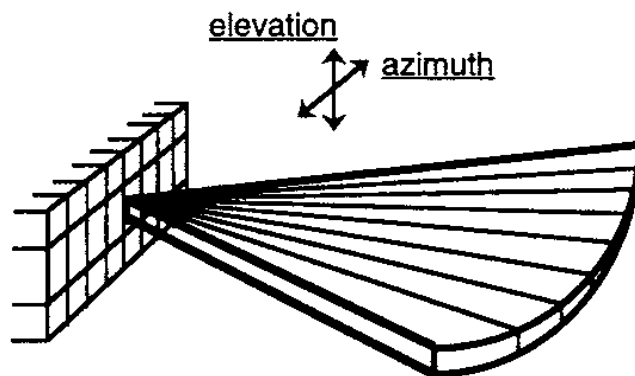
Figure A-6 Array-element configuration for 1.5 array made for B-scan [52].

134

2D Arrays:

They can have many elements in both azimuth and elevation dimensions. Thus, it is possible to steer and focus in both dimensions. An example is shown in Figure A-7.
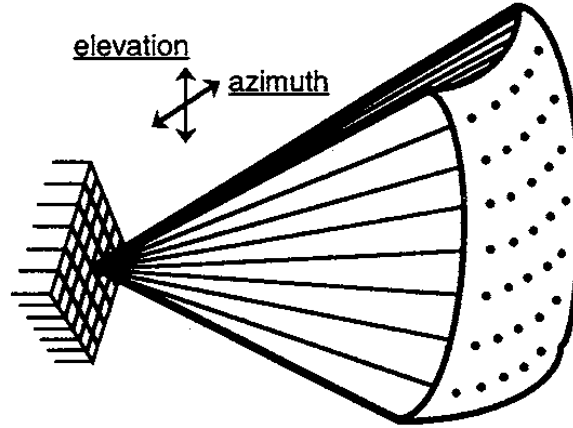
Figure A-7 Array-element configuration for 2D array [52].

A.2.3 Steering with Phased Array Transducers

In medical ultrasonic imaging generally array transducers are used. The general field from one element of an array source that consists of arbitrary shaped elements is as follows [49]:

$$P(x,y,z) = \iint_{surface} P_s ds = \iint_{surface} A_0(\mu,\eta) \cdot \frac{e^{j(wt-kd(\mu,\eta,x,y,z)+\varphi(\mu,\eta))}}{d(\mu,\eta,x,y,z)} \cdot ds \tag{A.1}$$

where $d(x,y,z)$ is the distance between point (μ,η) on the transmitting surface at the point Q. $A_0(\mu,\eta)$ is the amplitude at point (μ,η) and $\varphi(\mu,\eta)$ is the phase. If the array has N elements, the field equation can be rewritten as follows:

135

$$P(x, y, z) = \sum_{i}^{N} \iint_{surface-i} P_s ds_i = \sum_{i}^{N} \iint_{surface} A_{0i}(\mu,\eta) \cdot \frac{e^{j(wt - k \cdot d(\mu,\eta,x,y,z) + \varphi_i(\mu,\eta))}}{d(\mu,\eta,x,y,z)} \cdot ds_i$$

<div align="right">(A.2)</div>

here i is the index of each element.

This acoustic field is calculated by using the following schematic.
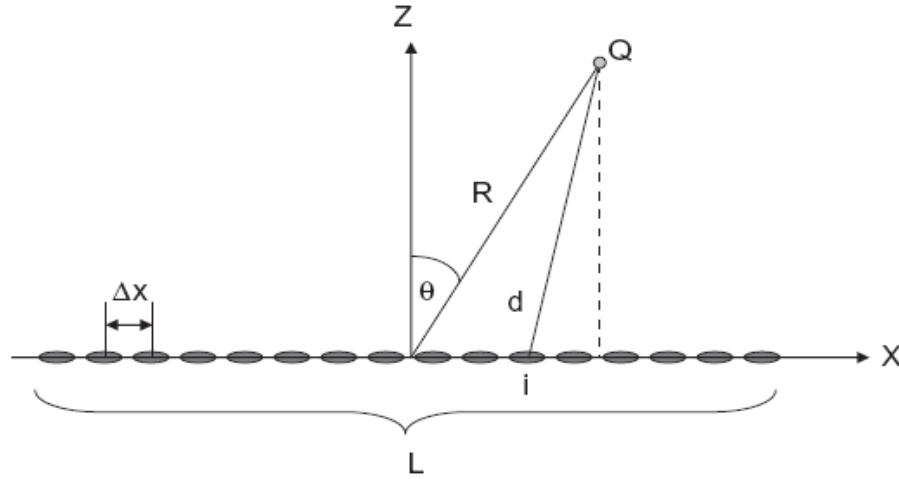
Figure A-8 Schematic of linear phased array [49].

In this figure;

$$x_i = (i-1) \cdot \Delta x - \frac{L}{2}$$

<div align="right">(A.3)</div>

The distance given as d is calculated as follows:

$$d(R,\theta)^2 = R^2 + x_i^2 - 2R \cdot x_i \cdot \cos(90° - \theta)$$
$$= R^2 + x_i^2 - 2R \cdot x_i \cdot \sin(\theta)$$

<div align="right">(A.4)</div>

By assuming the elements are sufficiently small to take into consideration as point source, the integration can be avoided and the field equation can be written as follows:

$$P(R,\theta) = \sum_i^N A_{0i} \cdot \frac{e^{j(wt - k \cdot d(R,\theta) + \varphi_i)}}{d(R,\theta)} \cdot a \qquad (A.5)$$

where a is the transmitting surface of each element. For far field approximation for a linear phased array, it is assumed that $R \gg x_i$, then the approximation for distance can be written as

$$d(R,\theta) \approx R - x_i \cdot \sin(\theta) \qquad (A.6)$$

By substituting above to the field equation into the field equation:

$$P(R,\theta) = \sum_i^N A_{0i} \cdot \frac{e^{j(wt - kd(R,\theta) + \varphi_i)}}{d(R,\theta)} \cdot a = a \cdot \frac{e^{j(wt - kR)}}{R} \sum_i^N A_{0i} \cdot e^{j(k \cdot x_i \cdot \sin(\theta) + \varphi_i)} \qquad (A.7)$$

If the amplitude and phase are same, then field equation is as:

$$P(R,\theta) = N \cdot A_0 \cdot a \cdot \frac{e^{j(wt - kR)}}{R} \left\{ \frac{\sin\left[k \dfrac{N \cdot \Delta x}{2} \sin(\theta) \right]}{N \cdot \sin\left[k \dfrac{\Delta x}{2} \sin(\theta) \right]} \right\} \qquad (A.8)$$

By using the linear phased arrays, the beam can be moved and steered. The next figure shows the motion of beams.
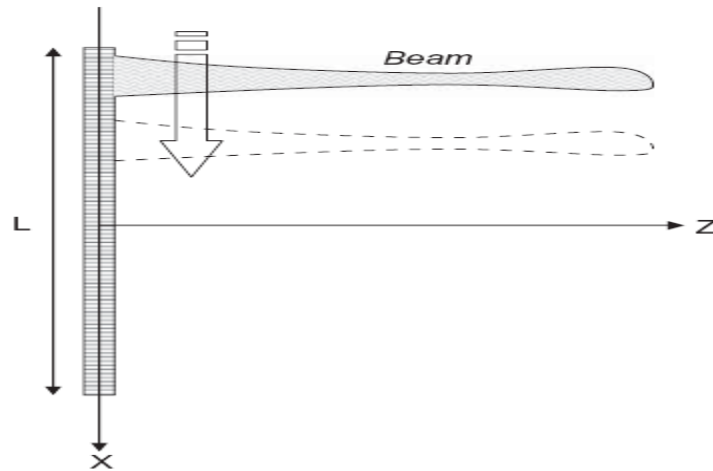
Figure A-9 Lateral beam motion of linear phased array [49].

The angular steering of linear phased array is shown in the following figure:
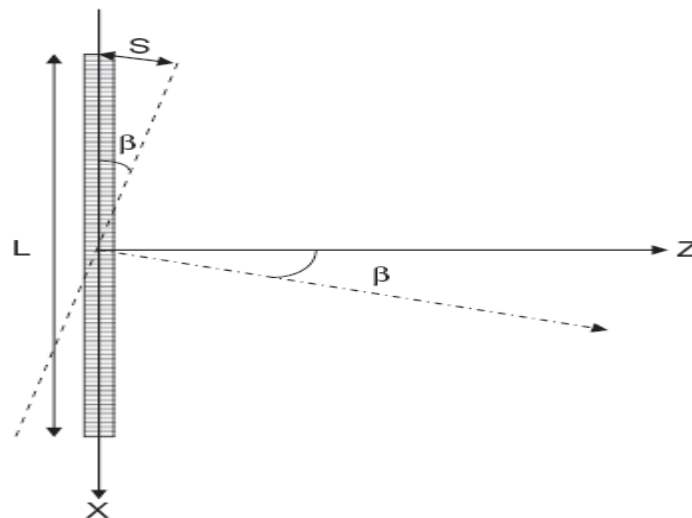
Figure A-10 The schematic view of linear phased array for steering of an acoustic field [49].

L is the length of the linear array with N elements. If all elements of the signal has the same phase in the same time, the pressure distribution is occurred as a linear wave front in the transducer's plane that is parallel to the array [49].

If the beams are steering with phase beta as in the Figure A-10, the term of φ_i can be changed as follows [49]:

$$\varphi_i = k \cdot x_i \cdot \sin(\beta)$$

$$\Rightarrow \varphi i = \left[(i-1) \cdot \Delta x - \frac{L}{2} \right] \cdot k \cdot \sin(\beta) \tag{A.9}$$

By substituting the above equation (A.9) in the pressure field equation (A.8), the final form of the pressure equation can be written as [49]:

$$P(R,\theta) == a \cdot \frac{e^{j(wt-kR)}}{R} \sum_i^N A_{0i} \cdot e^{j(k \cdot x_i \cdot \sin(\theta) + k \cdot x_i \cdot \sin(\beta))} \tag{A.10}$$

A.2.4 Focusing with Phased Array Transducers

In the previous part, steering the ultrasonic beam was described. Ultrasonic beam can be also formed, especially focused, with phased array transducer electronically. To focus the beam there is no need for any focusing hardware.

Consider the array transducer in Figure A-10. Ultrasonic beam can focus at a focal distance F along the z-axis. The corresponding phase for the element transmitting from the origin axes is $\varphi_0 = k \cdot F$. To focus at a focal point all elements should have the same phase at the focal point. Calculation of the phase element of each element i is as follows: multiply its distance to the focal point by the wave number and add its initial phase φ_i. This expression should equal to φ_0 as in Equation (A.11).

$$k \cdot \sqrt{x_i^2 + F^2} + \varphi_i = k \cdot F \tag{A.11}$$

After rearranging Eq. A.11, we obtain:

$$\varphi i = k \cdot \left(F - \sqrt{x_i^2 + F^2} \right) \tag{A.12}$$

The final form of resultant pressure formulation becomes as given below:

$$P(R,\theta) == a \cdot \frac{e^{j(wt-kR)}}{R} \sum_i^N A_{0i} \cdot e^{j\left(k \cdot x_i \cdot \sin(\theta) + k \cdot x_i \cdot \sin(\beta) + k \cdot \left(F - \sqrt{x_i^2 + F^2} \right) \right)} \tag{A.13}$$

APPENDIX B

ELECTRICAL AND ACOUSTIC PROPERTIES OF SOME HUMAN TISSUES

B.1. Electrical Properties of Some Human Tissues

Dielectric permittivity and conductivity values of some tissues are given for 50 kHz, 100 kHz, 500 kHz and 1 MHz in Table.B.1 and in Table.B.2, respectively.

Table B-1 Conductivity values of some human tissues at 50 kHz, 100 kHz, 500 kHz, and 1 MHz [38-40].

	50 kHz (S/m)	100 kHz (S/m)	500 kHz (S/m)	1 MHz (S/m)
Aorta	0.3169	0.3186	0.3239	0.3267
Bladder	0.2169	0.2189	0.2279	0.2360
Blood	0.7008	0.7029	0.7482	0.8221
Bone(Cancellous)	0.0834	0.0838	0.0867	0.0903
Bone (Cortical)	0.0206	0.0207	0.0222	0.0243
Bone Marrow (Infiltrated)	0.1027	0.1028	0.1035	0.1041

TableB-1 Continued

Bone Marrow (Not Infiltrated)	0.0036	0.0038	0.0044	0.0047
Brain (Grey Matter)	0.1275	0.1336	0.1519	0.1632
Brain (White Matter)	0.0776	0.0818	0.0947	0.1021
Breast Fat	0.0249	0.0250	0.0254	0.0257
Cartilage	0.1771	0.1785	0.2008	0.2328
Cerebellum	0.1475	0.1536	0.1725	0.1854
Cerebro Spinal Fluid	2.0000	2.0000	2.0000	2.0000
Cervix	0.5443	0.5476	0.5569	0.5624
Colon	0.2444	0.2477	0.2778	0.3141
Cornea	0.4814	0.4993	0.5773	0.6559
Dura	0.5017	0.5018	0.5026	0.5033
Eye Tissue (Sclera)	0.5147	0.5184	0.5615	0.6188
Fat (Average Infiltrated)	0.0433	0.0434	0.0438	0.0440
Fat (Not Infiltrate)	0.0242	0.0244	0.0248	0.0250
Gall Bladder	0.9001	0.9001	0.9002	0.9002
Gall Bladder Bile	1.4000	1.4000	1.4000	1.4000
Heart	0.1954	0.2151	0.2807	0.3275
Kidney	0.1594	0.1713	0.2283	0.2782
Lens Cortex	0.3385	0.3401	0.3528	0.3745

Table B-1 Continued

Lens Nucleus	0.2006	0.2007	0.2013	0.2018
Liver	0.0720	0.0845	0.1481	0.1866
Lung (Deflated)	0.2620	0.2716	0.3070	0.3343
Lung (Inflated)	0.1027	0.1073	0.1230	0.1360
Muscle	0.3518	0.3618	0.4459	0.5026
Nerve	0.0693	0.0807	0.1109	0.1302
Ovary	0.3362	0.3393	0.3502	0.3579
Skin (Dry)	0.0001	0.00025	0.0042	0.0130
Skin (Wet)	0.0290	0.0654	0.1776	0.2210
Small Intestine	0.5803	0.5942	0.7147	0.8648
Spleen	0.1179	0.1221	0.1471	0.1823
Stomach	0.5337	0.5360	0.5540	0.5837
Tendon	0.3878	0.3885	0.3908	0.3920
Testis	0.4344	0.4386	0.4911	0.5620
Thyroid	0.5339	0.5369	0.5658	0.6026
Tongue	0.2842	0.2879	0.3310	0.3882
Trachea	0.3299	0.3380	0.3591	0.3732
Uterus	0.5258	0.5314	0.5495	0.5642
Vitreous Humor	1.5000	1.5000	1.5003	1.5007

Table B-2 Dielectric permittivity values of some human tissues at 50 kHz, 100 kHz, 500 kHz, and 1 MHz [38-40].

	50 kHz (x1e3)	100 kHz (x1e3)	500 kHz (x1e3)	1 MHz (x1e3)
Aorta	1.633	0.9299	0.3123	0.2181
Bladder	1.9123	1.2310	0.5345	0.3427
Blood	5.1976	5.1200	4.1885	3.0263
Bone(Cancellous)	0.6131	0.4717	0.30816	0.2489
Bone (Cortical)	0.2641	0.2276	0.1745	0.1445
Bone Marrow (Infiltrated)	0.2444	0.1731	0.1095	0.0990
Bone Marrow (Not Infiltrated)	0.1805	0.1107	0.0489	0.0397
Brain (Grey Matter)	5.4613	3.2217	1.1869	860.4221
Brain (White Matter)	3.5481	2.1076	0.7122	0.4797
Breast Fat	1.1775	0.0706	0.0307	0.0236
Cartilage	2.7620	2.5722	1.9385	1.3908
Cerebellum	5.7555	3.5152	1.4749	1.1408
Cerebro Spinal Fluid	0.1089	0.1089	0.1089	0.1089
Cervix	3.1507	1.750	0.6140	0.4479
Colon	4.6106	3.7220	2.3702	1.6787

TableB-2 Continued

Cornea	16.970	10.5670	4.6365	2.8780
Dura	0.3938	0.3263	0.2644	0.2534
Eye Tissue (Sclera)	5.4946	4.7452	3.2519	2.1783
Fat (Average Infiltrated)	0.1632	0.1014	0.0567	0.0508
Fat (Not Infiltrated)	0.1724	0.0928	0.0345	0.0272
Gall Bladder	0.1724	0.1072	0.1011	0.1002
Gall Bladder Bile	0.1199	0.1199	0.1199	0.1199
Heart	16.9823	9.8458	3.2645	1.9673
Kidney	11.4294	7.6515	3.4432	2.2514
Lens Cortex	2.6265	2.0675	1.5021	1.2267
Lens Nucleus	0.2641	0.2003	0.1476	0.1387
Liver	10.6896	7.4988	2.7698	1.5357
Lung (Deflated)	8.5314	5.1452	1.8842	1.1705
Lung (Inflated)	4.2725	2.5812	1.0249	0.7331
Muscle	10.0937	8.0891	3.6472	1.8364
Nerve	9.5874	5.1330	1.4875	0.9261
Ovary	3.010	1.9417	0.8732	678.2865
Skin (Dry)	1.1267	1.1192	1.0619	0.9907

TableB-2 Continued

Skin (Wet)	21.8759	15.3567	3.6100	1.8328
Small Intestine	17.4050	13.8474	8.5941	5.6755
Spleen	5.4927	4.2222	2.7889	2.2900
Stomach	3.5511	2.8609	2.0647	1.6783
Tendon	0.81497	0.4724	0.2006	0.1600
Testis	6.4863	5.7169	4.0019	2.6833
Thyroid	4.0231	3.3011	2.1395	1.4333
Tongue	5.4960	4.7456	3.2520	2.1783
Trachea	6.9124	3.7347	1.1576	0.7750
Uterus	5.6698	3.4112	1.4893	1.1675
Vitreous Humor	0.0985	0.0979	0.09134	0.0840

B.2. Acosutic Properties of Some Human Tissues

Table B-3. Acoustic Properties of different tissues [57]

Material	Speed of Sound(m/s)	Density(kg/m^3)
Soft tissues	1520-1580	980-1010
Lipid-based tissues	1400-1490	920-940
Collagen-based tissues	1600-1700	1020-1100
Aqueous humor	1002-1006	1500
Vitreous humor	1090	1530
Blood	1580	1040-1090
Brain-grey	1532-1550	1039
Brain-white	1532-1550	1043
Skull-compact inner and outer tables	2600-3100	1900
Skull-spongy diploe	2200-2500	1000
Long bone-outer layer	2600-3100	1900
Long bone-inner layer	1700-2000	1100
Teeth	3500-4000	2200

APPENDIX C

SIGNAL-TO-NOISE RATIO OF A DATA ACQUISITION SYSTEM

The signal-to-noise ratio (SNR) of a data acquisition system with signal s and noise n can be defined as:

$$SNR = 10\log\frac{E(\|s\|^2)}{E(\|n\|^2)} \tag{C.1}$$

where $E(.)$ represents expected value and $\|.\|$ represents the Euclidean norm operations. The singular value at the truncation level (r) is the smallest singular value that satisfies the following inequality:

$$20\log\frac{\sigma_1}{\sigma_k} \leq SNR \quad \text{for k=1, ...r} \tag{C.2}$$

If r<n, then V becomes an nxr matrix, that is, the matrix V is truncated. The remaining basis vectors characterize the resolution matrix R.

CURRICULUM VITAE

PERSONAL INFORMATION

Surname, Name: Zengin, Reyhan

Nationality: Turkish (TC)

Date and Place of Birth: 1 January 1979, Malatya

Marital Status: Married

E-mail: reyhantutukzengin@gmail.com

EDUCATION:

Degree	Institution	Year of Graduation
MS&PhD	METU, Electrical and Electronics Engineering	2012
BS	Inonu Unv, Electrical and Electronics Engineering	2001
High School	Malatya Anadolu High School, Malatya	1996

WORK EXPERIENCE

Year	Place	Enrollment
2003-Present	METU, Dept. of Electrical and Electronics Eng.	Research Assistant

FOREIGN LANGUAGES

English

PUBLICATIONS:

1. Zengin R., Gençer N. G., ' Forward Problem Solution for Electrical Conductivity Imaging via ANSYS', 13th Biomedical Engineering Meeting, 2008, Ankara, Turkey

2. Zengin R., Gençer N. G., 'Forward Problem Solution for Contactless Electrical Conductivity Imaging with Realistic Head Model', 14th Biomedical Engineering Meeting 2009, İzmir, Turkey

3. Zengin R., Gençer N. G., 'Sensitivity Matrix Analysis for Contactless Electical Conductivity Imaging, 15th Biomedical Engineering Meeting 2010 , Antalya, Turkey

4. Zengin R., Gençer N. G., 'Dokunmasız Elektrik İletkenlik Görüntülemesi için Gerçekçi Kafa Modeli ile Duyarlılık Matrisi Analizi,' V. URSI-TURKIYE'2010, METU-Northern Cyprus Campus, North Cyprus Turkish Republic